Electronic Transport in Highly Mismatched InAs Films on GaAs

Yao Zhang

Thesis submitted to the Faculty of the
Virginia Polytechnic Institute and State University
in partial fulfillment of the requirements for the degree of

Master of Science
in
Electrical and Computer Engineering

Louis J. Guido, Chair
Jean J. Heremans
Mariusz K. Orlowski

December 9th, 2013
Blacksburg, Virginia

Keywords: InAs, surface accumulation layer, nucleation layer, band structure, three-band
Copyright 2013, Yao Zhang

Electronic Transport in Highly Mismatched InAs Films on GaAs

Yao Zhang

(ABSTRACT)

Electrical properties of Si- and Mg-doped InAs epitaxial layers grown by MOCVD were studied by performing magneto-transport measurements at different temperatures, from 300 K down to 1.2 K. The longitudinal magnetoresistance and Hall effect indicate a three-band system existing in n-type (p-type) InAs, which consists of the surface accumulation (inversion) layer, the bulk electron (hole) layer, and the nucleation layer. Therefore, a classical parabolic background in magnetoresistance due to multi-carrier occurs at low fields. With the magnetic field being further applied, a linear magnetoresistance caused by inhomogeneities is revealed. At liquid helium temperatures, the Shubnikov-de Haas magneto-oscillations are also observed. These transport characterizations provide a means of analyzing the band structure at the InAs surface. In a set of n-type InAs epilayers with Si doped at different levels, the bulk electron density increases as the doping level increases. The increased ionized impurities lead to lower electron mobilities due to more Coulomb scatterings. Within all of the n-type InAs films, except the two active layers (the surface and the bulk), the nucleation layer contributes to the film conductivity as well with an electron density of $\sim 5\times10^{17}$ cm^{-3} and a mobility of ~ 2000 cm^2/Vs. In a cooldown process, the electron density of each layer slightly and monotonically decreases whereas the mobility experiences a maximum from the competition between phonon scatterings and Coulomb scatterings. The phonon scattering overwhelms the Coulomb scatting at high temperatures, but declines as the temperature decreases, thus the mobility increases. Around 100 K, the temperature-independent ionized impurity scattering becomes comparable with and starts exceeding the phonon scattering. As the temperature being further lowered, the screening effect of the Coulomb scattering is weakened because of the decreased carrier densities. As a result, the mobility starts dropping. The maximum mobility corresponds to a minimum resistance, which explains the non-trivial temperature dependence of the resistance in the cooldown history. For the p-type InAs film, the doping with Mg in the course of MOCVD growth allows us to obtain a large hole density and a low mobility at 300 K. At low temperatures, holes are frozen out, and a strong negative magnetoresistance with a dip at 0 field are observed, which is the antilocalization signal from accumulation electrons. This is a strong technique to probe the surface quantum states and derive the phase coherence length and the spin flip length of surface electrons.

Dedication

I dedicate this dissertation work to my family. I am very grateful to my loving parents, Shucun and Ailian Zhang whose encouragements help me make up my mind to pursue this master degree in electrical engineering. I am also thankful to my parents and sister in law for their understanding. Especially my sister in law, Shuchun Wu, who used to live with and take care of my wife and me in Blacksburg for about three years, she is like a real sister to me. Primarily, I dedicate my master dissertation to my beloved wife, Wenchun Wu, and our son Alexander Jiru Zhang. They provide me with unconditional supports. After a whole busy day, no matter how exhausted I am, as long as I step into my house and look at their smiles, all of the anxieties and worries are released. Without my family, I can not accomplish this dissertation.

Acknowledgments

This project would not have been possible without the support of many people. First and most, I would like to thank Prof. Louis Guido for his expertise and precious time of reading, encouraging, and most of all patience throughout the entire process. I wish to thank Prof. Jean Heremans who is my Ph.D. thesis advisor in physics. Without his encouragements and the experimental technique supports, I can not accomplish this master degree in electrical engineering. The countless discussion between him and me is crucial for determining the fundamental structure of this project. Next, I wish to acknowledge the help I received from Prof. Victoria Soghomonian who gives me invaluable advices and opinions. I am thankful to all of my lab colleagues I am thankful to all of my lab colleagues Tim Ciarkowski, Kevin Chern, Noah Allen, Rachel Umbel, and Andrew Giordani. I want to specifically single out Tim Ciarkowski who grew the InAs wafers I used in my project. I wish to thank my wife Wenchun who has been ever so understanding and supportive of my research work. She takes great care of our family and made me concentrate on this dissertation.

Contents

1 Introduction **1**
1.1 Overview . . . 1
1.2 Outline . . . 2

2 Experimental **4**
2.1 Growth . . . 4
2.2 Sample Fabrication . . . 6
2.3 Measurement Setup . . . 7

3 *n*-type InAs **11**
3.1 Cooldown . . . 11
3.2 Room Temperature Band Structure . . . 12
3.2.1 Lightly Doped *n*-type InAs . . . 12
3.2.2 Moderately Doped *n*-type InAs . . . 22
3.2.3 Heavily Doped *n*-type InAs . . . 25
3.3 Liquid Nitrogen Temperature Band Structure . . . 29
3.3.1 Lightly Doped *n*-type InAs . . . 29
3.3.2 Moderately Doped *n*-type InAs . . . 32
3.3.3 Heavily Doped *n*-type InAs . . . 35
3.4 Liquid Helium Temperature Band Structure . . . 35
3.4.1 Shubnikov-de Haas Oscillation . . . 35
3.4.2 Lightly Doped *n*-type InAs . . . 38

3.4.3 Moderately Doped n-type InAs 45
3.4.4 Heavily Doped n-type InAs 49

4 p-type InAs 56
4.1 Room Temperature Band Structure 56
4.1.1 Surface Inversion Layer 56
4.1.2 Two-band Fitting 56
4.1.3 Surface Band Structure 57
4.2 Liquid Helium Temperature Band Structure 59
4.2.1 $T = 8.2$ K 59
4.2.2 $T = 1.2$ K 64

5 Discussion 69
5.1 n-type InAs 69
5.2 p-type InAs 70

6 Summary 71

Bibliography 72

List of Figures

2.1 Aixtron 200/4 RF-S MOCVD system. (a) Reactor and glove box. (b) Material sources. 5

2.2 Schematic of the InAs/GaAs structures with the test layers shaded. 5

2.3 (a) Schematics of YZ01 and YZ02 Van der Pauw samples on a DIP header. (b) A picture of YZ01 and YZ02 Van der Pauw chips mounted on a 14-pin DIP header, with one cent by side as a comparison to demonstrate the dimensions of the sample. 7

2.4 (a) On the left is the cryogen-free cryostat, which consists of the pulse tube cryofridge (Cryomech PT405), the split-coil magnet, and the Cryomech CP 900 compressor. Equipments on the right shelf are SR 830 DSP lock-in amplifier, LakeShore 331 temperature controller, KEPCO power supply, GMW magnet systems current reversal switch, and Power Ten power supply. (b) Probe used for connecting the sample with the measurement system, with a thermocouple next to the sample. 8

2.5 Schematics of cryogen-free cryostat (a) and ^{3}He cryostat (b). 9

2.6 Equipments on the left shelf are LakeShore 370 AC resistance bridge, Princeton Applied Research P124A analog lock-in amplifier, SR 830 digital lock-in amplifier, EG&G 7265 digital lock-in amplifier, Keithley 2400 source meter, Keithley 2000 multimeter, Cryomagnetics CS-4 superconducting magnet power supply. On the right is the cryostat system. 10

3.1 Cooldown of n-type InAs 13

3.2 YZ01 Van der Pauw magneto-transport measurements at $T = 300$ K 14

3.3 Schematic band structure of YZ01 to demonstrate the formation of the band-bending and the accumulation layer at the surface. 15

3.4 Resistance of YZ01 Van der Pauw on each side. 17

3.5 (Color online) (a) R_d and (b) R_{xy} data of YZ01 Van der Pauw at $T = 300$ K. The circles are experimental values (For clarity, 1 out of 16 experimental points only are plotted). Red solid lines are fitted curves from the two-band fitting, which in (a) leads to a parabolic background in R_d. 17

3.6 (Color online) (a) R_d and (b) R_{xy} data of YZ01 Van der Pauw at $T = 300$ K. The circles are experimental values (For clarity, 1 out of 16 experimental points only are plotted). Red solid lines are fitted curves from the three-band fitting. 18

3.7 (Color online) Room temperature schematic band structure at the surface of sample YZ01, where the 2DES has two occupied subbands [the energy levels are explained in the text, and $|\Psi_i|^2$ ($i = 1, 2$) represents the probability density (in arbitrary units, with $|\Psi_i|^2 = 0$ taken at the E_i line)]. 21

3.8 YZ02 Van der Pauw magneto-transport measurements at $T = 300$ K 23

3.9 Schematic band structures of YZ01 and YZ02 to demonstrate the positions of E_F in the bulk. The shaded area is the accumulation layer, and YZ02 is expected to have more surface electrons due to the larger shaded area. 24

3.10 (Color online) (a) R_d and (b) R_{xy} data of YZ02 Van der Pauw at $T = 300$ K. The circles are experimental values (For clarity, 1 out of 16 experimental points only are plotted). Red solid lines are fitted curves from the three-band fitting. 24

3.11 (Color online) Room temperature schematic band structure at the surface of sample YZ02, where the 2DES has two occupied subbands [the energy levels are explained in the text, and $|\Psi_i|^2$ ($i = 1, 2$) represents the probability density (in arbitrary units, with $|\Psi_i|^2 = 0$ taken at the E_i line). 25

3.12 YZ03 Van der Pauw magneto-transport measurements at $T = 300$ K 26

3.13 Schematic band structures of YZ01, YZ02, and YZ03 to demonstrate the rising of E_F in the bulk due to the increased doping. The shaded area is the accumulation layer. Compared with YZ01 and YZ02, there is less potential confinement on the YZ03 surface layer. 27

3.14 (Color online) (a) R_d and (b) R_{xy} data of YZ03 Van der Pauw at $T = 300$ K. The circles are experimental values (For clarity, 1 out of 16 experimental points only are plotted). Red solid lines are fitted curves from the three-band fitting. 28

3.15 (Color online) Room temperature schematic band structure at the surface of sample YZ03, where the 2DES has two occupied subbands [the energy levels are explained in the text, and $|\Psi_i|^2$ ($i = 1, 2$) represents the probability density (in arbitrary units, with $|\Psi_i|^2 = 0$ taken at the E_i line). 29

3.16 YZ02 Van der Pauw magneto-transport measurements at $T = 82$ K 30

3.17 (Color online) (a) R_d and (b) R_{xy} data of YZ01 Van der Pauw at $T = 82$ K. The circles are experimental values (For clarity, 1 out of 16 experimental points only are plotted). Red solid lines are fitted curves from the three-band fitting. 31

3.18 (Color online) At $T = 82$ K, schematic band structure at the surface of sample YZ01, where the 2DES has two occupied subbands [the energy levels are explained in the text, and $|\Psi_i|^2$ ($i = 1, 2$) represents the probability density (in arbitrary units, with $|\Psi_i|^2 = 0$ taken at the E_i line)]. 32

3.19 YZ02 Van der Pauw magneto-transport measurements at $T = 82$ K 33

3.20 (Color online) (a) R_d and (b) R_{xy} data of YZ02 Van der Pauw at $T = 82$ K. The circles are experimental values (For clarity, 1 out of 16 experimental points only are plotted). Red solid lines are fitted curves from the three-band fitting. 34

3.21 (Color online) At $T = 82$ K, schematic band structure at the surface of sample YZ02, where the 2DES has two occupied subbands [the energy levels are explained in the text, and $|\Psi_i|^2$ ($i = 1, 2$) represents the probability density (in arbitrary units, with $|\Psi_i|^2 = 0$ taken at the E_i line). 34

3.22 YZ03 Van der Pauw magneto-transport measurements at $T = 80$ K 36

3.23 (Color online) (a) R_d and (b) R_{xy} data of YZ03 Van der Pauw at $T = 80$ K. The circles are experimental values (For clarity, 1 out of 16 experimental points only are plotted). Red solid lines are fitted curves from the three-band fitting. 37

3.24 (Color online) At $T = 80$ K, schematic band structure at the surface of sample YZ03, where the 2DES has two occupied subbands [the energy levels are explained in the text, and $|\Psi_i|^2$ ($i = 1, 2$) represents the probability density (in arbitrary units, with $|\Psi_i|^2 = 0$ taken at the E_i line). 37

3.25 (Color online) Left panel: Explanation of the de Haas-van Alphen effect with filled orbitals of the Fermi sea shaded. Right panel: Shubnikovde Haas Oscillation of YZ01 at $T = 4.5$ K, parabolic background of R_{xx} is subtracted to obtain better resolution. B_1 and B_3 indicate where the minimum energy occur while B_2 signifies the maximum. 38

3.26 YZ01 Van der Pauw magneto-transport measurements at $T = 4.5$ K 39

3.27 (Color online) Shubnikov-de Haas oscillations of (a) δR_{xx} and (b) δR_{yy} at $T = 4.5$ K, and parabolic backgrounds are subtracted to obtain better resolution. (c) and (d) Fast Fourier transforms (FFT) of the data in (a) and (b) respectively. The first peaks in (c) and (d) are both from background noise, and the second peaks are from the Shubnikov-de Haas oscillation, indicating a same frequency. 40

3.28 (Color online) (a) R_d and (b) R_{xy} data of YZ01 Van der Pauw at $T = 4.5$ K. The circles are experimental values (For clarity, 1 out of 16 experimental points only are plotted). Red solid lines are fitted curves from the three-band fitting. 41

3.29 (Color online) At $T = 4.5$ K, schematic band structure at the surface of sample YZ01, where the 2DES has two occupied subbands [the energy levels are explained in the text, and $|\Psi_i|^2$ ($i = 1, 2$) represents the probability density (in arbitrary units, with $|\Psi_i|^2 = 0$ taken at the E_i line)]. 42

3.30 YZ01 Van der Pauw magneto-transport measurements at $T = 1.2$ K 43

3.31 (Color online) Shubnikov-de Haas oscillations of (a) δR_{xx} and (b) δR_{yy} at $T = 1.2$ K, and linear backgrounds are subtracted to obtain better resolution. (c) and (d) Fast Fourier transforms (FFT) of the data in (a) and (b) respectively. The first peaks in (c) and (d) are both from background noise. The second and the third peaks are from the Shubnikov-de Haas oscillation. 44

3.32 (Color online) (a) R_d and (b) R_{xy} data of YZ01 Van der Pauw at $T = 1.2$ K. The circles are experimental values (For clarity, 1 out of 50 experimental points only are plotted). Red solid lines are fitted curves from the three-band fitting. 45

3.33 (Color online) At $T = 1.2$ K, schematic band structure at the surface of sample YZ01, where the 2DES has the first subband occupied [the energy levels are explained in the text, and $|\Psi_1|^2$ represents the probability density (in arbitrary units, with $|\Psi_1|^2 = 0$ taken at the E_1 line)]. 46

3.34 YZ02 Van der Pauw magneto-transport measurements at $T = 4.5$ K 47

3.35 (Color online) Shubnikov-de Haas oscillations of (a) δR_{xx} and (b) δR_{yy} at $T = 4.5$ K, and parabolic backgrounds are subtracted to obtain better resolution. (c) and (d) Fast Fourier transforms (FFT) of the data in (a) and (b) respectively. The first peaks in (c) and (d) are both from background noise, and the second peaks are from the Shubnikov-de Haas oscillation, indicating a same frequency. 48

3.36 (Color online) (a) R_d and (b) R_{xy} data of YZ02 Van der Pauw at $T = 4.5$ K. The circles are experimental values (For clarity, 1 out of 16 experimental points only are plotted). Red solid lines are fitted curves from the three-band fitting. 48

3.37 (Color online) At $T = 4.5$ K, schematic band structure at the surface of sample YZ02, where the 2DES has two occupied subbands [the energy levels are explained in the text, and $|\Psi_i|^2$ ($i = 1, 2$) represents the probability density (in arbitrary units, with $|\Psi_i|^2 = 0$ taken at the E_i line)]. 49

3.38 YZ01 Van der Pauw magneto-transport measurements at $T = 1.2$ K 50

3.39 (Color online) Shubnikov-de Haas oscillations of (a) δR_{xx} and (b) δR_{yy} at $T = 1.2$ K, and linear backgrounds are subtracted to obtain better resolution. (c) and (d) Fast Fourier transforms (FFT) of the data in (a) and (b) respectively. The first peaks in (c) and (d) are both from background noise. The second and the third peaks are from the Shubnikov-de Haas oscillation. 51

3.40 (Color online) (a) R_d and (b) R_{xy} data of YZ02 Van der Pauw at $T = 1.2$ K. The circles are experimental values (For clarity, 1 out of 50 experimental points only are plotted). Red solid lines are fitted curves from the three-band fitting. 52

3.41 (Color online) At $T = 1.2$ K, schematic band structure at the surface of sample YZ02, where the 2DES has the first subband occupied [the energy levels are explained in the text, and $|\Psi_1|^2$ represents the probability density (in arbitrary units, with $|\Psi_1|^2 = 0$ taken at the E_1 line)]. 52

3.42 YZ03 Van der Pauw magneto-transport measurements at $T = 4.5$ K 53

3.43 (Color online) (a) R_d and (b) R_{xy} data of YZ03 Van der Pauw at $T = 4.5$ K. The circles are experimental values (For clarity, 1 out of 16 experimental points only are plotted). Red solid lines are fitted curves from the three-band fitting. 54

3.44 (Color online) At $T = 4.5$ K, schematic band structure at the surface of sample YZ03, where the 2DES has two occupied subbands [the energy levels are explained in the text, and $|\Psi_i|^2$ ($i = 1, 2$) represents the probability density (in arbitrary units, with $|\Psi_i|^2 = 0$ taken at the E_i line). 55

4.1 Left panel: Schematic band structure at the surface of p-type InAs. E_F is above the surface conduction minimum and close to the bulk valence band maximum. The shaded area is the inversion layer, while the holes stay in the bulk and are separated from the surface electrons by a depletion layer. Right panel: Schematic of the InAs/GaAs heterostructure with surface electron inversion layer (Black) and the bulk hole test layer (shaded). 57

4.2 YZ04 Van der Pauw magneto-transport measurements at $T = 300$ K 58

4.3 (Color online) (a) R_d and (b) R_{xy} data of YZ04 Van der Pauw at $T = 300$ K. The circles are experimental values (For clarity, 1 out of 16 experimental points only are plotted). Red solid lines are fitted curves from the two-band fitting. 59

4.4 (Color online) Room temperature schematic band structure at the surface of sample YZ04, where the 2DES has two occupied subbands [the energy levels are explained in the text, and $|\Psi_i|^2$ ($i = 1, 2$) represents the probability density (in arbitrary units, with $|\Psi_i|^2 = 0$ taken at the E_i line)]. 60

4.5 Quantum interference of time reversed paths of an electron with a perpendicular B. 61

4.6 Characteristic shape of the AL measurement. Curve shape sensitive to phase coherence time τ_ϕ and spin-orbit scattering time τ_{SO}. 61

4.7 YZ04 Van der Pauw magneto-transport measurements at $T = 8.2$ K 63

4.8 (Color online) (a) R_d and (b) R_{xy} data of YZ04 Van der Pauw at $T = 8.2$ K. The circles are experimental values (For clarity, 1 out of 16 experimental points only are plotted). Red solid lines are fitted curves from the three-band fitting. 64

4.9 (Color online) (a) Magnetoresistance due to AL within a small range of B at 8.2 K. (b) R_d data with AL fitting at 8.2 K. The circles are experimental values (For clarity, 1 out of 2 and 1 out of 20 experimental points only are plotted in (a) and (b) respectively). Red solid lines are fitted curves from Eq. 4.3. 65

4.10 YZ04 Van der Pauw magneto-transport measurements at $T = 1.2$ K 66

4.11 (Color online) (a) R_d and (b) R_{xy} data of YZ04 at 1.2 K. The black line and the circles are experimental values [For clarity, in (b) 1 out of 50 experimental points only are plotted]. Red solid lines are fitted curves from the two-band analysis, which in (a) leads to a parabolic background in MR. 67

4.12 (Color online) (a) Magnetoresistance due to AL within a small range of B at 1.2 K. (b) R_d data with AL fitting at 1.2 K. The circles are experimental values (For clarity, 1 out of 2 and 1 out of 40 experimental points only are plotted in (a) and (b) respectively). Red solid lines are fitted curves from Eq. 4.3. 67

List of Tables

2.1 InAs test layer thickness, doping type and density, and carrier transport properties: three-dimensional (3D) electron density n_{3D}, 3D hole density p_{3D}, and μ at $T = 300$ K. 6

Chapter 1

Introduction

1.1 Overview

Moore's Law states that the number of transistors in unit area doubles every two years. For more than four decades, the continuous scaling down of chip geometries allows Moore's Law to remain on track. However, the applicable limit for semiconductor process technology will be reached when chip process geometries shrink to be smaller than 20 nm. The end of Moore's Law has been predicted to be happen in the near future, but new technological processes have always come to the rescue. Recently, an attempt to further develop advanced complementary metal-oxide semiconductor (CMOS) technologies, which is internationally defined as *more Moore*, has emerged as a promising solution. In addition, an application of the new state variables (like spin) is referred as *beyond the CMOS*, which is another post Moore's law technology. In the category of *more Moore*, narrow-gap III-V semiconductors demonstrate significant potentials to replace the conventional metaloxidesemiconductor field-effect transistor (MOSFET) channel materials due to their high mobilities. Within *beyond the CMOS* field, the prominent intrinsic structural spin-orbit interaction (SOI) of III-V compounds is practical for spin-field-effect-transistor in spin electronics. Hence, III-V semiconductors attracted enormous attention and my dissertation is to study one of the most prevalent III-V semiconductors, InAs.

There has been much interest in the use of InAs as a material for high-speed device applications due to its extraordinarily high electron mobilities [1]. InAs is either undoped or n-type doped in most cases, and for almost all n-type zinc-blende III-V semiconductor surfaces, an electron depletion layer is observed (except on the defect-free perfectly cleaved III-V(110) surfaces where no band bending occurs), with Fermi level E_F pinned within the band gap [2]. However, InAs is unique among zinc-blende III-V semiconductors, since an electron accumulation layer can be easily formed at the surface instead, which hindered development of InAs-based electronic devices. It is well established that the surfaces of InAs exhibit an

accumulation layer with E_F pinning way above the conduction band minimum due to the donorlike surface states [2, 3, 4, 5, 6]. The strong band bending creates a considerable Rashba SOI. As mentioned above, the existence of the metallic surface could be problematic for InAs to become ideal channel materials, because typical CMOS transistors require a pinched-off channel at their normal mode to avoid leakage currents. Therefore, removing the surface electrons is crucial to make InAs CMOS attainable. This can be achieved by adjusting the surface Fermi level down below the conduction band, which yields a detailed knowledge of the InAs band structure. This dissertation focused on understanding the InAs surface band structure at different doping levels by applying magneto-transport characterizations. During the transport, Both the surface accumulation layer and the bulk active layer contribute to the conductivity of InAs films and they possess different electron mobilities and densities. Thus we are facing two layers with different types of carriers conducting in parallel. The characterization of the transport properties of this two-band system is critical for calculating the surface band structure of InAs, which in turn provides the information of surface Fermi level.

1.2 Outline

When InAs epitaxial layers are doped at different levels, the varied doping concentration modifies not only the carrier density, but also the mobility μ and the band structure. To investigate how these properties correspond to the variation of the doping density, we did a series of magneto-transport measurements on both n- and p-type InAs epilayers grown on GaAs (100) substrates through metal organic chemical vapor deposition (MOCVD). In the interest of maximizing the utility of this document, the contents and purpose of each chapter is previewed as following.

In Experimental, we managed to grow three n-type InAs epitaxial layers doped with Si and one p-type InAs epilayer doped with Mg. The schematic heterostructure is depicted and the transport properties of all epilayers are tabled. We also introduced the sample fabrication process and the experimental setups for measurements.

All of the measurements were conducted in the temperature T range T = 1.2 K – 300 K. We first measured the cooldown history of three n-type InAs films, and a non-trivial T dependence of the resistance is explained in the first section of chapter n-type InAs. Then the measured magnetoresistance of three n-type InAs films at room temperature are discussed in the second section. As the doping level increases, more electrons from dopants are expected to be populated in the bulk, thus the Fermi level E_F is raised. The surface electron density will be also varied due to the shift of E_F. Except the surface and the bulk electrons, the carriers in a InAs nucleation layer have to be considered as well for the contributions to the film conductivity. The growth condition of the nucleation layer is kept the same for all of the three films, thereby, similar nucleation layer transport properties are obtained, which are $\sim 5 \times 10^{17}$ cm^{-3} in density and ~ 2000 cm^2/Vs in mobility. For every n-type InAs film, the

degradation of the bulk electron density can be almost neglected compared with the reduction of k_BT in the Fermi-Dirac distribution when the temperature is lowered, where k_B is the Boltzmann constant, indicating the rising of E_F in the bulk during cooldown. From cooldown history, all of the three n-type InAs epilayers experience a minimum resistance at $\sim$ the liquid nitrogen temperature. The third section presents our measurement results around $T = 77$ K. The minimum resistance slightly shifts to higher temperature with heavier doping, and corresponds to a maximum mobility caused by the competition between the phonon and the ionized impurity scatterings. Phonon scatterings overwhelm other scattering mechanisms at high temperatures, but decrease in the cooldown, which improves the mobility. The mobility will stop increasing when phonon scattering exceeded by T-independent Coulomb scatterings, and starts dropping because that the slight decrease of electron densities as T decreases weakens the screening effect of the ionized impurity scatterings. In the fourth section, around liquid helium temperatures E_F of the three epilayers rise above the bulk conduction band minimum, therefore the bulks become degenerate. Whereas the surface E_F of all three epilayers are slightly lowered when T declines. Shubnikov-de Haas oscillations with two different periods in $1/B$ were observed, from which the surface and the bulk electron densities and mobilities can be derived and are consistent with our three-band model analysis. The surface band structures are similar with the ones around $T = 77$ K and 300 K.

The Mg doped p-type InAs sample is analyzed in the fourth chapter. The band bending still provides surface electrons, which form an inversion layer separated from the holes in the bulk by a depletion layer between. The mobilities of both electrons and holes are very low. At room temperature, the sheet density of holes p is so large that the whole system behaves as a mono-band structure. However p is decreasing as T decreases, and the system turns into more n-type. The magnetoresistance (MR) measurement indicates that electrons dominate the transport system below 10 K. Since the mobility μ is very low, the Hall measurement probes the contribution from the nucleation layer as well in addition to the surface and the bulk layers. Thus a three-band structure is formed. When the system is further cooled down to 1.2 K, both the bulk and the nucleation layer will be frozen out. Besides, a robust antilocalization (AL) signal due to surface electrons is observed, which is a quantum interference of time reversed paths of electrons. The appearance of this signal requires a relatively low carrier mobility and a strong SOI, which are both satisfied by our p-type InAs sample.

Chapter 2

Experimental

2.1 Growth

We systematically characterized four different InAs epitaxial layers in this dissertation, three n-type InAs epilayers doped with Si from low to high (YZ01 to YZ03) and one p-type InAs epilayer doped with Mg (YZ04). All of the epilayers are grown through Aixtron 200/4 RF-S single-wafer MOCVD system (Fig. 2.1). As schematically depicted in Fig. 2.2, the structure was grown on a 2-inch diameter semi-insulating (SI) GaAs (100) substrate. An unintentionally doped (UID) GaAs buffer layer was first grown to eliminate the impact from the oxidation layer. The following InAs growth experienced a two-step process. At temperature T = 475 °C, $\sim$ 150 nm InAs nucleation layer was grown on top of the GaAs buffer layer and UID with C, H, and O. At T = 625 °C, 1.5 – 2.0 μm thick InAs test layer was grown on top of the nucleation layer and intentionally doped with Si or Mg. There is no miscut on substrate, and the surface is (100) to within $\pm$ 0.5°. Trimethylindium TMIn and arsine AsH_3 were used as precursors to deposit InAs. Silane SiH_4 and bis cyclopentadienyl magnesium CP_2Mg were chosen to dope the test layer with Si and Mg. H_2 was employed as the carrier gas with reactor pressure at 104 Pa.

Dopants and their densities and the test layer thickness in the second step of the InAs growth are summarized in Table 2.1. In addition, it also lists the transport properties at room temperature obtained by growers with applying a small range of magnetic field B. There are two contradictions in the transport properties obtained by growers. One is for n-type InAs films, whose electron densities do not match with the doping concentrations. The other is for the p-type InAs, which only contains electrons. Nonetheless, the above data are only rough measurements under low fields. In Chap. 3, we applied a sophisticated three-band model to characterize the electrons densities in the test layer of InAs films, which are consistent with the doping densities. In Chap. 4, the Hall effect remeasured within large magnetic fields reveals that holes exist as majorities in the bulk while a small amount of

(a) (b)

Figure 2.1: Aixtron 200/4 RF-S MOCVD system. (a) Reactor and glove box. (b) Material sources.

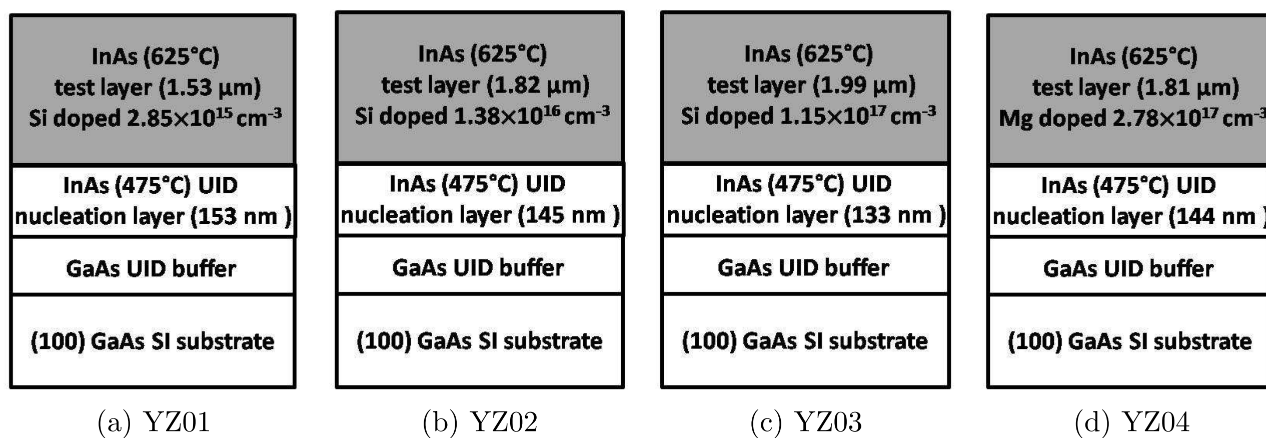

(a) YZ01 (b) YZ02 (c) YZ03 (d) YZ04

Figure 2.2: Schematic of the InAs/GaAs structures with the test layers shaded.

Table 2.1: InAs test layer thickness, doping type and density, and carrier transport properties: three-dimensional (3D) electron density n_{3D}, 3D hole density p_{3D}, and μ at $T = 300$ K.

Samples	Name	InAs (μm)	Doping density (cm^{-3})	n_{3D} or p_{3D} (cm^{-3})	μ (cm^{-2}/Vs)
100806-1	YZ01	1.53	Si: 2.85×10^{15}	n_{3D}: 2.67×10^{16}	10807
100806-2	YZ02	1.82	Si: 1.38×10^{16}	n_{3D}: 2.83×10^{16}	15857
120608-2	YZ03	1.99	Si: 1.15×10^{17}	n_{3D}: 6.61×10^{16}	20620
100818-1	YZ04	1.81	Mg: 2.78×10^{17}	p_{3D}: 2.47×10^{17}	302

electrons form an inversion layer at the surface.

2.2 Sample Fabrication

The MR is measured by applying the standard Van der Pauw [7] technique, which is commonly used to measure the resistivity and the Hall effect of a sample. This technique requires that the sample thickness must be much less than the width and length of the sample, and four infinitely small ohmic contacts have to be placed on the boundary of the sample. Figure 2.3 (a) demonstrates a sample layout on a 14-pin Dual In-Line (DIP) header with the direction notations of $\hat{x}$ and $\hat{y}$. Take YZ01 in Fig. 2.3 (a) as an example, when the current is applied along $\hat{x}$ (from 1 to 3), $\hat{y}$ (from 1 to 8), and the diagonal (from 1 to 10), with the voltage being measured between 8 and 10, 3 and 10, and 3 and 8 respectively, the resistances calculated from the corresponding voltages and currents are called R_{xx}, R_{yy}, and R_{xy}.

The first step of sample fabrication is to prepare 2×2 mm^2 InAs chips by cleaving from InAs wafers. To make samples neat and clean, the chips are obtained by sawing the GaAs (100) surface (the back side) of the wafer with a carbide tip first, then cleaned by soaking in trichloroethylene (TCE), acetone (ACE), and isopropyl alcohol (IPA) in consecutive order for 3 minutes each to remove organic, ionic, and metallic impurities. At the end, the surface is rigorously squirted with IPA and blown dry with N_2 to physically remove any large dust particles.

After cleaning, In-Sn alloy is soldered at each corner of the chip as ohmic contacts, and the soldering temperature is 175 °C. Then the chip is connected to the mounting package (DIP header) by soldering Au wires with In [Fig. 2.3 (b)]. In is chosen because it is stable and conductive at low temperature (1.2 K), and its low melting point (156.6 °C) also eliminates the unexpected thermal annealing of the chip. Limited to the number of lock-in amplifiers and the chip size, only two InAs chips are typically attached to a DIP header by greasing them with Apiezon N low temperature grease, which ensures that the device does not fall off of the DIP header.

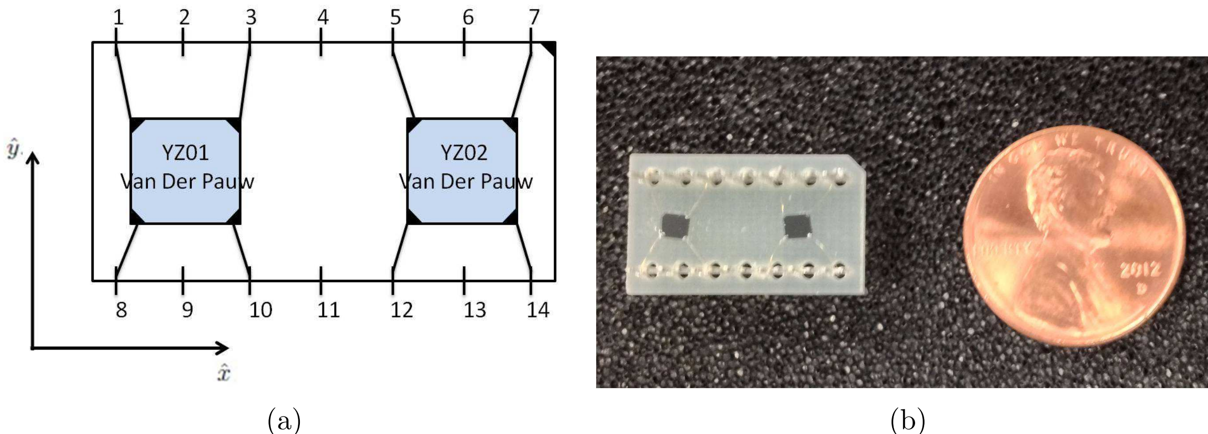

(a) (b)

Figure 2.3: (a) Schematics of YZ01 and YZ02 Van der Pauw samples on a DIP header. (b) A picture of YZ01 and YZ02 Van der Pauw chips mounted on a 14-pin DIP header, with one cent by side as a comparison to demonstrate the dimensions of the sample.

2.3 Measurement Setup

Two apparatuses are employed to perform the magneto-transport measurements. For T = 4.5 K − 300 K and B = -1.2 T − 1.2 T, a cryogen-free cryostat capable of 4.5 K in steady state (Fig. 2.4) is used. As depicted in Fig. 2.5 (a), a cold finger is cooled by a pulse tube cryofridge (Cryomech PT405) driven by a compressor (Cryomech CP950COPSW-4). The cold finger can reach approximately 2 K, and through thermal conduction the sample can reach a base temperature of $\sim$ 4.5 K. The cryogen-free system is equipped with a resistive magnet capable of magnetic fields up to 1.4 T. The sample needs to be mounted onto a probe (Fig. 2.4) to insert into the cryostat. The probe contains a calibrated thermometer and a resistive heater, used for controlling and varying the temperature at temperatures other than the base temperature.

To further cooldown the sample to 1.2 K, a ^{3}He cryostat capable of 0.4 K in steady state (Fig. 2.6) is applied. The ^{3}He system is a homebuilt insert for a commercial ^{4}He cryostat (Janis), depicted in Fig. 2.5 (b), which has several chambers filled with liquid He that can be pumped on to lower the vapour pressure, thus lowering the temperature. It incorporates a superconducting (SC) magnet to achieve magnetic fields of up to 9 T. In addition, it is not necessary to use ^{3}He in the inner-most chamber. Often, a ^{4}He exchange gas is used, which raises the base temperature to 1.2 K.

All of the measurements are performed by using lock-in amplifiers with magnetic fields perpendicular to the surfaces of InAs epilayers. AC current is applied from lock-in to the sample via a contact box. Experimental setup is controlled through a LabView (National Instruments) control software via GPIB (general purpose interface bus) lines.

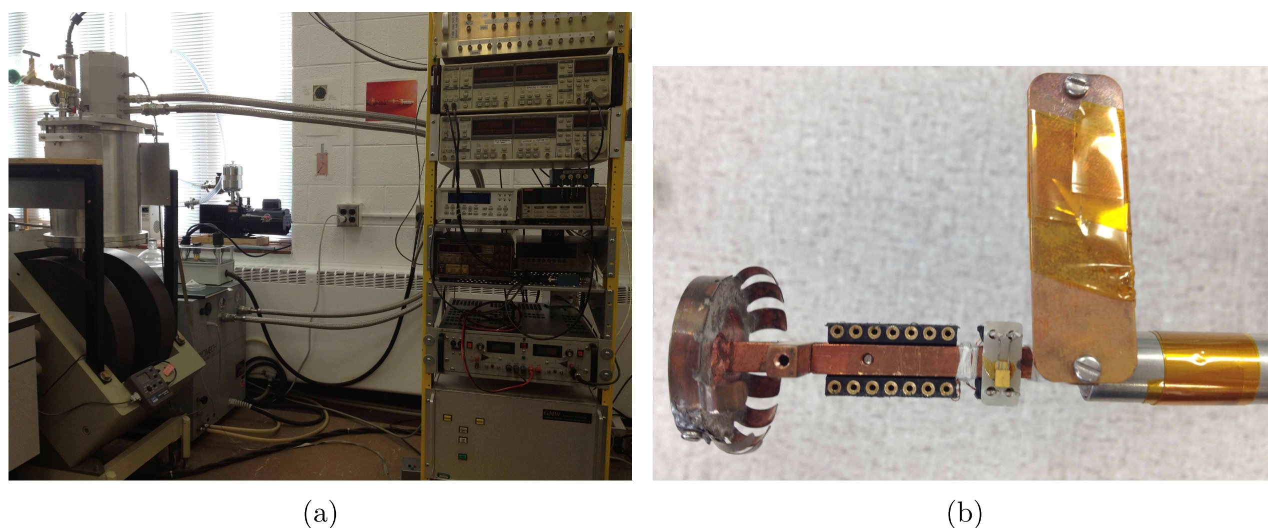

(a) (b)

Figure 2.4: (a) On the left is the cryogen-free cryostat, which consists of the pulse tube cryofridge (Cryomech PT405), the split-coil magnet, and the Cryomech CP 900 compressor. Equipments on the right shelf are SR 830 DSP lock-in amplifier, LakeShore 331 temperature controller, KEPCO power supply, GMW magnet systems current reversal switch, and Power Ten power supply. (b) Probe used for connecting the sample with the measurement system, with a thermocouple next to the sample.

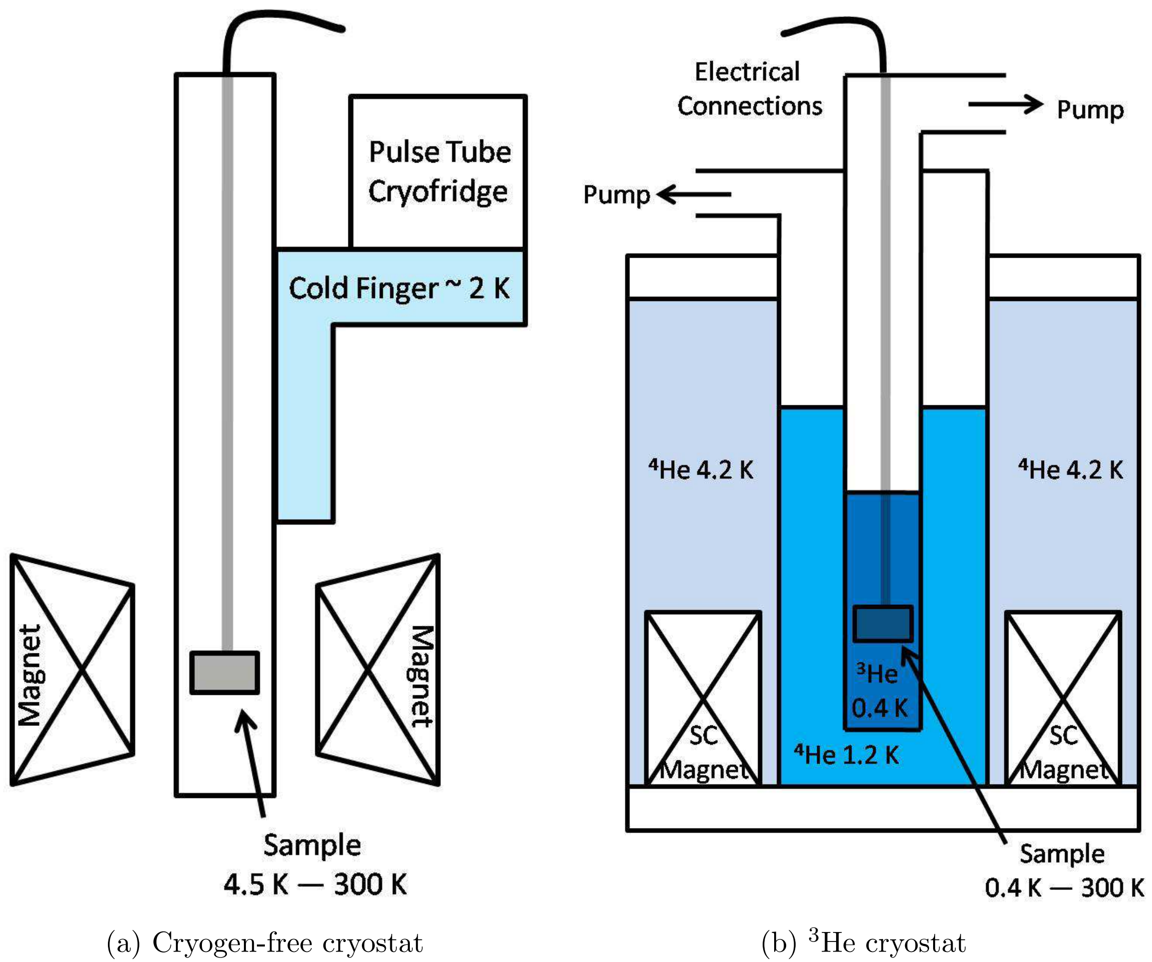

(a) Cryogen-free cryostat

(b) ^{3}He cryostat

Figure 2.5: Schematics of cryogen-free cryostat (a) and ^{3}He cryostat (b).

Figure 2.6: Equipments on the left shelf are LakeShore 370 AC resistance bridge, Princeton Applied Research P124A analog lock-in amplifier, SR 830 digital lock-in amplifier, EG&G 7265 digital lock-in amplifier, Keithley 2400 source meter, Keithley 2000 multimeter, Cryomagnetics CS-4 superconducting magnet power supply. On the right is the cryostat system.

Chapter 3

n-type InAs

3.1 Cooldown

For semiconductors, the resistance is often increasing as T decreases due to less carrier populating in the conduction band. However, the measurements of R_{xx} at varied temperatures for all of the three n-type InAs samples demonstrate a variation from the conventional T dependence of semiconductor resistances. The resistances of three n-type InAs samples first drop and then increase during a cooldown from 300 K to 4.5 K (Fig. 3.1). The resistance is determined by the carrier density and mobility, which are both influenced by the temperature. Since the dopants used are shallow donors for InAs, the carrier density only slightly and monotonically decreases when T is lowered. Therefore the minimum resistance during the cooldown corresponds to a maximum mobility, which is caused by the competition between two scattering mechanisms. One is the strong T-dependent phonon scattering, and the other is the T-independent Coulomb scattering from the ionized impurities. In fact, phonon scatterings overwhelm other scattering mechanisms at high temperatures. Thus when T declines the mobility is improved due to the gradual freeze-out of phonons. Around $T = 80$ K, the phonon scattering is exceeded by the Coulomb scattering. As a result, the resistance reaches its minimum and is expected to saturate. However, an increase of the resistance is observed instead of a saturation, indicating a T-dependent behaviour related to the Coulomb scattering. It is well known that the scattering cross section for Coulomb scattering is T-independent, nonetheless, Coulomb scattering can be reduced by the screening effect from electrons themselves in the conducting channels during the transport. When T is further lowered, the slight reduction in electron density weakens the screening effect, thereby the mobility will drop after reaching a maximum. In conclusion, the competition between the phonon and the Coulomb scatterings originates this non-trivial temperature dependence of the resistance. Additionally, the minimum resistance is observed to slightly shift to higher temperatures with heavier doping. This could be attributed to more ionized impurities in the lattice strengthening the Coulomb scattering to exceed the phonon scattering at a relatively

higher temperature. The resistance minima are close to each other and all around the liquid nitrogen temperature (77 K). The magneto-transport characterizations are hence performed at room temperature, liquid nitrogen temperature, and liquid helium temperature in the following sections.

3.2 Room Temperature Band Structure

3.2.1 Lightly Doped n-type InAs

Two-band System

It is well established that at the surfaces of InAs the Fermi level E_F is pinned above the conduction band minimum due to the donorlike surface states, forming an electron accumulation layer and hence a two-dimensional electron system (2DES) at the surface. However, E_F is still below the conduction band minimum in the bulk, which acts as a n-type semiconductor, and provides as yet another conducting layer parallel to the accumulation layer. The formation of the InAs surface band structure can be schematically described in Fig. 3.3. When the surface and the bulk are in thermal equilibrium, YZ01 is characterized by a spatially constant E_F throughout the semiconductor structure, which leads to a downward band-bending in band structure. This band-bending occurs primarily within the surface layer whereas the energy bands remain relatively flat in the bulk. For the lightly doped n-type InAs sample (YZ01), its longitudinal (R_{xx} and R_{yy}) and transverse resistance (R_{xy}) in Fig. 3.2 (the parabolic magnetoresistance background and the non-linear Hall signal) indicate the presence of at least two types of carriers with different densities and mobilities. Considering the InAs surface band structure, we first attribute the multi-type carriers to the surface and the bulk electrons. For any magneto-transport measurement data presented in this dissertation, R_{xx} and R_{yy} are symmetrized and R_{xy} is antisymmetrized to remove components resulting from electronic shifts.

Two-band Fitting

In the Drude model, the MR is characterized by the resistivity tensor $\hat{\rho}$. For a system with only one type of carriers (electron), we have

$$\hat{\rho} = \begin{pmatrix} \rho_{xx} & \rho_{xy} \\ \rho_{yx} & \rho_{yy} \end{pmatrix} = \frac{1}{ne\mu} \begin{pmatrix} 1 & -\mu B \\ \mu B & 1 \end{pmatrix}. \tag{3.1}$$

where $\frac{1}{ne\mu} = \rho$ is the resistivity at $B = 0$ with n and μ being the electron density and mobility. Equation 3.1 implies that for a mono-band system R_{xx} and R_{yy} are B-independent, while

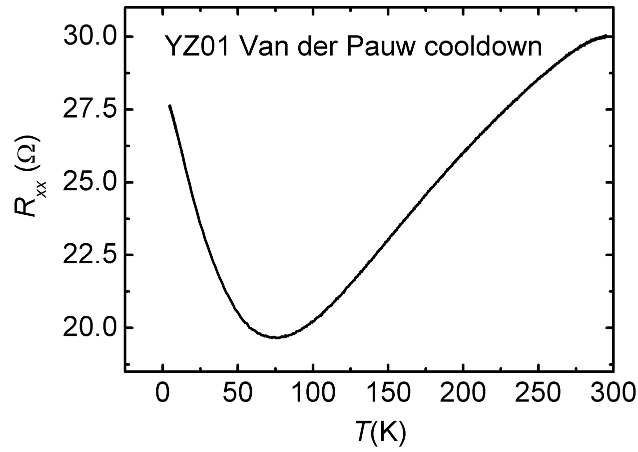

(a) Cooldown of YZ01

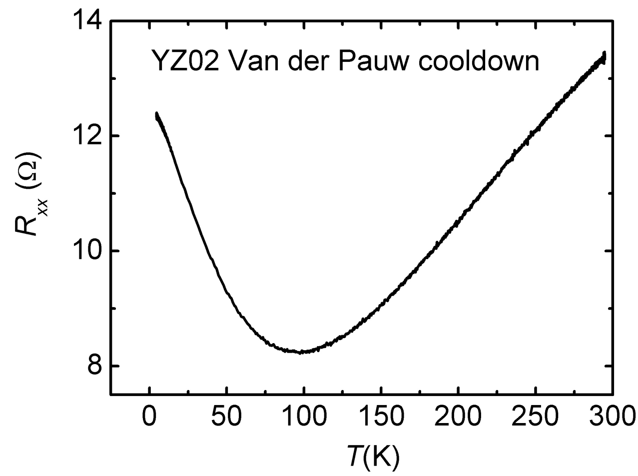

(b) Cooldown of YZ02

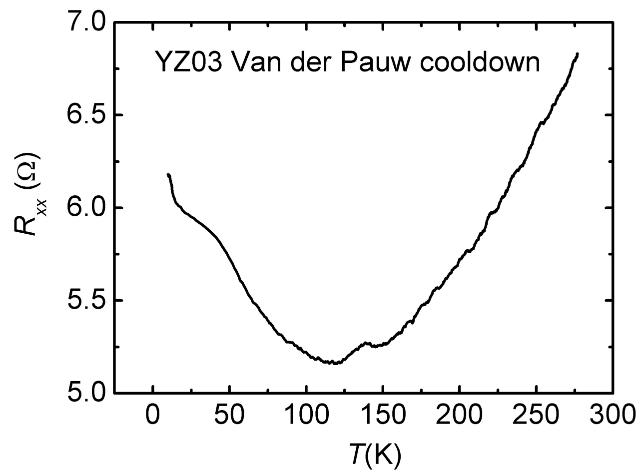

(c) Cooldown of YZ03

Figure 3.1: Cooldown of n-type InAs

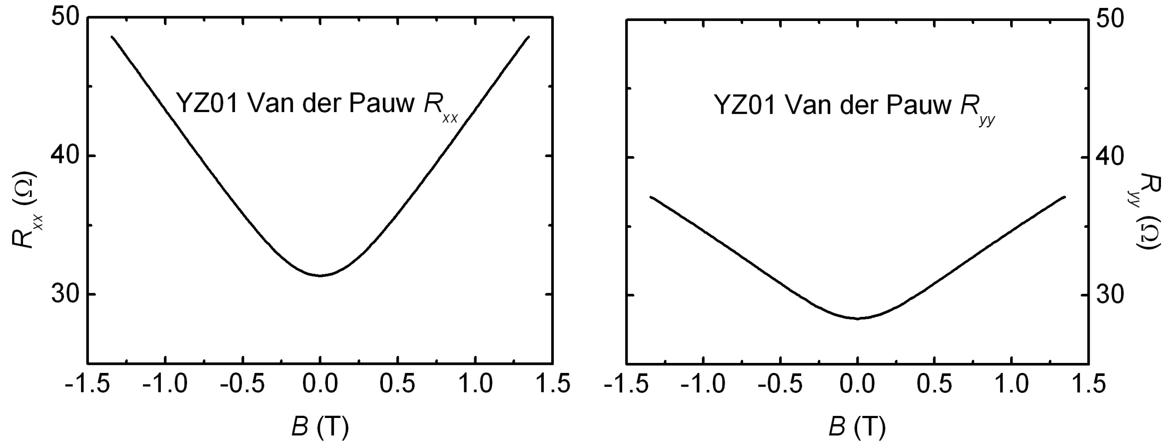

(a) Longitudinal MR of YZ01 Van der Pauw along $\hat{x}$.

(b) Longitudinal MR of YZ01 Van der Pauw along $\hat{y}$.

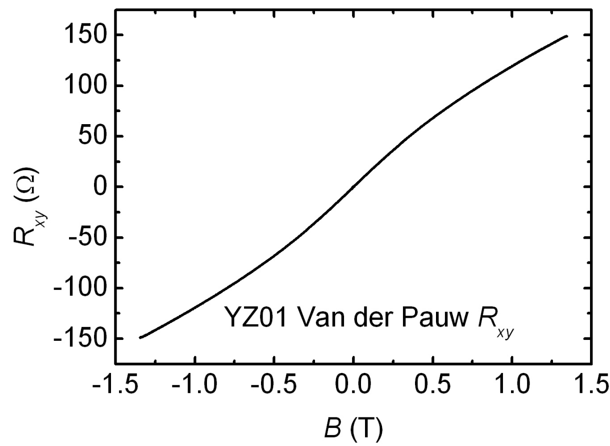

(c) Transverse MR of YZ01 Van der Pauw

Figure 3.2: YZ01 Van der Pauw magneto-transport measurements at $T = 300$ K

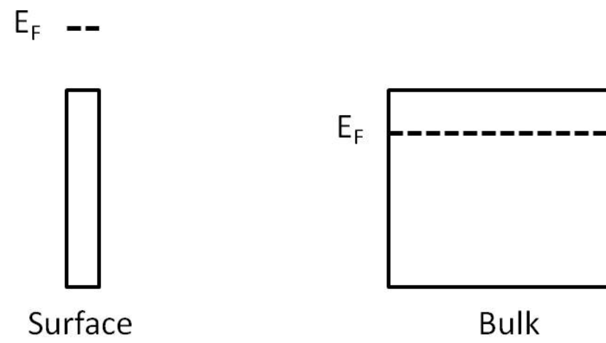

(a) Positions of E_F at the surface and the bulk.

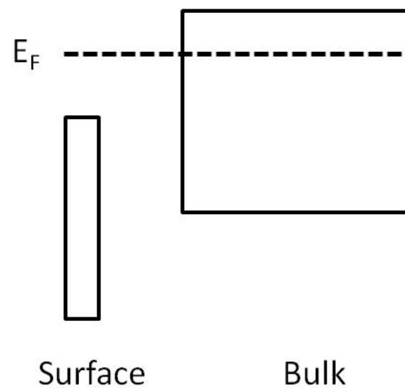

(b) The position of E_F is unvaried inside the semiconductor.

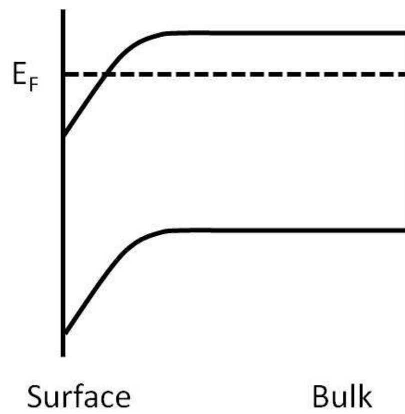

(c) Band-bending due to the spacially constant E_F.

Figure 3.3: Schematic band structure of YZ01 to demonstrate the formation of the band-bending and the accumulation layer at the surface.

R_{xy} is linear in B. However, our n-type InAs is assumed to be a two-band system with two sets of different electronic transport parameters [8], which are the surface electron mobility and sheet density (μ_s and n_s), and the bulk electron mobility and sheet density (μ_b and n_b). Each set corresponds to an independent resistivity tensor $\hat{\rho}_i$ [$i = s$ (surface) and b (bulk)]. Solving the matrix equation of the total resistivity tensor $\hat{\rho} = (\hat{\rho}_s^{-1} + \hat{\rho}_b^{-1})^{-1}$, the longitudinal and the transverse components in Eq. 3.1 are modified into

$$\begin{cases} \rho_{xx} = \dfrac{n_s\mu_s + n_b\mu_b + \mu_s\mu_b(n_s\mu_b + n_b\mu_s)B^2}{e[(n_s\mu_s + n_b\mu_b)^2 + (n_s + n_b)^2(\mu_s\mu_b B)^2]} \\ \rho_{xy} = \dfrac{[n_s\mu_s^2 + n_b\mu_b^2 + \mu_s^2\mu_b^2(n_s + n_b)B^2)]B}{e[(n_s\mu_s + n_b\mu_b)^2 + (n_s + n_b)^2(\mu_s\mu_b B)^2]} \end{cases} . \tag{3.2}$$

The two-band model can be extended to more than two types of carriers by introducing more conducting channels in the summation of $\hat{\rho} = (\sum_i \hat{\rho}^{-1})^{-1}$ [9], where i denotes the index of the carrier type, and

$$\hat{\rho}_i^{-1} = \begin{pmatrix} \dfrac{n_i e\mu_i}{1 + \mu_i^2 B^2} & \dfrac{n_i e\mu_i^2 B}{1 + \mu_i^2 B^2} \\ -\dfrac{n_i e\mu_i^2 B}{1 + \mu_i^2 B^2} & \dfrac{n_i e\mu_i}{1 + \mu_i^2 B^2} \end{pmatrix} . \tag{3.3}$$

In Eq. 3.2, there is a quadratic B term in the numerator of ρ_{xx} and ρ_{yy}, which explains the parabolic-like background in the Figs. 3.2(a) and 3.2(b). The difference between R_{xx} and R_{yy} demonstrates an anisotropy in the resistance of YZ01 Van der Pauw. Furthermore, the cubic term in the numerator of ρ_{xy} (Eq. 3.2) causes the slope changing in the Hall measurement [Fig. 3.2(c)]. To utilize both R_{xx} and R_{yy} in the two-band fitting, we assume a current being applied from the contact 1 to 10 [Fig. 2.3(a)] to introduce the diagonal longitudinal resistance $R_d = \frac{1}{2}(R_{xx} + R_{yy})$. As illustrated in Fig. 3.4, the resistance layout of YZ01 Van der Pauw is simplified as if there is one resistor on each side of the Van der Pauw. Thereby, the resistance between the contacts 1 and 10 can be calculated by taking two resistors with resistance $R_{xx} + R_{yy}$ connected in parallel.

Figure 3.5 manifests a sufficient correspondence between the measurements and the theoretical two-band fitting. By simultaneously fitting R_d and R_{xy} to ρ_{xx} and ρ_{xy} from Eq. 3.2, two sets of μ and n are extracted as

$$\begin{cases} \mu_1 = 16000 \text{ cm}^2/\text{Vs} \\ n_1 = 1.9 \times 10^{12} \text{ cm}^{-2} \end{cases}, \quad \text{and} \quad \begin{cases} \mu_2 = 2100 \text{ cm}^2/\text{Vs} \\ n_2 = 7.7 \times 10^{12} \text{ cm}^{-2} \end{cases}. \tag{3.4}$$

There are four free parameters in this fitting, which can be reduced to two by implementing the constraints $\rho_{xx}|_{B=0} = 1/e(n_s\mu_s + n_b\mu_b)$ and $\rho'_{xy}|_{B=0} = (n_s\mu_s^2 + n_b\mu_b^2)/[e(n_s\mu_s + n_b\mu_b)^2]$, with $\rho_{xx}(B = 0)$ given in Fig. 3.5 (a) and $\rho'_{xy}|_{B=0}$ being the zero-field slope of the Hall signal

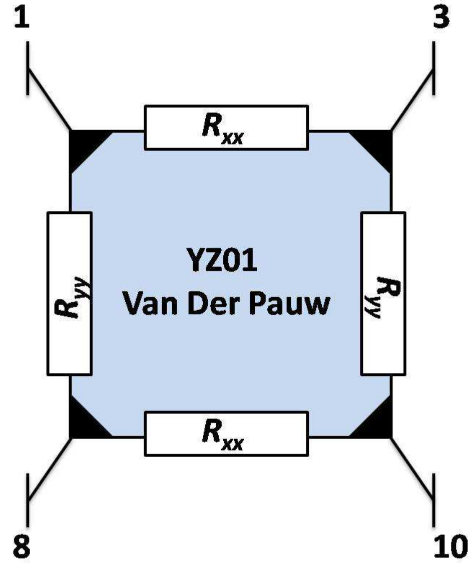

Figure 3.4: Resistance of YZ01 Van der Pauw on each side.

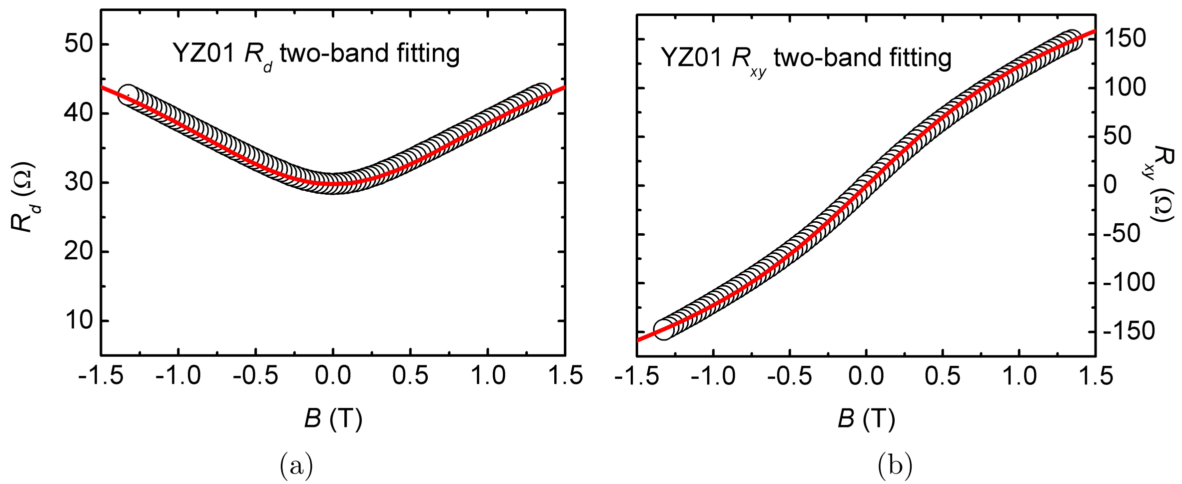

Figure 3.5: (Color online) (a) R_d and (b) R_{xy} data of YZ01 Van der Pauw at T = 300 K. The circles are experimental values (For clarity, 1 out of 16 experimental points only are plotted). Red solid lines are fitted curves from the two-band fitting, which in (a) leads to a parabolic background in R_d.

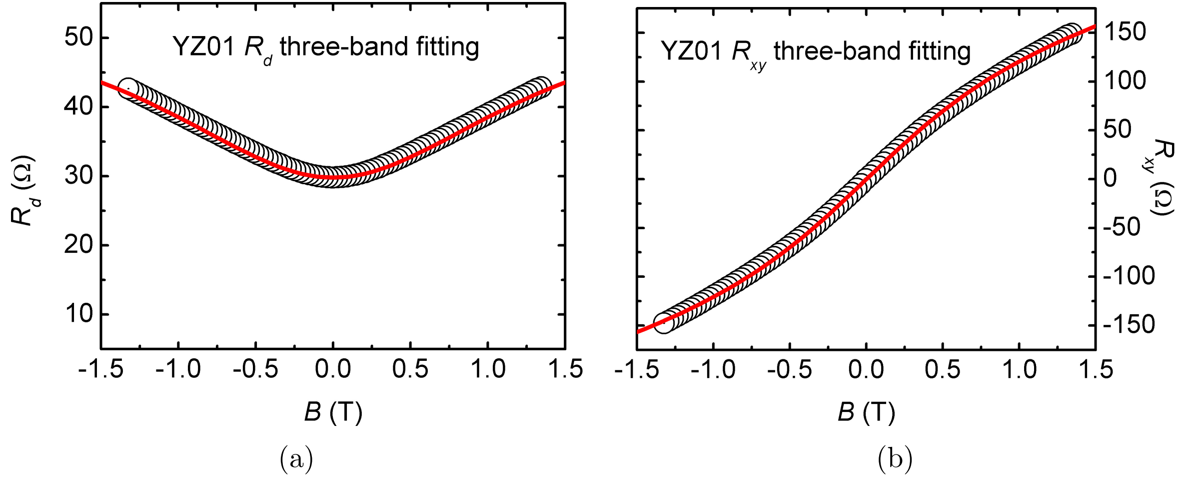

Figure 3.6: (Color online) (a) R_d and (b) R_{xy} data of YZ01 Van der Pauw at T = 300 K. The circles are experimental values (For clarity, 1 out of 16 experimental points only are plotted). Red solid lines are fitted curves from the three-band fitting.

in Fig. 3.5 (b). Based on previous studies of InAs films [10, 11, 12], the reasonable values for μ_s and μ_b are $\sim$ 5000 cm^2/Vs and $\sim$ 20000 cm^2/Vs, so we assign μ_s = 2100 cm^2/Vs, n_s = 7.7×10^{12} cm^{-2}, μ_b = 16000 cm^2/Vs, and n_b = 1.9×10^{12} cm^{-2}. However, the high n_s from this assignation provides an extremely large surface electric field $\sim 2 \times 10^5$ V/cm, which exceeds the breakdown field of InAs. This irrational field is obtained from the calculation of E_F in subsubsection *Surface Band Structure*, by considering the surface band-bending as a triangular potential well. The calculation applies the quasi-relativistic dispersion, with InAs room temperature band gap of 360 meV and the γ-point electron effective mass of $m_e^* = 0.024 m_e$ where $m_e = 9.11 \times 10^{-31}$ kg.

Since μ_2 and n_2 in Eq. 3.4 can not be assigned to either the surface or the bulk electrons, they have to be from the nucleation layer electrons, which satisfy the prerequisites of low mobility but high density. The surface and the bulk electrons are buried together in carrier 1 from the two-band fitting. Therefore the two-band fitting needs to be adjusted into three-band by adding the nucleation layer conductivity tensor $\hat{\rho}_n^{-1}$ with its electron mobility μ_n and density n_n. Knowing the values of μ_n and n_n, switching to three-band fitting in fact does not involve additional fitting freedom. Figure 3.6 demonstrates the three-band fitting results of both R_d and R_{xy}. Likewise, three sets of μ and n can be extracted as

$$\begin{cases} \mu_1 = 9900 \text{ cm}^2/\text{Vs} \\ n_1 = 1.5 \times 10^{12} \text{ cm}^{-2} \end{cases}, \quad \begin{cases} \mu_2 = 26000 \text{ cm}^2/\text{Vs} \\ n_2 = 0.43 \times 10^{12} \text{ cm}^{-2} \end{cases}, \quad \text{and} \quad \begin{cases} \mu_3 = 2100 \text{ cm}^2/\text{Vs} \\ n_3 = 7.7 \times 10^{12} \text{ cm}^{-2} \end{cases}. \tag{3.5}$$

We assign μ_s = 9900 cm^2/Vs, n_s = 1.5×10^{12} cm^{-2}, μ_b = 26000 cm^2/Vs, n_b = 0.43×10^{12} cm^{-2}, μ_n = 2100 cm^2/Vs, and n_n = 7.7×10^{12} cm^{-2}. The assignation is in great agreement

with other semiconductor parameters which will be discussed later in this section.

Quasi-relativistic Dispersion

It was noted in the past that the electrons of narrow-gap semiconductors behave analogous to relativistic electrons in vacuum with linear energy-momentum relation [13]. The analogy was also reported to hold in the presence of crossed magnetic and electric fields confirmed by cyclotron-resonance experiments performed on InSb [14]. For electrons and light holes in direct narrow-gap semiconductors with zinc-blende structure like InAs, this quasi-relativistic dispersion between energy E and the wavenumber k is employed. In the absence of external fields $E(k)$ relation is derived as [14]

$$E_k = \sqrt{\left(\frac{E_g}{2}\right)^2 + E_g \frac{\hbar^2 k^2}{2m_e^*}} - \frac{E_g}{2}, \tag{3.6}$$

where E_g and $\hbar$ are band gap and Dirac constant. Under this non-parabolic dispersion, the effective mass at any given E can be defined as

$$m(E)^* = m_e^* \left(1 + \frac{2E}{E_g}\right)^3. \tag{3.7}$$

Consequently, the conventional (non-relativistic) two-dimensional (2D) and three-dimensional (3D) density of states are modified as

$$\begin{aligned} g_{2\mathrm{D}}(E) &= \frac{m_e^*}{\pi\hbar^2}\left(1 + \frac{2E}{E_g}\right), \\ g_{3\mathrm{D}}(E) &= \frac{m_e^*\sqrt{2m_e^* E}}{\pi^2\hbar^3}\left(1 + \frac{2E}{E_g}\right)\sqrt{1 + \frac{E}{E_g}}. \end{aligned} \tag{3.8}$$

Surface Band Structure

The results of n_s and n_b obtained from the three-band fitting allow determination for E_F and the band-bending at the surface. Electrons follow Fermi-Dirac distribution, together with Eq. 3.8, the 3D bulk electron density can be derived as

$$n_{b3\mathrm{D}} = \int_{E_C^b}^{\infty} \frac{m_e^*\sqrt{2m_e^*(E - E_C^b)}}{\pi^2\hbar^3} \frac{1}{e^{\frac{E-E_F}{kT}} + 1}\left[1 - \frac{2(E - E_C^b)}{E_g}\right]\sqrt{1 - \frac{E - E_C^b}{E_g}} dE. \tag{3.9}$$

where E_C^b and k_B are bulk conduction band minimum and Boltzmann constant. Through secondary ion mass spectrometry measurements, the donor concentration is characterized to be 0.285×10^{16} cm^{-3} (Table 2.1). On the other hand, from n_b and the test layer thickness, the numerical value of $n_{b3\text{D}}$ is calculated to be 0.28×10^{16} cm^{-3}, indicating ionizations of most donors, which is consistent with the small Si donor ionization energy in bulk InAs $\sim$ 1 meV [15, 16]. At room temperature, the dopant electrons possess enough thermal energy ($k_BT = 26$ meV) to break free from the impurity atoms. Therefore, almost the entire amount of the donors are supposed to be ionized and E_F will lie above the middle of E_g. Plugging the numerical value of $n_{b3\text{D}}$ into Eq. 3.9, Fermi level is attained to be 97 meV below E_C^b. The band-bending at the surface approximately forms a triangular potential well, where the energies of accumulation electrons are quantized into a couple of subbands. In the triangular well approximation, a constant electric field F at the surface and an infinitely high potential barrier at the interface are presumed [17]. Correspondingly, the subbands energies E_i with respect to the surface conduction band minimum E_C^s are

$$E_i - E_C^s = \left(\frac{9\pi^2}{8m_e^*}\right)^{\frac{1}{3}} \left[e\hbar F\left(i - \frac{1}{4}\right)\right]^{\frac{2}{3}},\ i = (1,\ 2,\ 3, ...), \tag{3.10}$$

with $e = 1.6 \times 10^{-19}$ C being the electron charge. We first assume only one subband is occupied in the potential well, thereby n_s can be expressed in an integral similar to Eq. 3.9 as

$$n_s = \int_{E_1}^{\infty} \frac{m_e^*}{\pi\hbar^2} \frac{1}{e^{\frac{E-E_F}{kT}} + 1} \left[1 - \frac{2(E - E_C^s)}{E_g}\right] dE. \tag{3.11}$$

With the n_s value obtained from the three-band fitting, a test calculation from Eqs. 3.10 and 3.11 reveals E_2 is also below E_F, which implies an occupation of two subbands from the surface electrons. Thus Eq. 3.11 has to be modified into

$$\begin{aligned} n_s = &\int_{E_1}^{\infty} \frac{m_e^*}{\pi\hbar^2} \frac{1}{e^{\frac{E-E_F}{kT}} + 1} \left[1 - \frac{2(E - E_C^s)}{E_g}\right] dE \\ + &\int_{E_2}^{\infty} \frac{m_e^*}{\pi\hbar^2} \frac{1}{e^{\frac{E-E_F}{kT}} + 1} \left[1 - \frac{2(E - E_C^s)}{E_g}\right] dE. \end{aligned} \tag{3.12}$$

to adapt this two-subband structure. According to Eq. 3.12 E_1 and E_2 are derived to be 64 meV and 21 meV below E_F respectively. From Eqs. 3.10, 3.12, and 3.13, F can be attained as 3.0×10^4 V/cm, which is reasonably below the breakdown field of InAs ($\sim 5.0 \times 10^4$ V/cm). Together calculated out with F, the width of the triangular well w_T is $\sim$ 40 nm. A good correspondence is shown between w_T and the surface electron Fermi wavelength λ_F^s of 20 nm determined by $\lambda_F = \sqrt{\frac{2\pi}{n_s}}$. w_T is about twice of λ_F and can be taken as the thickness of the surface layer.

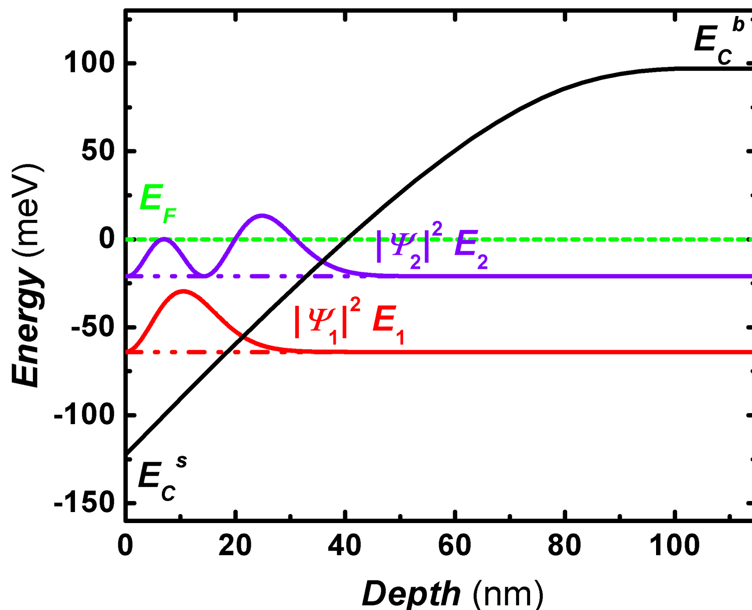

Figure 3.7: (Color online) Room temperature schematic band structure at the surface of sample YZ01, where the 2DES has two occupied subbands [the energy levels are explained in the text, and $|\Psi_i|^2$ (i = 1, 2) represents the probability density (in arbitrary units, with $|\Psi_i|^2 = 0$ taken at the E_i line)].

$$eFw_T = E_F - E_C^s = (E_F - E_1) + (E_1 - E_C^s) = 0.080\ \text{eV} + \left(\frac{9\pi^2}{8m_e^*}\right)^{\frac{1}{3}} \left(\frac{3}{4}e\hbar F\right)^{\frac{2}{3}}. \quad (3.13)$$

Figure 3.7 depicts the band structure and the probability density ($|\Psi|^2$) associated with the surface electron wave functions at room temperature. E_1, E_2, E_3, and E_F are calculated to be 56 meV, 99 meV, 130 meV, and 120 meV respectively above E_C^s. $E_3 > E_F$ indicates the third subband is not populated. From the above calculations, a downward band-bending of 217 meV at the InAs surface is obtained, as well as the electron densities of two surface subbands $n_{s1} = 1.04 \times 10^{12}$ cm^{-2} and $n_{s2} = 0.46 \times 10^{12}$ cm^{-2}. In quantum physics regime, electrons exhibit wave-like properties. The dissimilar wave functions of two surface subbands in Fig. 3.7 experience different scatterings from phonons and ionized impurities, which determines their mobilities. For some reasons, the difference between electron mobilities of two surface subbands is so small that they can be presumed to share the same mobility to perform the three-band fitting rather than four-band. We intentionally avoided the four-band fitting because more fitting parameters would make themselves individually less unique due to the increased fitting freedom.

3.2.2 Moderately Doped n-type InAs

Changes Due to Heavier Doping

Figure. 3.8 demonstrates R_{xx}, R_{yy} and R_{xy} of the moderately doped n-type InAs sample (YZ02). Like YZ01, the quadratic dependence of R_{xx} and R_{yy} on B and non-linearity of the Hall resistance are observed. Three types of electrons are also expected here, which are from the surface, the bulk, and the nucleation layer. YZ02 is more heavily doped than YZ01, so the position of E_F in the bulk is higher, but still below E_C^b. The formation of the surface band structure is similar to YZ01. A comparison of E_F between YZ01 and YZ02 is illustrated in Fig. 3.9. The raised E_F in the bulk of YZ02 enlarges the shaded area which represents the accumulation layer as schematically described in Fig. 3.9, is thus qualitatively anticipated to increase n_s.

Figures 3.8(a) and 3.8(b) also show an anisotropy in MR of YZ02 Van der Pauw. Thereby R_d is engaged for the three-band fitting. Three sets of μ and n are extracted from fitting R_d and R_{xy}, which are

$$\begin{cases} \mu_1 = 5600 \text{ cm}^2/\text{Vs} \\ n_1 = 3.2 \times 10^{12} \text{ cm}^{-2} \end{cases}, \quad \begin{cases} \mu_2 = 23000 \text{ cm}^2/\text{Vs} \\ n_2 = 2.5 \times 10^{12} \text{ cm}^{-2} \end{cases}, \quad \text{and} \quad \begin{cases} \mu_3 = 2200 \text{ cm}^2/\text{Vs} \\ n_3 = 7.0 \times 10^{12} \text{ cm}^{-2} \end{cases}. \tag{3.14}$$

According to the n and μ assignation of YZ01, we assign μ_s = 5600 cm^2/Vs, n_s = 3.2$\times$10^{12} cm^{-2}, μ_b = 23000 cm^2/Vs, n_b = 2.5$\times$10^{12} cm^{-2}, μ_n = 2200 cm^2/Vs, and n_n = 7.0$\times$10^{12} cm^{-2}. The size relation of n_s between YZ01 and YZ02 is consistent with the qualitative anticipation from above. The similar nucleation layer transport properties between YZ01 and YZ02 are the results from their identical growth condition, which further confirm our assignation.

Surface Band Structure

The surface electron Fermi wavelength is 14 nm as determined from n_s, and like YZ01 we approximate $w_T = 2\lambda_F^s$ for the later band-bending calculation. With n_b divided by the thickness of the bulk layer, $n_{b3\text{D}}$ is derived as 1.4×10^{16} cm^{-3}, which is about 5 times of $n_{b3\text{D}}$ of YZ01. The Fermi level is then calculated to be 55 meV below E_C^b by integrating from E_C^b to infinity with consideration of non-parabolic energy dispersion and Fermi-Dirac distribution in 3D case (Eq. 3.9). The additional donors in YZ02 provide more electrons, therefore E_F in the bulk is raised compared with the one of YZ01. In Table 2.1, the donor concentration is listed as 1.38×10^{16} cm^{-3}, consistent with $n_{b3\text{D}}$ obtained from the three-band fitting. A triangular well is still applied here to analyze the states of electrons at the surface. From n_s and Eq. 3.12 E_1 is derived to be 117 meV below E_F, which can be substituted into Eq. 3.13 to determine $F = 8.1 \times 10^4$ V/cm. Respect to the approximation of the triangular

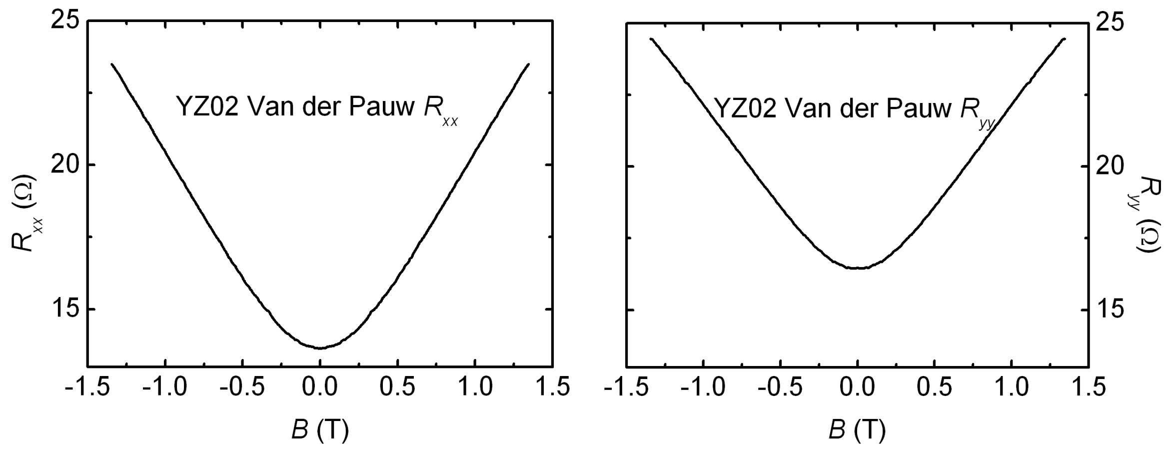

(a) Longitudinal MR of YZ02 Van der Pauw along $\hat{x}$.

(b) Longitudinal MR of YZ02 Van der Pauw along $\hat{y}$.

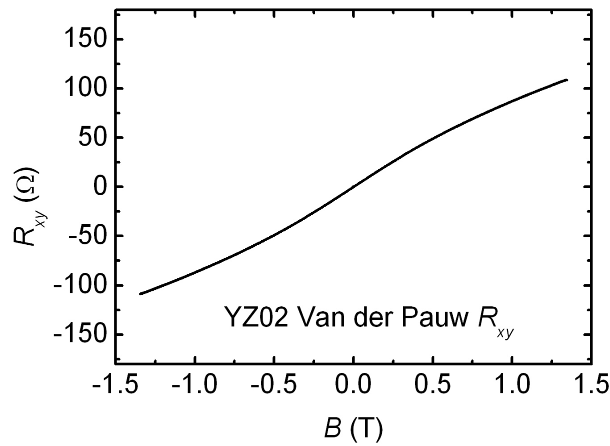

(c) Transverse MR of YZ02 Van der Pauw

Figure 3.8: YZ02 Van der Pauw magneto-transport measurements at $T = 300$ K

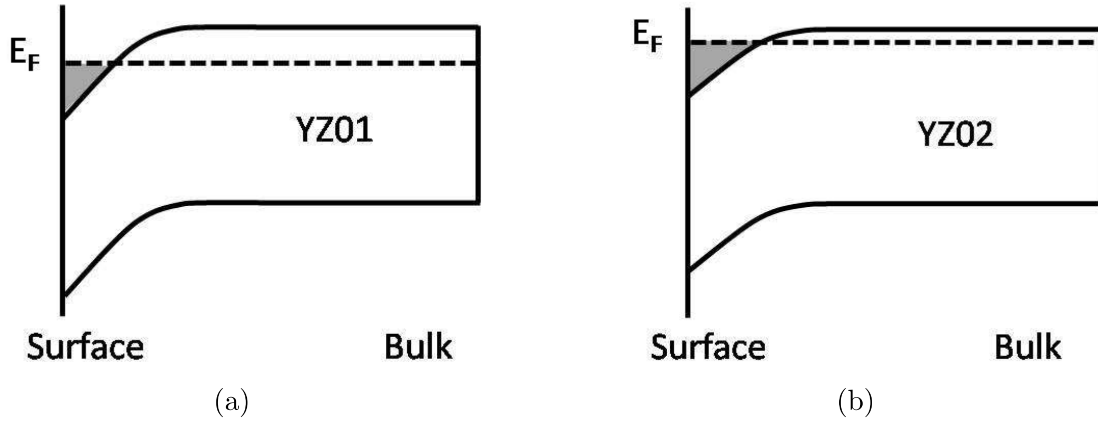

Figure 3.9: Schematic band structures of YZ01 and YZ02 to demonstrate the positions of E_F in the bulk. The shaded area is the accumulation layer, and YZ02 is expected to have more surface electrons due to the larger shaded area.

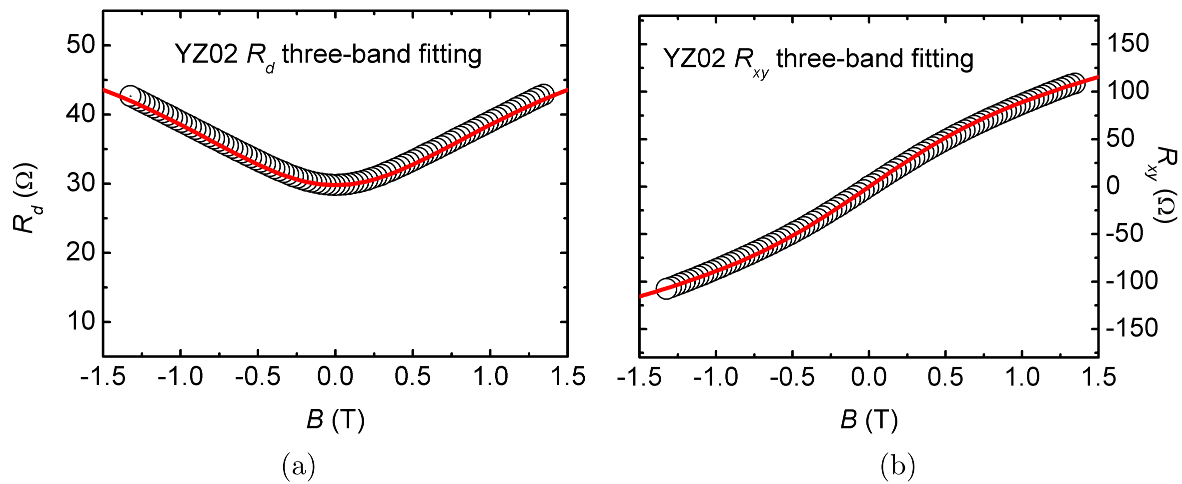

Figure 3.10: (Color online) (a) R_d and (b) R_{xy} data of YZ02 Van der Pauw at $T = 300$ K. The circles are experimental values (For clarity, 1 out of 16 experimental points only are plotted). Red solid lines are fitted curves from the three-band fitting.

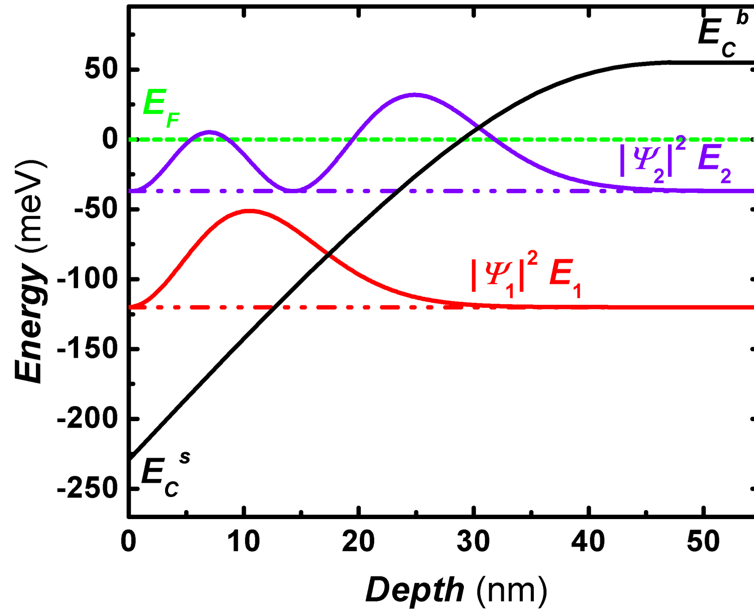

Figure 3.11: (Color online) Room temperature schematic band structure at the surface of sample YZ02, where the 2DES has two occupied subbands [the energy levels are explained in the text, and $|\Psi_i|^2$ (i = 1, 2) represents the probability density (in arbitrary units, with $|\Psi_i|^2 = 0$ taken at the E_i line).

well model, in reality F can be a couple times lower than the calculated value and safely below the breakdown field of InAs. With the value of F, from Eq. 3.10 E_1, E_2, E_3, and E_F are calculated to be 109 meV, 192 meV, 260 meV, and 229 meV respectively above E_C^s. At the surface YZ02, the first two subbands are also populated with $n_{s1} = 2.32 \times 10^{12}$ cm^{-2} and $n_{s2} = 0.78 \times 10^{12}$ cm^{-2}. The wave functions of the two surface subbands and a downward band-bending of 284 meV are shown in Fig. 3.11. We notice that both μ_s and μ_b of YZ02 are lower than the ones of YZ01, which can be explained by more ionized impurity scatterings introduced by heavier doping.

3.2.3 Heavily Doped n-type InAs

Degenerated Bulk

The range of R_{xx} and R_{yy} shown in Figs. 3.12(a) and 3.12(b) for the heavily doped n-type InAs sample (YZ03) are negligible compared with YZ01 and YZ02. Among the three types of electrons (surface, bulk, and nucleation layer), the flat parabolic backgrounds indicate only one of them is dominant in this three-band system, consistent with the linear Hall signal in Fig. 3.12 (c). For the surface accumulation and the nucleation layer electrons, both n_s and n_n are on the order of 10^{12} cm^{-2}, plus μ_s and μ_n around $1000 - 5000$ cm^2/Vs. In contrast, the

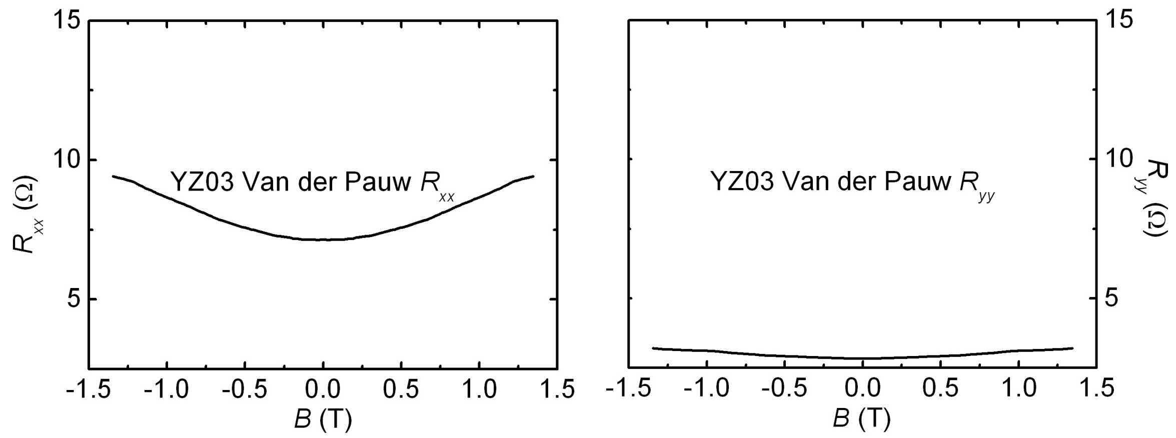

(a) Longitudinal MR of YZ03 Van der Pauw along $\hat{x}$.

(b) Longitudinal MR of YZ03 Van der Pauw along $\hat{y}$.

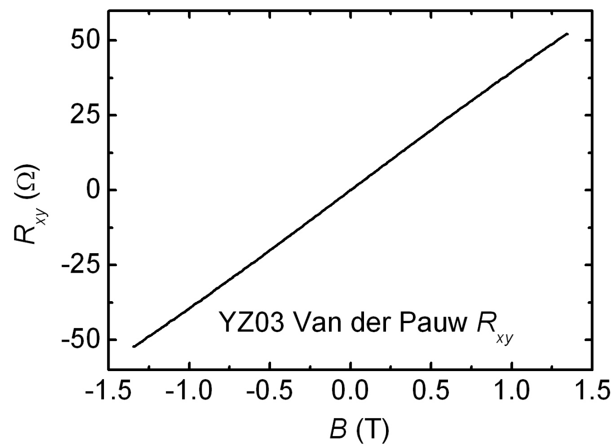

(c) Transverse MR of YZ03 Van der Pauw

Figure 3.12: YZ03 Van der Pauw magneto-transport measurements at $T = 300$ K

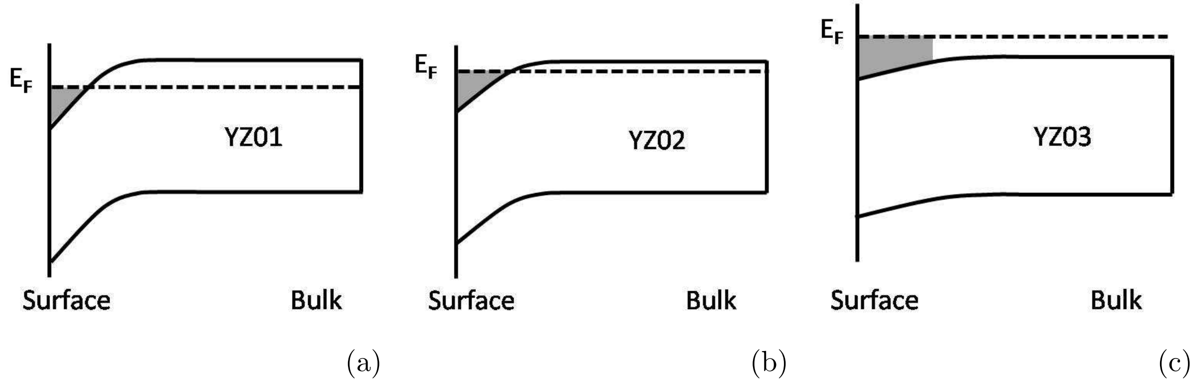

(a) (b) (c)

Figure 3.13: Schematic band structures of YZ01, YZ02, and YZ03 to demonstrate the rising of E_F in the bulk due to the increased doping. The shaded area is the accumulation layer. Compared with YZ01 and YZ02, there is less potential confinement on the YZ03 surface layer.

~ 2 μm thick bulk InAs doped with Si at $\sim 10^{17}$ cm^{-3} has $n_b \sim 10^{13}$ cm^{-2} and $\mu_b \sim 20000$ cm^2/Vs. Therefore, the conductivities of the surface accumulation and the nucleation layer are overwhelmed by the bulk layer conductivity (about two orders of magnitude smaller). Thus the dominant population of electrons sensed in the transport measurements shown in Fig. 3.12 is ascribed to the bulk electrons.

In lightly and moderately doped n-type semiconductors, the dopant atoms create individual donor levels E_d that can often be considered as localized states which donate electrons by thermal excitation to the conduction band. At high donor concentrations the Bohr radii of the dopant electrons overlap and a splitting of E_d will be observed, which may further spread out into a whole donor band. At sufficiently high levels of doping, the donor band becomes so broad that it merges with the conduction band minimum. As a result E_g is reduced and E_F is located inside the conduction band [18]. Such a semiconductor is called a degenerate semiconductor, and it exhibits electrical properties similar to those of a metal. Typically a semiconductor is defined as non-degenerate if E_F is $\sim 2k_BT$ below E_C^b, which is satisfied by YZ01 and YZ02 at room temperature. When E_F is closer to E_C^b than $\sim k_BT$, properties of degenerate semiconductors have to be considered. Table 2.1 shows the donor concentration is 11.5×10^{16} cm^{-3}. Assuming $n_{b3\mathrm{D}}$ equals to the donor concentration, then E_F in the bulk can be calculated to be 6.4 meV above E_C^b through Eq. 3.9, which indicates YZ03 is a degenerate n-type semiconductor. Figure 3.13 demonstrates the position of E_F in the bulk becomes higher as dopant concentration increases. As a result, there will be less downward band-bending with heavier doping. And the decreased barrier height will cause more surface electrons spilled into the bulk until the whole system becomes mono-band at an extremely high doping level.

The three-band fitting of R_d and R_{xy} are shown in Figs. 3.14(a) and 3.14(b) and the transport properties of each layer are obtained as

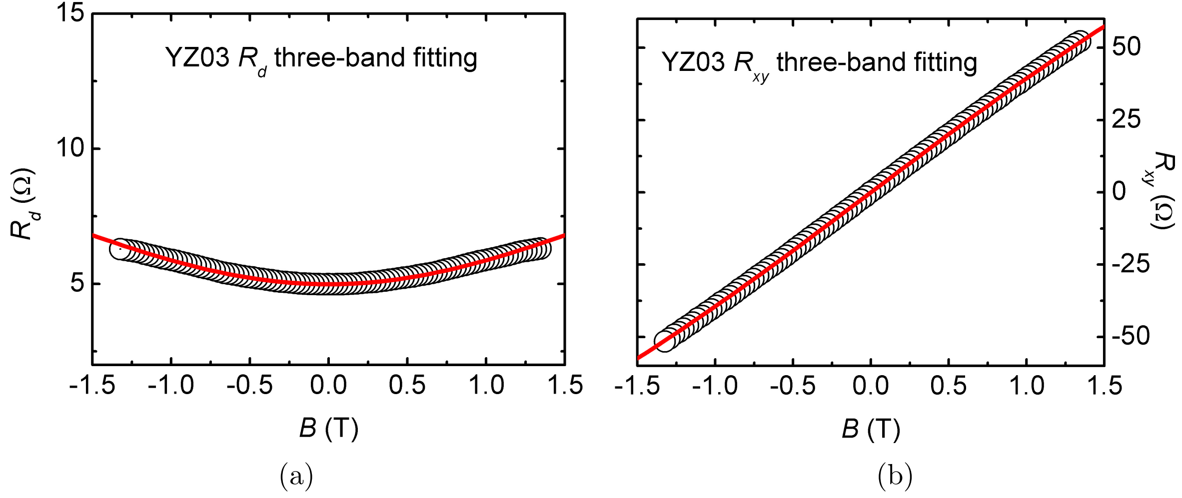

(a) (b)

Figure 3.14: (Color online) (a) R_d and (b) R_{xy} data of YZ03 Van der Pauw at T = 300 K. The circles are experimental values (For clarity, 1 out of 16 experimental points only are plotted). Red solid lines are fitted curves from the three-band fitting.

$$\begin{cases} \mu_s = 2900 \text{ cm}^2/\text{Vs} \\ n_s = 2.5 \times 10^{12} \text{ cm}^{-2} \end{cases}, \quad \begin{cases} \mu_b = 20000 \text{ cm}^2/\text{Vs} \\ n_b = 14 \times 10^{12} \text{ cm}^{-2} \end{cases}, \quad \text{and} \quad \begin{cases} \mu_n = 2100 \text{ cm}^2/\text{Vs} \\ n_n = 6.9 \times 10^{12} \text{ cm}^{-2} \end{cases}. \tag{3.15}$$

The bulk conductivity is almost two orders of magnitude larger than the conductivities of the other two layers, which confirms the above discussion. The nucleation layer parameters are consistent with those of YZ01 and YZ02. Increased dopants in the bulk involve more ionized impurities, thus μ_b and μ_s are further decreased compared with YZ01 and YZ02.

Surface Band Structure

From n_b and the test layer thickness of YZ03(Table 2.1), $n_{b3\text{D}}$ is derived to be 7.0×10^{16} cm^{-3}, $\sim$ 60% of the amount of donors, which is unlike YZ01 and YZ02 with $n_{b3\text{D}} \sim$ the donor concentration. Actually it is also possible that not all of the donors are ionized in YZ01 and YZ02 neither. Considering the effects from the UID donors ($\sim 10^{16}$ cm^{-3}) during the growth and the intrinsic electrons at room temperature ($\sim 0.1 \times 10^{16}$ cm^{-3}), it is still plausible to have free bulk electrons in comparable amount with donors for YZ01 and YZ02. But not for YZ03 because its donor concentration is at least one order of magnitude higher than the UID donors and intrinsic electrons. With this $n_{b3\text{D}}$ from three-band fitting, the Fermi level is rederived to be 9.3 meV below the E_C^b, which is within one k_BT at room temperature and YZ03 is still considered as a degenerate semiconductor. The decreased band-bending causes a smaller F in the triangular well model, thus lowers the potential barrier. As a result, surface electrons are more likely moving into the bulk, which explains why YZ03 possesses

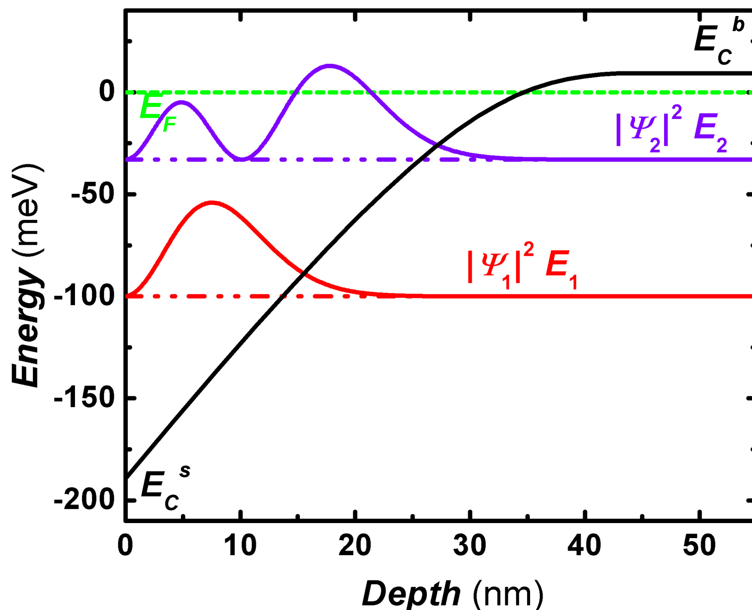

Figure 3.15: (Color online) Room temperature schematic band structure at the surface of sample YZ03, where the 2DES has two occupied subbands [the energy levels are explained in the text, and $|\Psi_i|^2$ (i = 1, 2) represents the probability density (in arbitrary units, with $|\Psi_i|^2 = 0$ taken at the E_i line).

the largest shaded area but owns fewer surface electrons than YZ02. The accumulation layer thickness is determined as $\sim 2\lambda_F^s = 32$ nm and taken as the width of the triangular potential well. The calculated band structure is shown in Fig. 3.15 with $F = 5.9 \times 10^4$ V/cm, and E_1, E_2, E_3, and E_F being 88 meV, 155 meV, 210 meV, and 188 meV respectively above E_C^s, implying a two-subband system with $n_{s1} = 1.83 \times 10^{12}$ cm^{-2} and $n_{s2} = 0.67 \times 10^{12}$ cm^{-2}.

3.3 Liquid Nitrogen Temperature Band Structure

3.3.1 Lightly Doped n-type InAs

Figure 3.16 shows the electronic transport measurements of YZ01 at T = 82 K. From the cooldown history in Fig. 3.1, the minimum of the longitudinal resistance is close to this temperature. For a typical semiconductor, its resistance is supposed to increase as T decreases simply due to less thermal excitation to generate free electrons. However, our n-type InAs samples are narrow-gap semiconductors with shallow donors of Si whose E_d is only about 1 meV below E_C^b [15]. Thus even at liquid nitrogen temperature, there is still enough thermal promotion ($k_BT \sim 10$ meV) to keep the amount of free electrons unvaried. On the other hand, the carrier mobilities will be improved due to less phonon scatterings at lower temper-

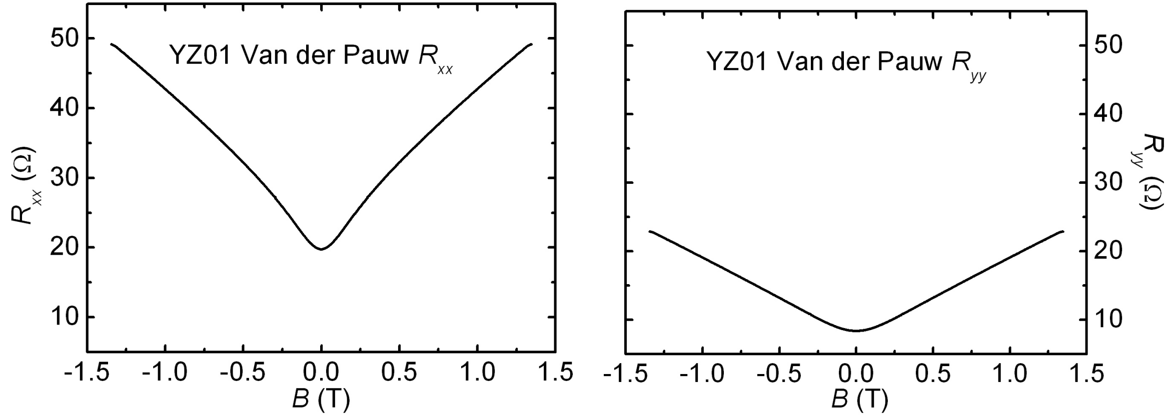

(a) Longitudinal MR of YZ01 Van der Pauw along $\hat{x}$.

(b) Longitudinal MR of YZ01 Van der Pauw along $\hat{y}$.

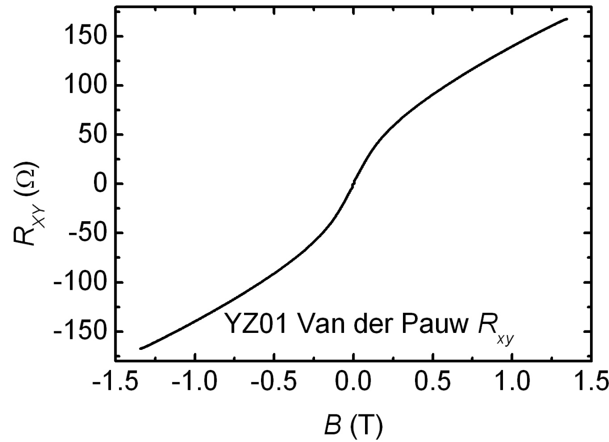

(c) Transverse MR of YZ01 Van der Pauw

Figure 3.16: YZ02 Van der Pauw magneto-transport measurements at $T = 82$ K

atures. As a result, the conductivity $\sigma = ne\mu$ increases as T decreases till ~ 80 K. At about 80 K, the Coulomb scatterings from the impurities start exceeding the phonon scatterings and becoming more robust when the temperature is further lowered because less thermal populating of the free electrons produces less screening effect. Therefore, below ~ 80 K, the electron mobility drops as T decreases, as well as the conductivity. In brief, the non-trivial temperature dependence of the resistance exhibited during the cooldown is mainly caused by the variance of the electron mobility rather than the density.

Fitting R_d and R_{xy} (Figs. 3.17(a) and 3.17(b)) with the three-band theory, three sets of μ and n are extracted

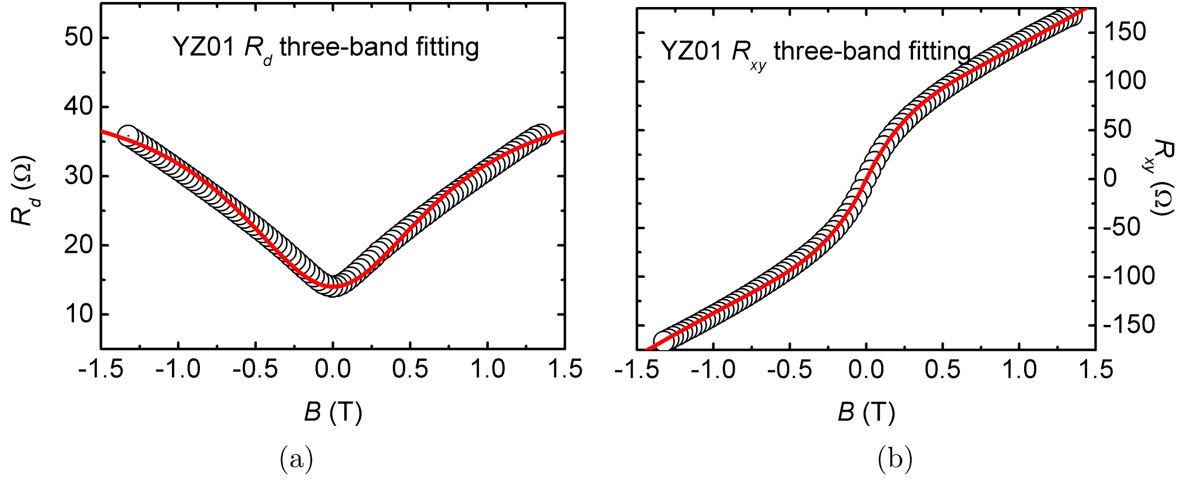

Figure 3.17: (Color online) (a) R_d and (b) R_{xy} data of YZ01 Van der Pauw at T = 82 K. The circles are experimental values (For clarity, 1 out of 16 experimental points only are plotted). Red solid lines are fitted curves from the three-band fitting.

$$\begin{cases} \mu_1 = 30000 \text{ cm}^2/\text{Vs} \\ n_1 = 1.2 \times 10^{12} \text{ cm}^{-2} \end{cases}, \quad \begin{cases} \mu_2 = 109000 \text{ cm}^2/\text{Vs} \\ n_2 = 0.37 \times 10^{12} \text{ cm}^{-2} \end{cases}, \quad \text{and} \quad \begin{cases} \mu_3 = 4200 \text{ cm}^2/\text{Vs} \\ n_3 = 6.5 \times 10^{12} \text{ cm}^{-2} \end{cases}. \tag{3.16}$$

Based on the electron densities we assigned to each layer of YZ01 at room temperature, carrier 1, 2, and 3 are attributed to electrons from the surface accumulation layer, the bulk layer, and the nucleation layer respectively. Compared with the properties at room temperature, μ_s, μ_b, and μ_n all become several times larger while n_s, n_b and n_n all slightly drop. The band gap increases to 404 meV at T = 82 K [19]. Three-dimensional bulk electron density is obtained as 0.25×10^{16} cm^{-3}, thus E_F is calculated to be only 12 meV below E_C^b. The increase of E_F in the bulk compared with the room temperature result is from the considerable reduction of k_BT, consistent with previous studies on E_F versus T for different concentrations of shallow donors in InAs [20]. At the surface, λ_F^s changed into 24 nm. In the triangular potential well, E_1 and E_2 are 61 meV and 25 meV both below E_F, whereas E_3 is 6 meV above. The first two subbands are occupied with $n_{s1} = 0.88 \times 10^{12}$ cm^{-2} and $n_{s2} = 0.32 \times 10^{12}$ cm^{-2}. The width of the potential well is taken as $\sim 2\lambda_F^s = 48$ nm, therefore, the electric field is 2.4×10^4 V/cm. The position of E_F is 110 meV above E_C^s, which is about the same as at room temperature (120 meV). The band structure and the electron wave functions are shown in Fig. 3.18.

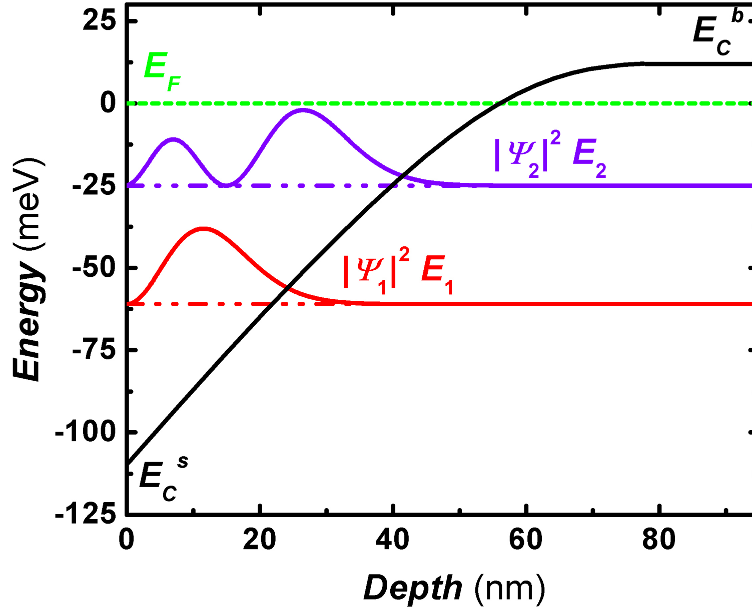

Figure 3.18: (Color online) At $T = 82$ K, schematic band structure at the surface of sample YZ01, where the 2DES has two occupied subbands [the energy levels are explained in the text, and $|\Psi_i|^2$ ($i = 1, 2$) represents the probability density (in arbitrary units, with $|\Psi_i|^2 = 0$ taken at the E_i line)].

3.3.2 Moderately Doped n-type InAs

Magnetoresistance and Hall measurements of YZ02 at $T = 82$ K are displayed in Fig. 3.19. After the three-band fitting (Figs. 3.20(a) and 3.20(b)), we have

$$\begin{cases} \mu_s = 9500\ \text{cm}^2/\text{Vs} \\ n_s = 2.6 \times 10^{12}\ \text{cm}^{-2} \end{cases}, \quad \begin{cases} \mu_b = 49000\ \text{cm}^2/\text{Vs} \\ n_b = 2.2 \times 10^{12}\ \text{cm}^{-2} \end{cases}, \quad \text{and} \quad \begin{cases} \mu_n = 2600\ \text{cm}^2/\text{Vs} \\ n_n = 6.0 \times 10^{12}\ \text{cm}^{-2} \end{cases}. \tag{3.17}$$

Like YZ01, n_s, n_b and n_n of YZ02 also slightly drop, whereas μ_s, μ_b, and μ_n all improve due to less phonon scatterings, but the improvements are not as much as the ones of YZ01 because of more ionized impurity scatterings. E_F is derived to be 0.8 meV above E_C^b to provide $n_{b3\text{D}} = 1.2 \times 10^{16}$ cm^{-3}. YZ02 apparently becomes degenerate, which agrees with the previous data [20]. In the triangular potential well, E_1, E_2, E_3, and E_F are 98 meV, 171 meV, 233 meV, and 207 meV respectively above E_C^s with the first two subbands electron densities of $n_{s1} = 2.0 \times 10^{12}$ cm^{-2} and $n_{s2} = 0.60 \times 10^{12}$ cm^{-2}. The electric field is decreased to 6.9×10^4 V/cm compared with $F = 8.1 \times 10^4$ V/cm at room temperature. The band structure and the electron wave functions are shown in Fig. 3.21.

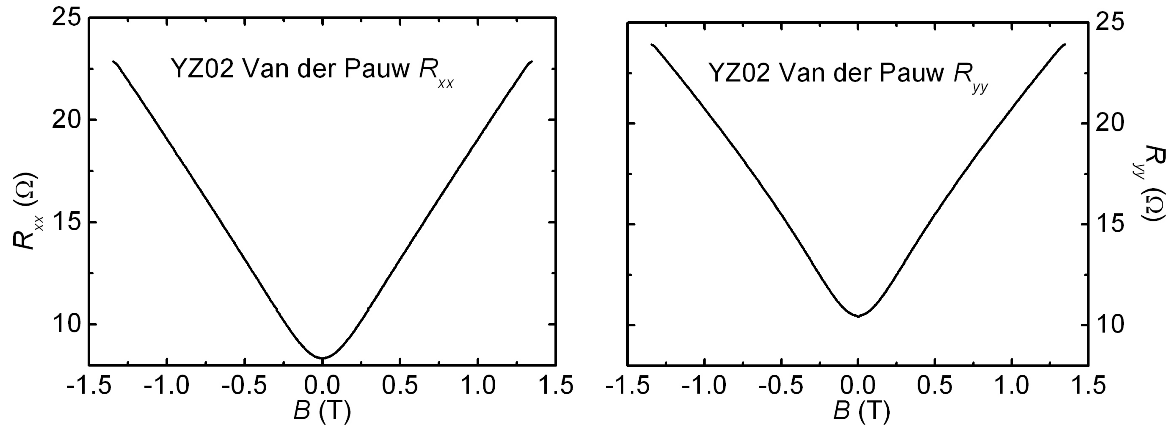

(a) Longitudinal MR of YZ02 Van der Pauw along $\hat{x}$.

(b) Longitudinal MR of YZ02 Van der Pauw along $\hat{y}$.

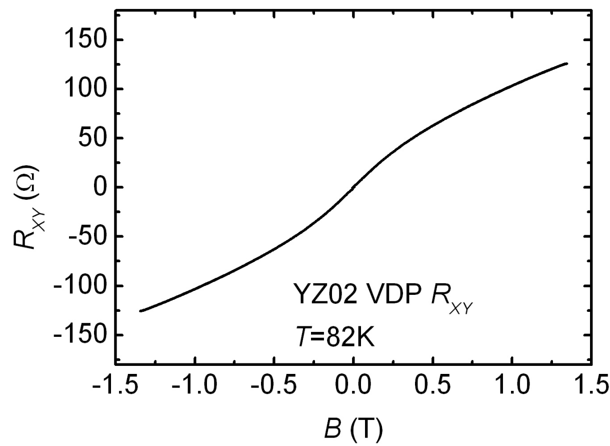

(c) Transverse MR of YZ02 Van der Pauw

Figure 3.19: YZ02 Van der Pauw magneto-transport measurements at $T = 82$ K

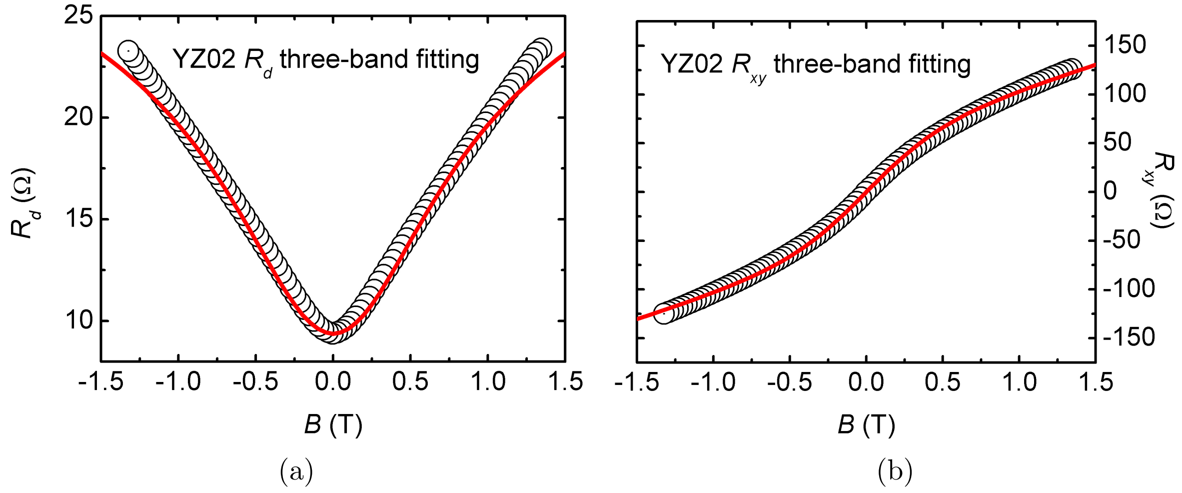

Figure 3.20: (Color online) (a) R_d and (b) R_{xy} data of YZ02 Van der Pauw at $T = 82$ K. The circles are experimental values (For clarity, 1 out of 16 experimental points only are plotted). Red solid lines are fitted curves from the three-band fitting.

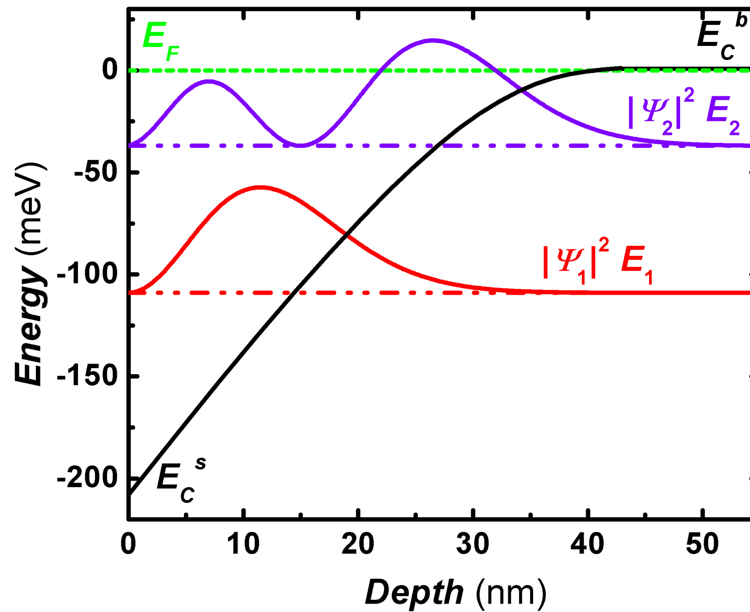

Figure 3.21: (Color online) At $T = 82$ K, schematic band structure at the surface of sample YZ02, where the 2DES has two occupied subbands [the energy levels are explained in the text, and $|\Psi_i|^2$ ($i = 1$, 2) represents the probability density (in arbitrary units, with $|\Psi_i|^2 = 0$ taken at the E_i line).

3.3.3 Heavily Doped n-type InAs

The symmetrized MR and the antisymmetrized Hall measurements data of YZ03 at $T = 80$ K indicate a dominant carrier type in the system (Fig. 3.22). Three-band fittings on R_d and R_{xy} (Fig. 3.23(a) and 3.23(b)) provide us

$$\begin{cases} \mu_s = 5600 \text{ cm}^2/\text{Vs} \\ n_s = 2.1 \times 10^{12} \text{ cm}^{-2} \end{cases}, \quad \begin{cases} \mu_b = 28000 \text{ cm}^2/\text{Vs} \\ n_b = 12.1 \times 10^{12} \text{ cm}^{-2} \end{cases}, \quad \text{and} \quad \begin{cases} \mu_n = 2400 \text{ cm}^2/\text{Vs} \\ n_n = 5.9 \times 10^{12} \text{ cm}^{-2} \end{cases}. \tag{3.18}$$

Consistent with YZ01 and YZ02, n_s, n_b and n_n of YZ03 slightly drop as well, whereas μ_s, μ_b, and μ_n all increase. YZ03 contains the most ionized impurity scatterings, which corresponds to the lowest mobilities among three samples. YZ03 is suggested to be more degenerate than YZ02 because its E_F is 20 meV above E_C^b. In the triangular potential well, E_1, E_2, E_3, and E_F are 80 meV, 141 meV, 191 meV, and 174 meV respectively above E_C^s with the first two subbands electron densities of $n_{s1} = 1.61 \times 10^{12}$ cm^{-2} and $n_{s2} = 0.49 \times 10^{12}$ cm^{-2}. The electric field is decreased to 5.1×10^4 V/cm. The band structure and the electron wave functions are shown in Fig. 3.24.

3.4 Liquid Helium Temperature Band Structure

3.4.1 Shubnikov-de Haas Oscillation

In the conduction band of a metal or a high quality narrow-gap semiconductor with large electron mobilities, the free electrons will behave like simple harmonic oscillators under a strong magnetic field when T is sufficiently low. As a result, the energies are degenerated into Landau levels as $E_n = (n - \dfrac{1}{2})\hbar\omega_c$ where n and $\omega_c = eB/m_e^*$ are a positive integer and the cyclotron frequency. Due to the external magnetic fields, the free electrons are localized within a circle with radius of one magnetic length $l_B = \sqrt{\dfrac{2\hbar}{eB}}$. Each Landau level contains $\dfrac{1}{\pi l_B^2} = \dfrac{eB}{2\pi\hbar}$ electron states per unit area. The electron transfer to lower Landau levels can occur because the degeneracy increases as B is raised. Figure 3.25 explains the origin of Shubnikovde Haas Oscillation [21]. At $B = 0$, free electrons occupy energy levels up to E_F without any degeneracy as shown in region (b). In (a) the field has a value B_1 such that integer levels are completely filled and the total energy is the same as in the absence of B: as many electrons have their energy raised as lowered by the orbital quantization under B_1. As increasing B further, the total electron energy is increased as the uppermost electrons have their energy raised. At B_2, the last level is half occupied and the total

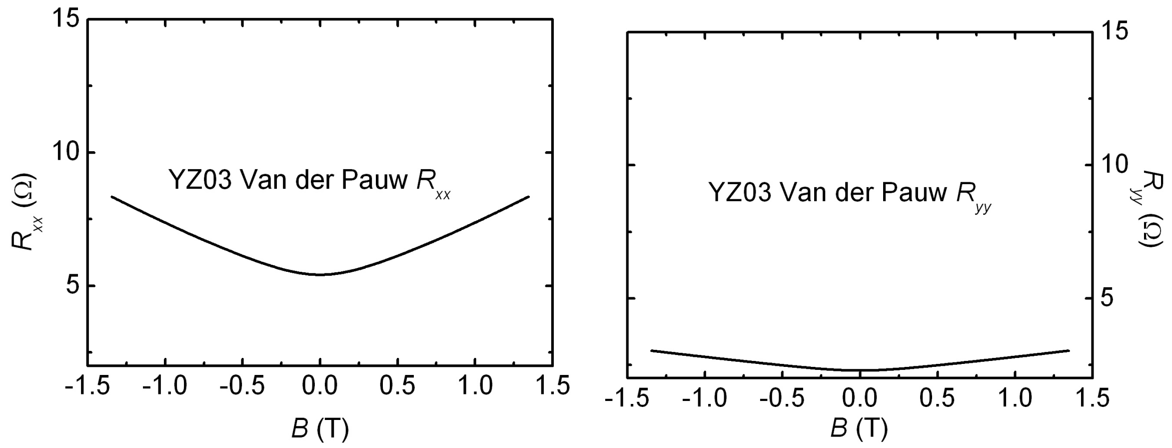

(a) Longitudinal MR of YZ03 Van der Pauw along $\hat{x}$.

(b) Longitudinal MR of YZ03 Van der Pauw along $\hat{y}$.

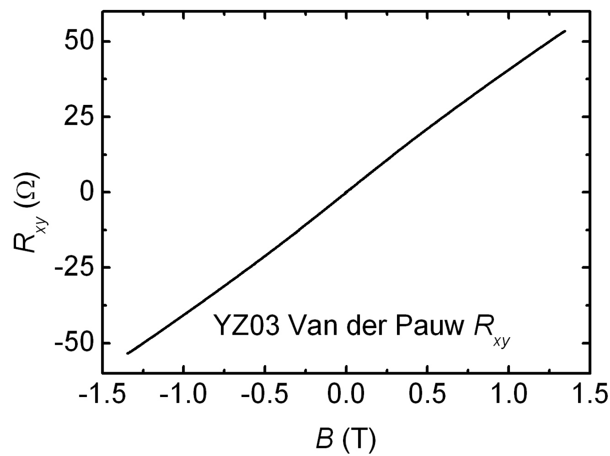

(c) Transverse MR of YZ03 Van der Pauw

Figure 3.22: YZ03 Van der Pauw magneto-transport measurements at $T = 80$ K

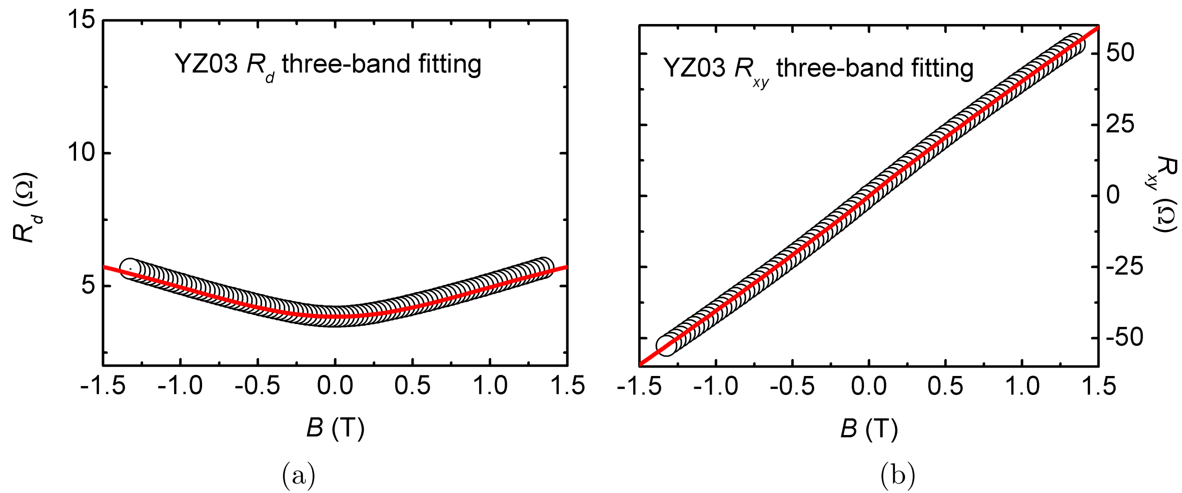

Figure 3.23: (Color online) (a) R_d and (b) R_{xy} data of YZ03 Van der Pauw at $T = 80$ K. The circles are experimental values (For clarity, 1 out of 16 experimental points only are plotted). Red solid lines are fitted curves from the three-band fitting.

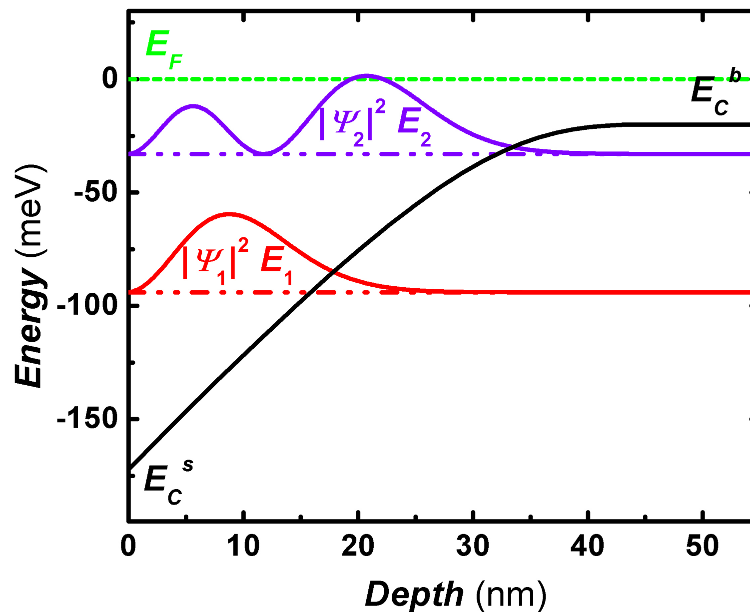

Figure 3.24: (Color online) At $T = 80$ K, schematic band structure at the surface of sample YZ03, where the 2DES has two occupied subbands [the energy levels are explained in the text, and $|\Psi_i|^2$ ($i = 1, 2$) represents the probability density (in arbitrary units, with $|\Psi_i|^2 = 0$ taken at the E_i line).

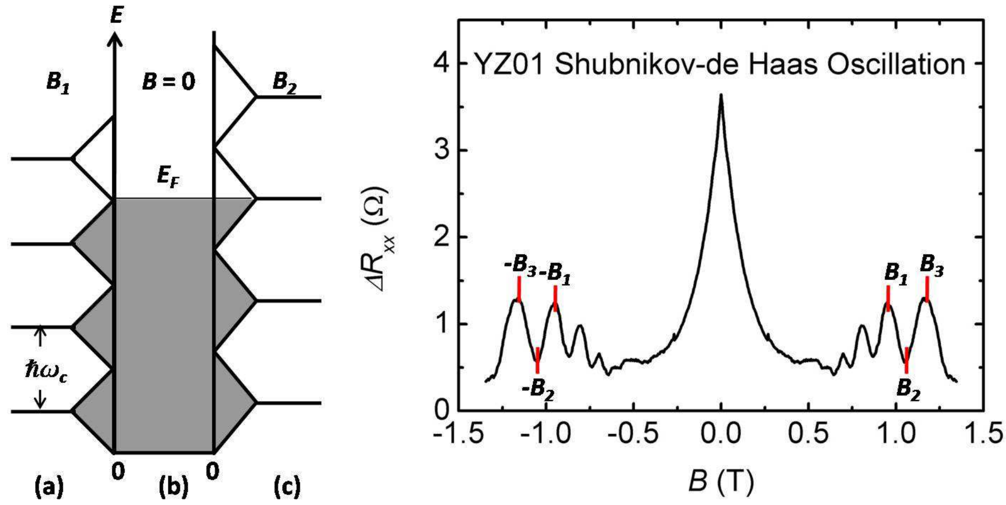

Figure 3.25: (Color online) Left panel: Explanation of the de Haas-van Alphen effect with filled orbitals of the Fermi sea shaded. Right panel: Shubnikovde Haas Oscillation of YZ01 at $T = 4.5$ K, parabolic background of R_{xx} is subtracted to obtain better resolution. B_1 and B_3 indicate where the minimum energy occur while B_2 signifies the maximum.

energy reaches a maximum whereas at B_1 the total energy is a minimum. The maximum or minimum energy will exist alternatively as we raise up B. This phenomenon is called the de Haas-van Alphen effect. The maximum or minimum energy corresponds to the lowest or highest resistance because electrons are more mobile with higher energies, thus producing a measurable oscillation in resistance known as Shubnikovde Haas Oscillation.

Suppose in a 2DES, there are j completely filled levels at $B = B_1$. Considering spin degeneracy, the 2D electron density $n_{\mathrm{2D}} = 2j\frac{eB_1}{2\pi\hbar}$. When B is increased to B_3, the degeneracy increases as well, as a result, $j-1$ levels are fully occupied. Then $n_{\mathrm{2D}} = 2(j-1)\frac{eB_3}{2\pi\hbar}$. Thereby, the oscillations occur at equal intervals of $1/B$ with $\Delta(1/B) = 1/B_1 - 1/B_3 = \frac{e}{\pi\hbar n_{\mathrm{2D}}}$. In other words, the electron density can be derived through Shubnikovde Haas Oscillation.

3.4.2 Lightly Doped n-type InAs

T = 4.5 K

In the cryogen-free cryostat system, the lowest temperature capable for a stable measurement is $T = 4.5$ K. At this temperature, oscillatory components can be observed in both MR and Hall measurements of YZ01 as displayed in Fig. 3.26. To reveal these oscillatory components, we plot the dependence of ΔR_{xx} and ΔR_{yy} on B after subtracting the parabolic background

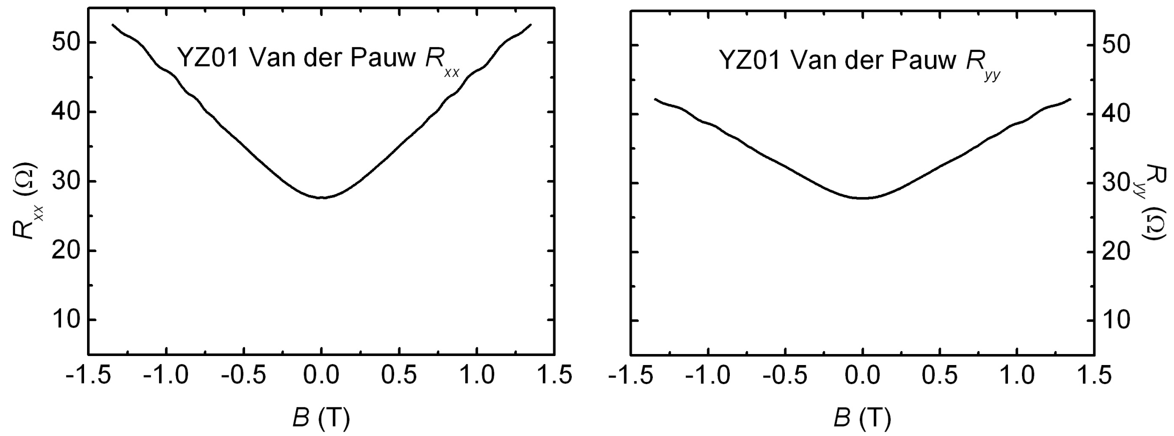

(a) Longitudinal MR of YZ01 Van der Pauw along $\hat{x}$.

(b) Longitudinal MR of YZ01 Van der Pauw along $\hat{y}$.

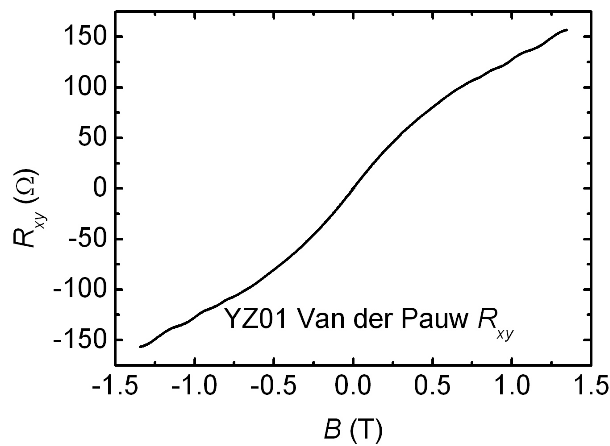

(c) Transverse MR of YZ01 Van der Pauw

Figure 3.26: YZ01 Van der Pauw magneto-transport measurements at $T = 4.5$ K

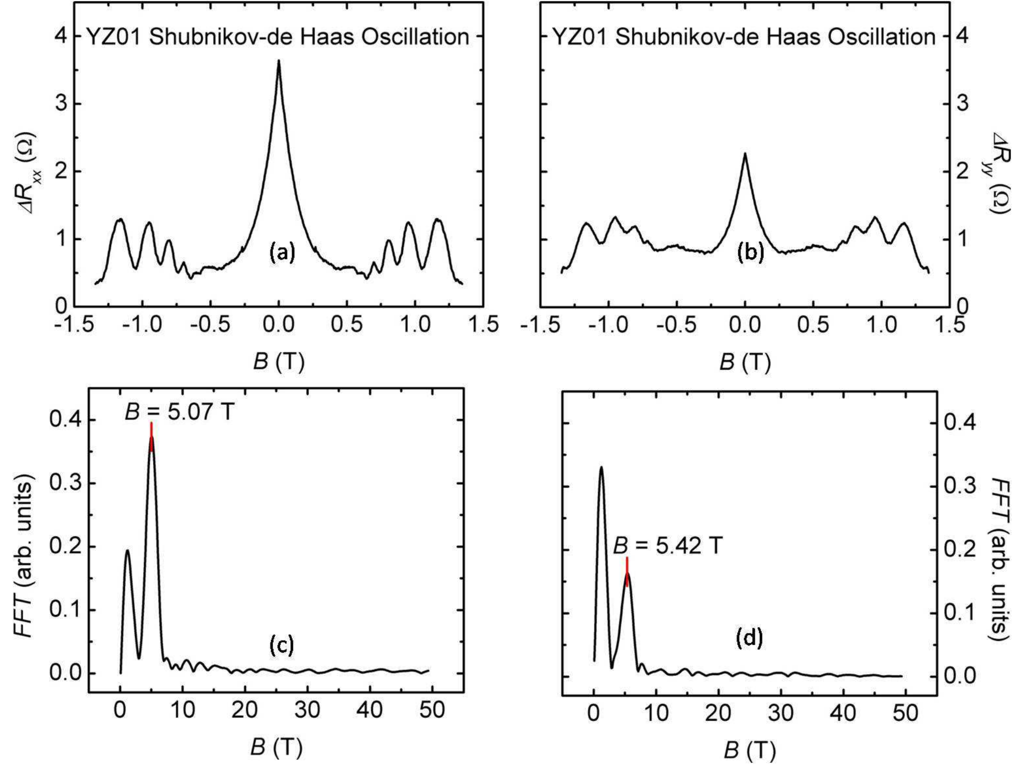

Figure 3.27: (Color online) Shubnikov-de Haas oscillations of (a) δR_{xx} and (b) δR_{yy} at $T = 4.5$ K, and parabolic backgrounds are subtracted to obtain better resolution. (c) and (d) Fast Fourier transforms (FFT) of the data in (a) and (b) respectively. The first peaks in (c) and (d) are both from background noise, and the second peaks are from the Shubnikov-de Haas oscillation, indicating a same frequency.

from R_{xx} and R_{yy} (Figs. 3.27(a) and 3.27(b)). These oscillations are attributed to the Shubnikov-de Haas effect. The fast Fourier transforms in Figs. 3.27(c) and 3.27(d) provide two close periods in $1/B$, which are 0.20 T^{-1} and 0.18 T^{-1}, implying a same carrier type. Thus, the average value 0.19 T^{-1} is taken to derive the carrier 2D density $n_{\mathrm{2D}} = 0.25 \times 10^{12}$ cm^{-2}. The oscillations start occuring at fields $B_{SdH} \sim 0.5$ T, suggesting an estimate of the carrier mobility $\sim B_{SdH}^{-1} = 20000$ $\mathrm{cm}^2\mathrm{V}^{-1}\mathrm{s}^{-1}$. From previous derived transport properties of each layer at higher temperatures, These carriers are supposed to be bulk electrons.

Transport properties of each layer are obtained as before through the three-band fittings with good qualities (Figs. 3.28(a) and 3.28(b)),

$$\begin{cases} \mu_s = 24000\ \mathrm{cm}^2/\mathrm{Vs} \\ n_s = 1.0 \times 10^{12}\ \mathrm{cm}^{-2} \end{cases}, \quad \begin{cases} \mu_b = 26000\ \mathrm{cm}^2/\mathrm{Vs} \\ n_b = 0.25 \times 10^{12}\ \mathrm{cm}^{-2} \end{cases}, \quad \text{and} \quad \begin{cases} \mu_n = 3200\ \mathrm{cm}^2/\mathrm{Vs} \\ n_n = 5.9 \times 10^{12}\ \mathrm{cm}^{-2} \end{cases}. \tag{3.19}$$

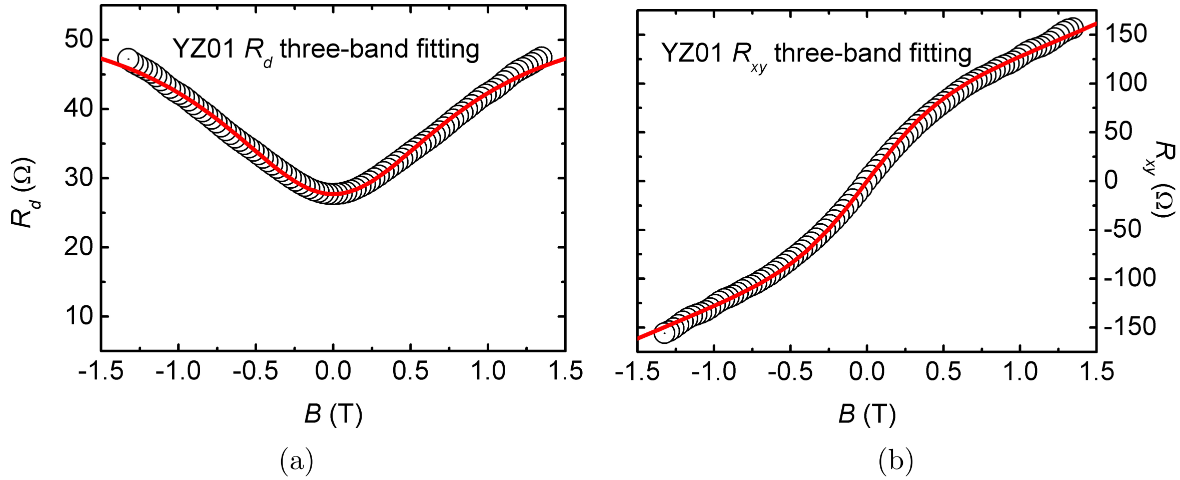

(a) (b)

Figure 3.28: (Color online) (a) R_d and (b) R_{xy} data of YZ01 Van der Pauw at T = 4.5 K. The circles are experimental values (For clarity, 1 out of 16 experimental points only are plotted). Red solid lines are fitted curves from the three-band fitting.

Both n_b and μ_b are consistent with the values analyzed through Shubnikovde Haas oscillation. These free bulk electrons from the shallow donors push E_F 2 meV above E_C^b. Compared with the properties at liquid nitrogen temperature, n_s, n_b and n_n all further decline due to less thermal excitations. The decreased densities weaken the screening effect on Coulomb scatterings, thereby μ_s, μ_b, and μ_n all drop dramatically. In the triangular well at the surface, F further decreased to 1.9×10^4 V/cm. The first two subbands are populated with $n_{s1} = 0.72 \times 10^{12}$ cm^{-2} and $n_{s2} = 0.28 \times 10^{12}$ cm^{-2}. And their eigen energies E_1 and E_2 are 54 meV and 22 meV below E_F. The band structure and the electron wave functions are shown in Fig. 3.29. Both μ_b and μ_s are sufficiently high to cause Shubnikovde Haas oscillations. Limited by the range of B in the Cryomech system, however, the oscillations from the surface electrons are not detected. Thus, the ^{3}He cryostat with maximum fields up to 10 T is needed.

T = 1.2 K

Shubnikov-de Haas oscillations have been observed at T = 4.5 K in the cryogen-free cryostat. Using the ^{3}He cryostat, the temperature can be further lowered to 1.2 K. Figure 3.30 shows the magneto-transport measurements of YZ01 at T = 1.2 K. Clearly, oscillatory components also exist in both R_{xx} and R_{yy}. A classical linear MR background due to inhomogeneities in InAs is subtracted to unveil the oscillations as plotted in Figs. 3.31(a) and 3.31(b). The fast Fourier transforms in Figs. 3.31(c) and 3.31(d) indicate two different periods in $1/B$, which are $\Delta B_\alpha^{-1} = 0.40$ T^{-1} and $\Delta B_\beta^{-1} = 0.098$ T^{-1}. Each period corresponds to a 2D density of one type of carriers, which are $n_{2D}^\alpha = 0.12\times10^{12}$ cm^{-2} and $n_{2D}^\beta = 0.49\times10^{12}$ cm^{-2}. The two different Shubinikov-de Haas oscillations start occurring at different fields. From

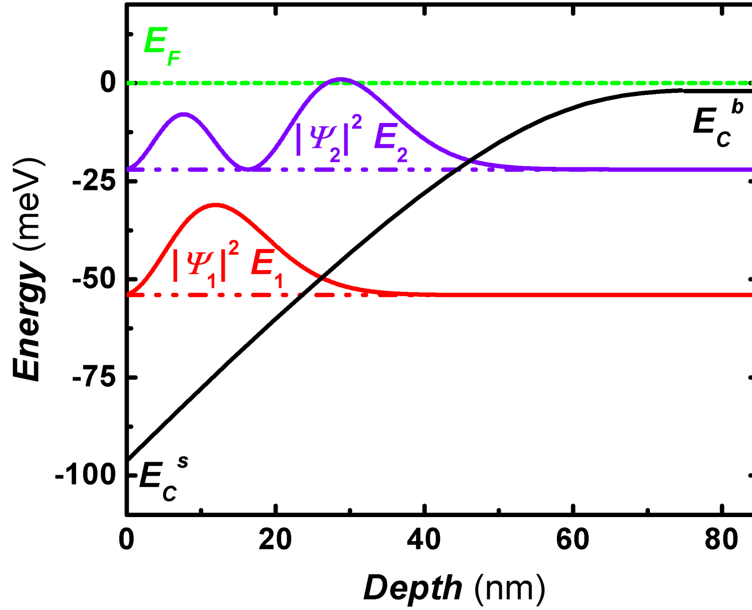

Figure 3.29: (Color online) At $T = 4.5$ K, schematic band structure at the surface of sample YZ01, where the 2DES has two occupied subbands [the energy levels are explained in the text, and $|\Psi_i|^2$ ($i = 1$, 2) represents the probability density (in arbitrary units, with $|\Psi_i|^2 = 0$ taken at the E_i line)].

Figs. 3.31(a) and 3.31(b), we obtain $B^{\alpha}_{SdH} \sim 0.3$ T and $B^{\beta}_{SdH} \sim 1$ T, providing $\mu_\alpha \sim 30000$ cm^{2}V^{-1}s^{-1} and $\mu_\beta \sim 10000$ cm^{2}V^{-1}s^{-1}. Based on the numerical values of the transport properties, we attribute α to the bulk electron and β to the surface electron.

In our InAs samples, a nonhomogenous concentration of threading dislocations formed a the highly mismatched InAs/GaAs interface generate spatial fluctuations in the mobility, causing the crossover of the MR from a parabolic to a linear B dependence [22, 23]. Thus in Figs. 3.32(a), a linear function of B is added to the three-band fitting. Mobilities and 2D electron densities of each layer are extracted as

$$\begin{cases} \mu_s = 23000 \text{ cm}^2/\text{Vs} \\ n_s = 0.69 \times 10^{12} \text{ cm}^{-2} \end{cases}, \quad \begin{cases} \mu_b = 27000 \text{ cm}^2/\text{Vs} \\ n_b = 0.17 \times 10^{12} \text{ cm}^{-2} \end{cases}, \quad \text{and} \quad \begin{cases} \mu_n = 2700 \text{ cm}^2/\text{Vs} \\ n_n = 6.8 \times 10^{12} \text{ cm}^{-2} \end{cases}, \tag{3.20}$$

which manifests an adequate correspondence with the Shubnikov-de Haas oscillation analysis. The nucleation layer sheet density is higher than that at $T = 4.5$ K, contradict with previous T dependence of n_n. This is due to different cooldown histories experienced by YZ01. The cooldown in the ^{3}He cryostat does not freeze as many nucleation layer electrons as the one in the cryogen-free cryostat. All other non-trivial behaviours which did not follow the observed T-dependence in the Cryomech system could be ascribed to this different cooldown. In the bulk, E_F is 1.6 meV above E^b_C. In the triangular well, only E_1 is below E_F, thus the surface

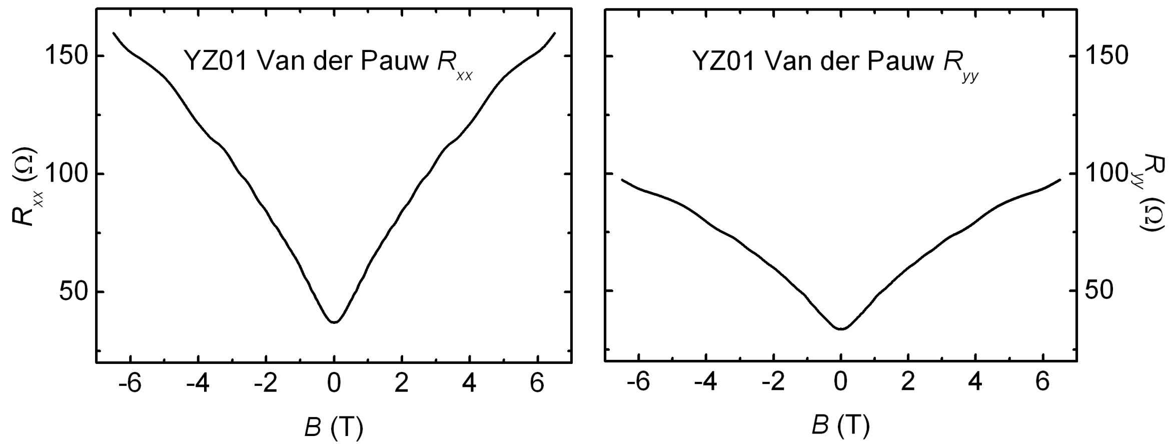

(a) Longitudinal MR of YZ01 Van der Pauw along $\hat{x}$.

(b) Longitudinal MR of YZ01 Van der Pauw along $\hat{y}$.

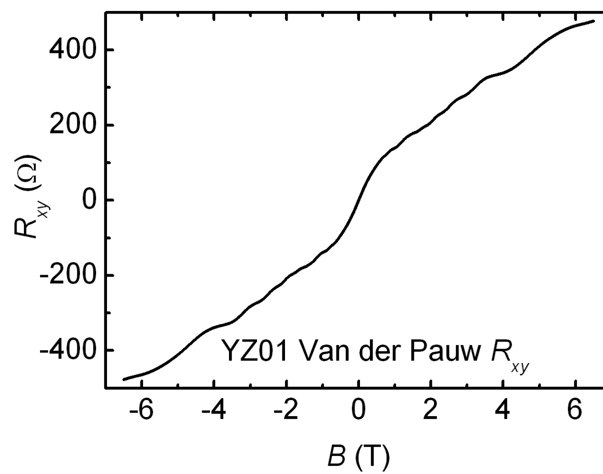

(c) Transverse MR of YZ01 Van der Pauw

Figure 3.30: YZ01 Van der Pauw magneto-transport measurements at $T = 1.2$ K

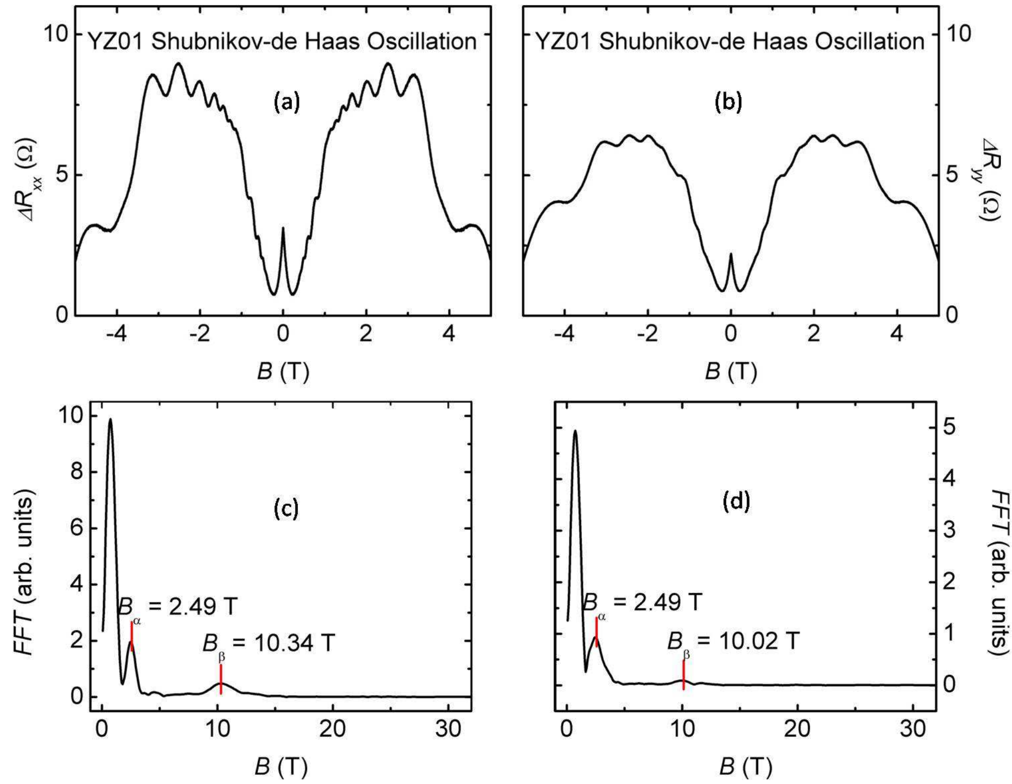

Figure 3.31: (Color online) Shubnikov-de Haas oscillations of (a) δR_{xx} and (b) δR_{yy} at $T = 1.2$ K, and linear backgrounds are subtracted to obtain better resolution. (c) and (d) Fast Fourier transforms (FFT) of the data in (a) and (b) respectively. The first peaks in (c) and (d) are both from background noise. The second and the third peaks are from the Shubnikov-de Haas oscillation.

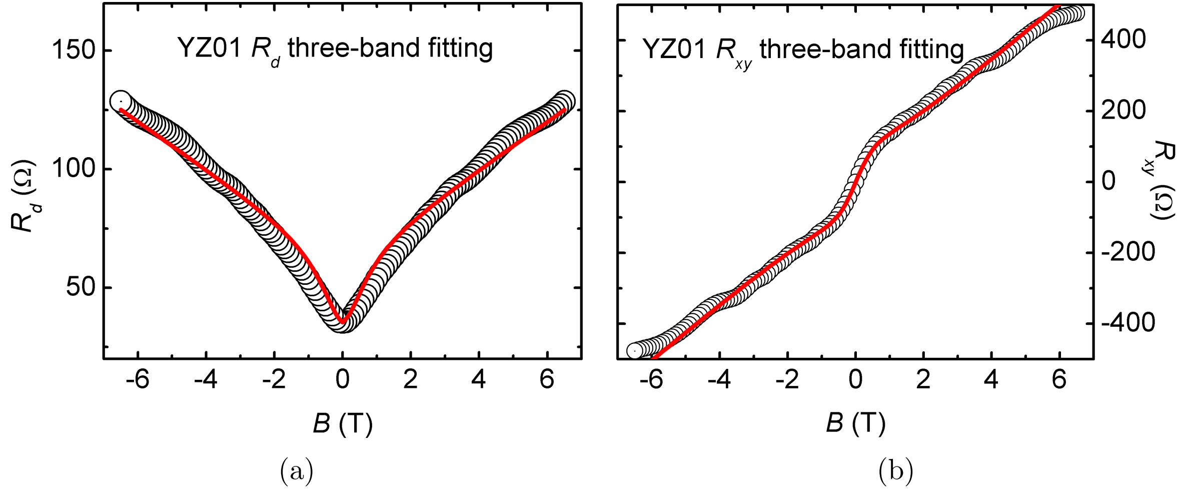

(a) (b)

Figure 3.32: (Color online) (a) R_d and (b) R_{xy} data of YZ01 Van der Pauw at $T = 1.2$ K. The circles are experimental values (For clarity, 1 out of 50 experimental points only are plotted). Red solid lines are fitted curves from the three-band fitting.

becomes a single subband system. E_1, E_2, and E_F are 60 meV, 108 meV, and 107 meV respectively above E_C^s, as shown in Fig. 3.33.

3.4.3 Moderately Doped n-type InAs

$T = 4.5$ K

Figure 3.34 also shows a weak oscillatory modulation of R_{xx} and R_{yy}. To reveal the oscillatory components of R_{xx} and R_{yy}, the parabolic backgrounds have to be subtracted [Figs. 3.35(a) and 3.35(b)]. A period of 0.18 T^{-1} in $1/B$ is obtained through the fast Fourier transforms in Figs. 3.27(c) and 3.27(d). The carrier 2D density and mobility are derived to be $\sim 0.27\times10^{12}$ cm^{-2} and ~ 20000 $\mathrm{cm}^2\mathrm{V}^{-1}\mathrm{s}^{-1}$. Compared with n_b and n_s at $T = 82$ K, the carrier 2D density is too low to be either of them. Nonetheless, these carriers have to correspond to one type of electrons with higher mobility, which are the bulk electrons. The ionization energy of the shallow donors is so small that a fair amount of donors are still ionized, contradict with the density derived from the Shubnikov-de Haas oscillation, which is only $\sim 10\%$ of the dopant concentration. This contradiction requires further studies.

From the three-band fitting [Figs. 3.36(a) and 3.36(b)], three sets of μ and n are extracted for every layer,

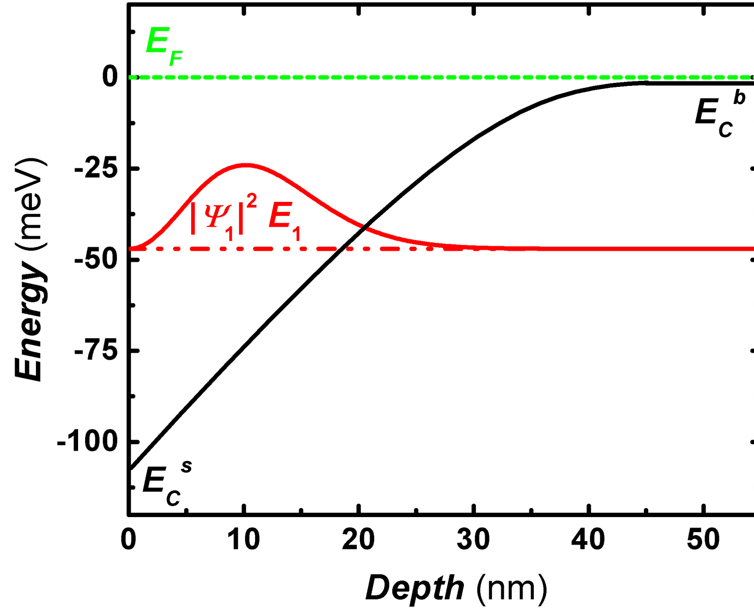

Figure 3.33: (Color online) At $T = 1.2$ K, schematic band structure at the surface of sample YZ01, where the 2DES has the first subband occupied [the energy levels are explained in the text, and $|\Psi_1|^2$ represents the probability density (in arbitrary units, with $|\Psi_1|^2 = 0$ taken at the E_1 line)].

$$\begin{cases} \mu_s = 7700\ \text{cm}^2/\text{Vs} \\ n_s = 2.5 \times 10^{12}\ \text{cm}^{-2} \end{cases}, \quad \begin{cases} \mu_b = 26000\ \text{cm}^2/\text{Vs} \\ n_b = 2.2 \times 10^{12}\ \text{cm}^{-2} \end{cases}, \quad \text{and} \quad \begin{cases} \mu_n = 2500\ \text{cm}^2/\text{Vs} \\ n_n = 5.9 \times 10^{12}\ \text{cm}^{-2} \end{cases}. \tag{3.21}$$

The Fermi level is derived to be 7.8 meV above E_b^C and 198 meV above E_s^C. Wih eigen energies 107 meV and 37 meV below E_F, the first two subbands are occupied in the surface potential well, and their densities are $n_{s1} = 1.91 \times 10^{12}$ cm^{-2} and $n_{s2} = 0.59 \times 10^{12}$ cm^{-2}. Figure. 3.37 shows the band structure and the electron wave functions.

T = 1.2 K

At $T = 1.2$ K and larger fields, a linear B background also appears in the transport measurements of YZ02 due to inhomogeneities (Figure 3.38). The Shubnikov-de Haas oscillations can be revealed after subtracting the background as shown in Figs. 3.39(a) and 3.39(b). Two different periods in $1/B$ $\Delta B_\alpha^{-1} = 0.51$ T^{-1} and $\Delta B_\beta^{-1} = 0.095$ T^{-1} are obtained from the fast Fourier transforms in Figs. 3.31(c) and 3.31(d). Each period suggests a carrier sheet density, which are $n_{2\text{D}}^\alpha = 0.095 \times 10^{12}$ cm^{-2} and $n_{2\text{D}}^\beta = 0.51 \times 10^{12}$ cm^{-2}.

The three-band fittings are shown in Fig. 3.40, a linear function of B is also added to the

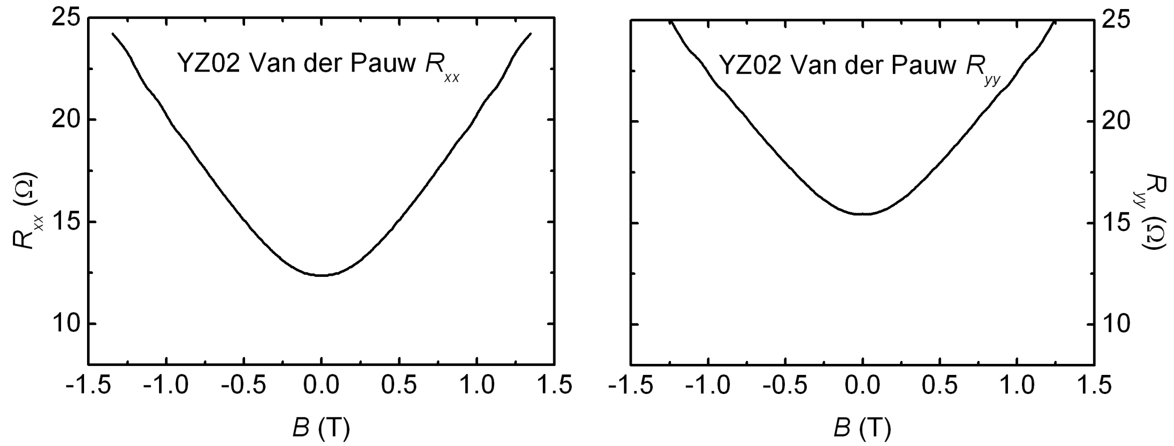

(a) Longitudinal MR of YZ02 Van der Pauw along $\hat{x}$.

(b) Longitudinal MR of YZ02 Van der Pauw along $\hat{y}$.

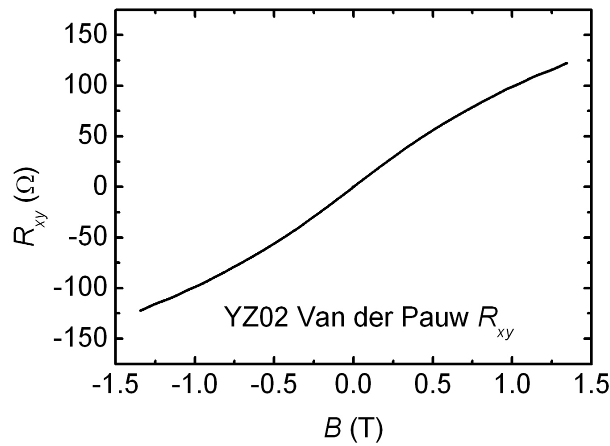

(c) Transverse MR of YZ02 Van der Pauw

Figure 3.34: YZ02 Van der Pauw magneto-transport measurements at $T = 4.5$ K

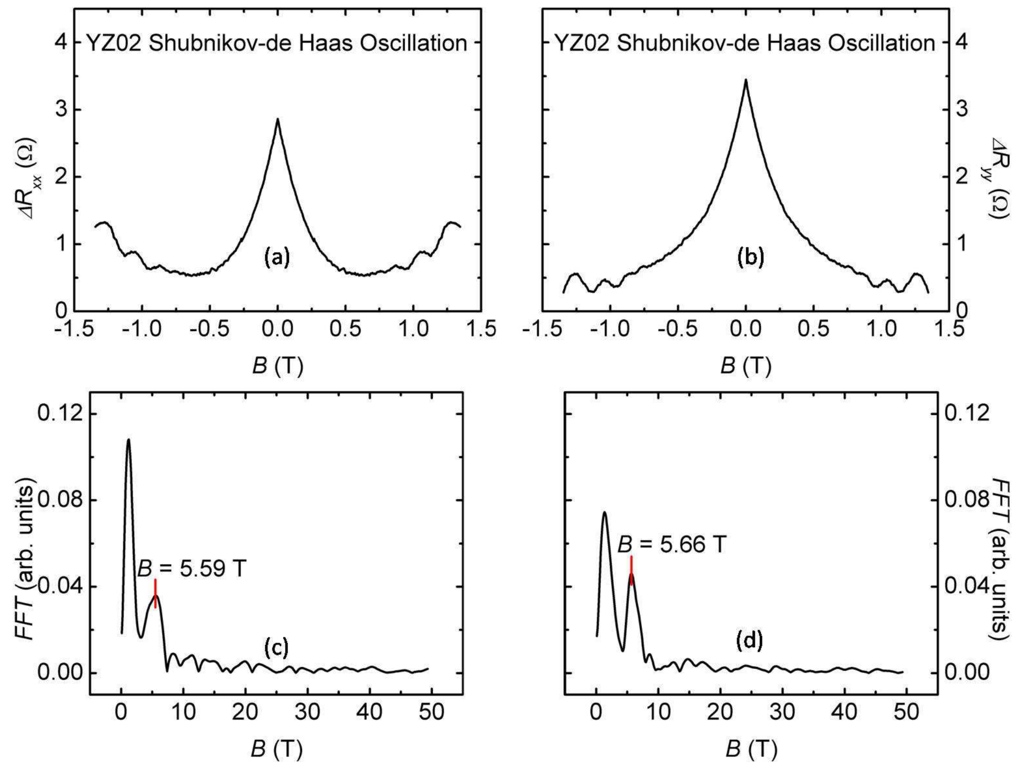

Figure 3.35: (Color online) Shubnikov-de Haas oscillations of (a) δR_{xx} and (b) δR_{yy} at $T = 4.5$ K, and parabolic backgrounds are subtracted to obtain better resolution. (c) and (d) Fast Fourier transforms (FFT) of the data in (a) and (b) respectively. The first peaks in (c) and (d) are both from background noise, and the second peaks are from the Shubnikov-de Haas oscillation, indicating a same frequency.

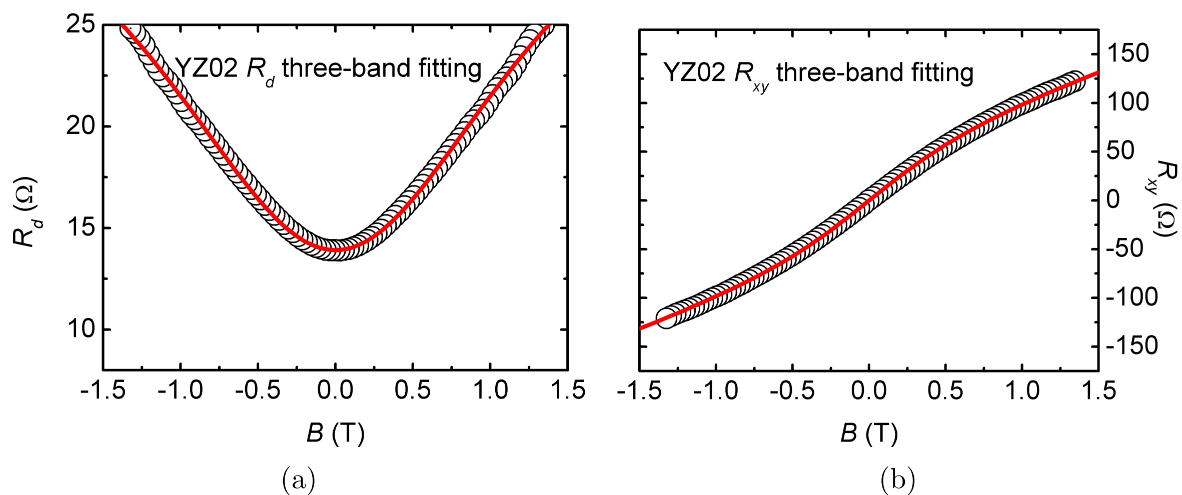

Figure 3.36: (Color online) (a) R_d and (b) R_{xy} data of YZ02 Van der Pauw at $T = 4.5$ K. The circles are experimental values (For clarity, 1 out of 16 experimental points only are plotted). Red solid lines are fitted curves from the three-band fitting.

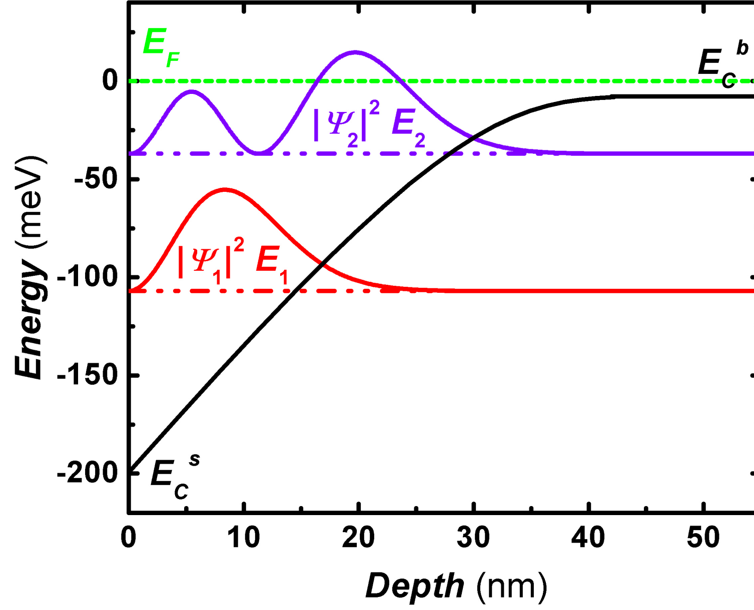

Figure 3.37: (Color online) At $T = 4.5$ K, schematic band structure at the surface of sample YZ02, where the 2DES has two occupied subbands [the energy levels are explained in the text, and $|\Psi_i|^2$ ($i = 1, 2$) represents the probability density (in arbitrary units, with $|\Psi_i|^2 = 0$ taken at the E_i line)].

fitting of R_d. The transport properties for each layer are

$$\begin{cases} \mu_s = 7400 \text{ cm}^2/\text{Vs} \\ n_s = 2.2 \times 10^{12} \text{ cm}^{-2} \end{cases}, \quad \begin{cases} \mu_b = 26000 \text{ cm}^2/\text{Vs} \\ n_b = 2.2 \times 10^{12} \text{ cm}^{-2} \end{cases}, \quad \text{and} \quad \begin{cases} \mu_n = 2500 \text{ cm}^2/\text{Vs} \\ n_n = 6.0 \times 10^{12} \text{ cm}^{-2} \end{cases}. \tag{3.22}$$

The Fermi level is calculated to be 7.8 meV and 230 meV above E_C^b and E_C^s respectively. At the surface, only the first subband is occupied. The band structure and the electron wave functions are shown in Fig. 3.41.

3.4.4 Heavily Doped n-type InAs

Figures 3.42 and 3.43 present the magneto-transport measurements and the three-band fitting of YZ03 at $T = 4.5$ K. However, Shubnikovde Haas oscillations are not observed in either R_{xx} or R_{yy}. YZ03 has the heaviest doping, which may affect the quality of the films, thereby no oscillations can be detected. Equation 3.23 exhibits the carrier mobilities and densities as

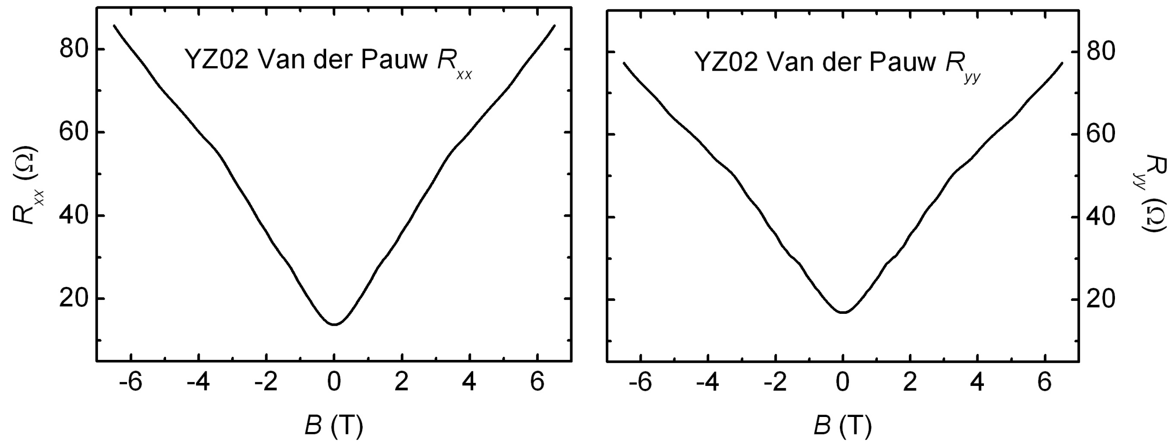

(a) Longitudinal MR of YZ02 Van der Pauw along $\hat{x}$.

(b) Longitudinal MR of YZ02 Van der Pauw along $\hat{y}$.

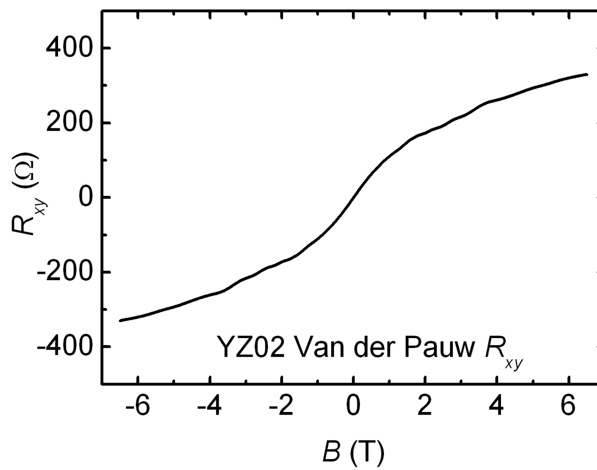

(c) Transverse MR of YZ02 Van der Pauw

Figure 3.38: YZ01 Van der Pauw magneto-transport measurements at $T = 1.2$ K

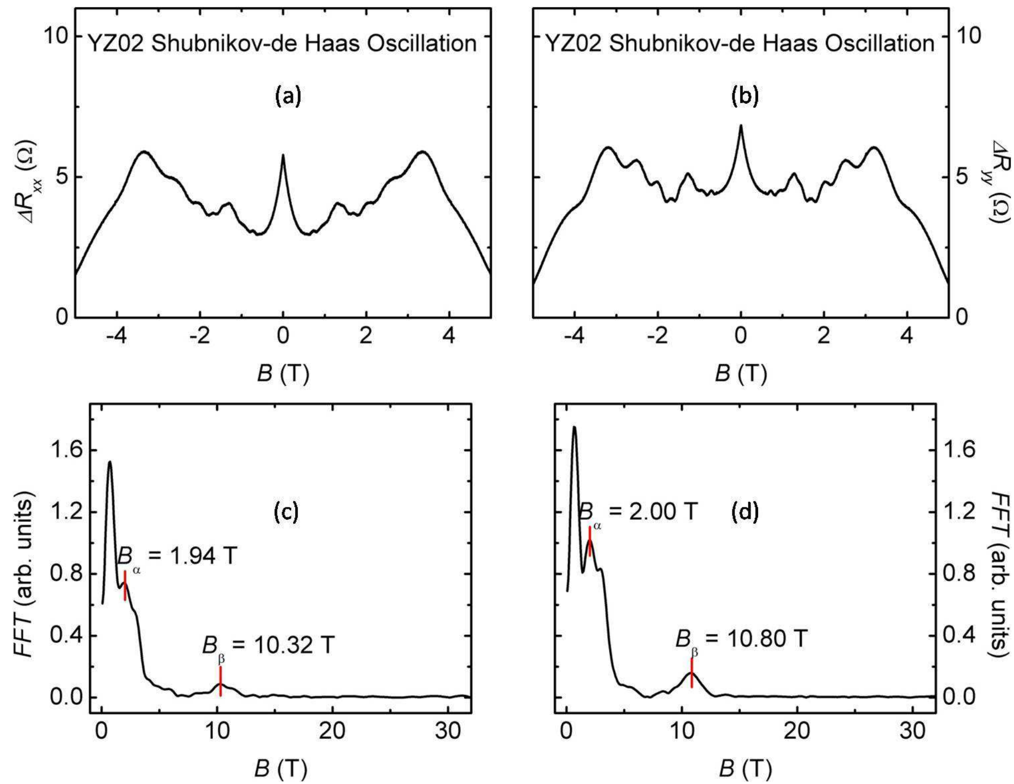

Figure 3.39: (Color online) Shubnikov-de Haas oscillations of (a) δR_{xx} and (b) δR_{yy} at $T = 1.2$ K, and linear backgrounds are subtracted to obtain better resolution. (c) and (d) Fast Fourier transforms (FFT) of the data in (a) and (b) respectively. The first peaks in (c) and (d) are both from background noise. The second and the third peaks are from the Shubnikov-de Haas oscillation.

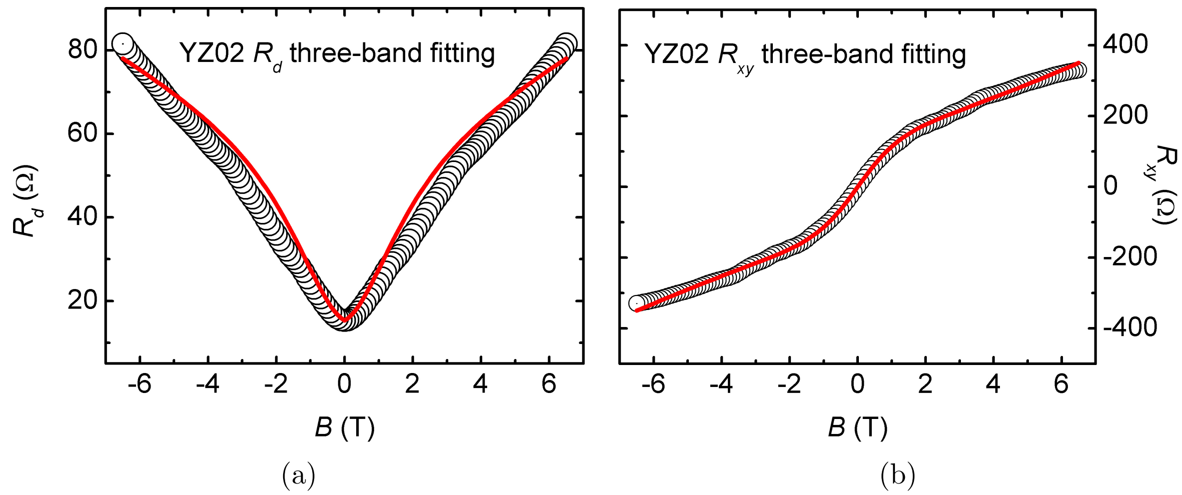

Figure 3.40: (Color online) (a) R_d and (b) R_{xy} data of YZ02 Van der Pauw at $T = 1.2$ K. The circles are experimental values (For clarity, 1 out of 50 experimental points only are plotted). Red solid lines are fitted curves from the three-band fitting.

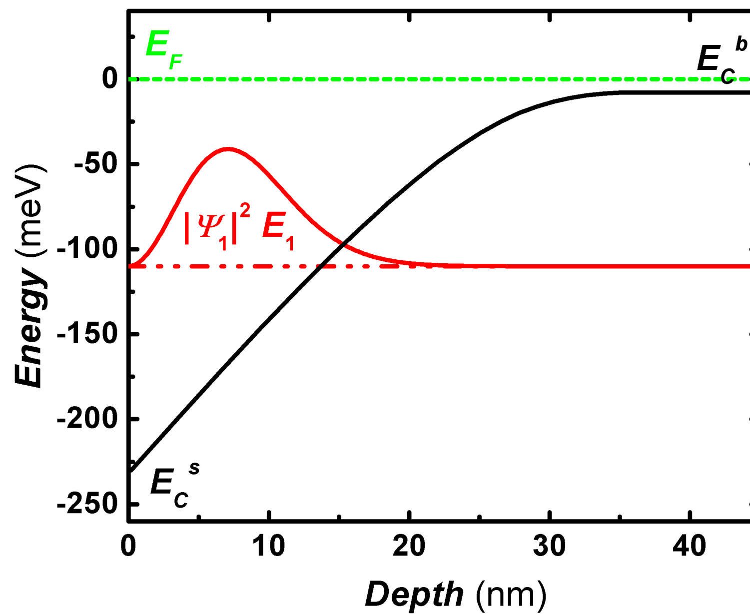

Figure 3.41: (Color online) At $T = 1.2$ K, schematic band structure at the surface of sample YZ02, where the 2DES has the first subband occupied [the energy levels are explained in the text, and $|\Psi_1|^2$ represents the probability density (in arbitrary units, with $|\Psi_1|^2 = 0$ taken at the E_1 line)].

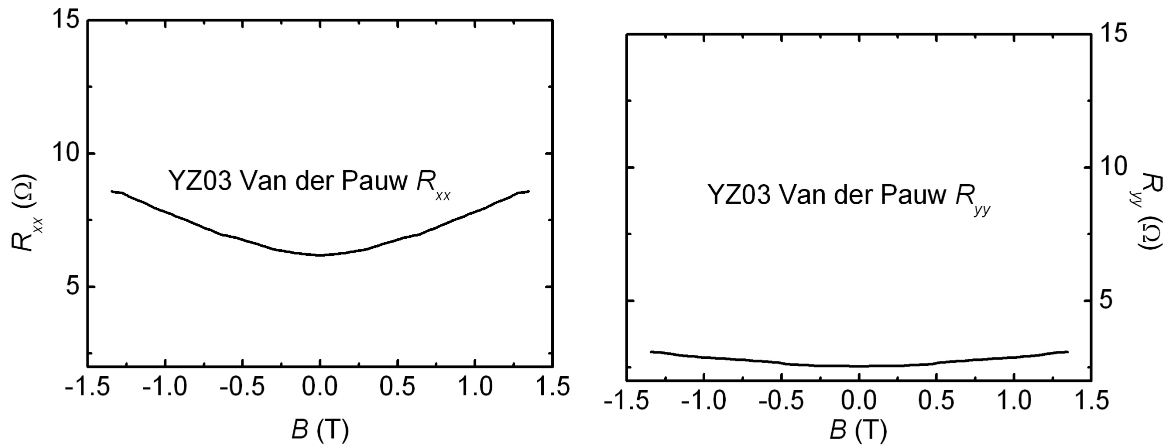

(a) Longitudinal MR of YZ03 Van der Pauw along $\hat{x}$.

(b) Longitudinal MR of YZ03 Van der Pauw along $\hat{y}$.

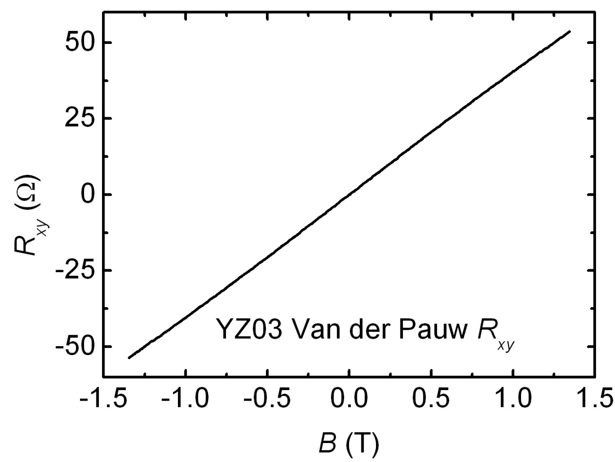

(c) Transverse MR of YZ03 Van der Pauw

Figure 3.42: YZ03 Van der Pauw magneto-transport measurements at $T = 4.5$ K

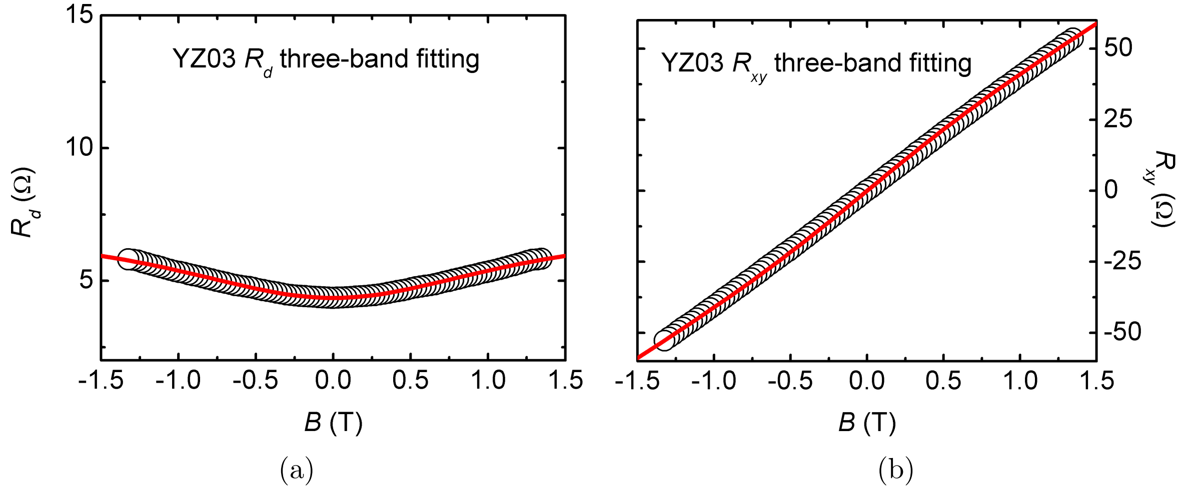

Figure 3.43: (Color online) (a) R_d and (b) R_{xy} data of YZ03 Van der Pauw at $T = 4.5$ K. The circles are experimental values (For clarity, 1 out of 16 experimental points only are plotted). Red solid lines are fitted curves from the three-band fitting.

$$\begin{cases} \mu_s = 3800 \text{ cm}^2/\text{Vs} \\ n_s = 2.1 \times 10^{12} \text{ cm}^{-2} \end{cases}, \quad \begin{cases} \mu_b = 25000 \text{ cm}^2/\text{Vs} \\ n_b = 12.1 \times 10^{12} \text{ cm}^{-2} \end{cases}, \quad \text{and} \quad \begin{cases} \mu_n = 2200 \text{ cm}^2/\text{Vs} \\ n_n = 5.9 \times 10^{12} \text{ cm}^{-2} \end{cases}. \tag{3.23}$$

YZ03 is highly degenerated, and behaves more metallic. Its carriers in each layer barely freeze. The unvaried n_b forced E_F rising up to 22.5 meV above E_C^b. The energy levels inside the surface potential well are same as the ones at $T = 80$ K, as reflected in Fig. 3.44. Since no Shubnikovde Haas oscillations exist in YZ03 at low temperatures, the magneto-transport measurements were not performed at $T = 1.2$ K and larger fields.

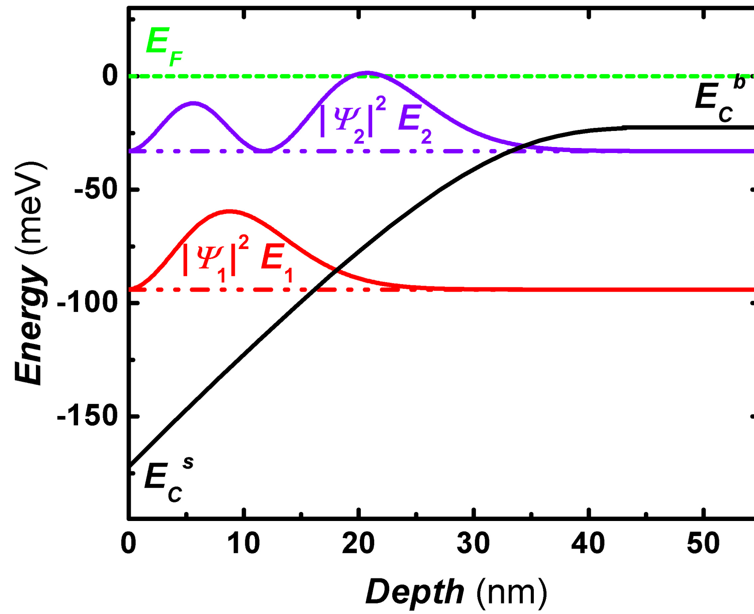

Figure 3.44: (Color online) At $T = 4.5$ K, schematic band structure at the surface of sample YZ03, where the 2DES has two occupied subbands [the energy levels are explained in the text, and $|\Psi_i|^2$ ($i = 1$, 2) represents the probability density (in arbitrary units, with $|\Psi_i|^2 = 0$ taken at the E_i line).

Chapter 4

p-type InAs

4.1 Room Temperature Band Structure

4.1.1 Surface Inversion Layer

Most of the previous research works of InAs have been done on n-type samples, while p-type ones still lack of investigations. Different from n-type InAs, the accumulation layer at the surface is replaced by an inversion layer, which is separated from the holes in the bulk by a depletion layer. Ideally, the magneto-transport measurements on the 2DES at the p-type InAs surface can be isolated from the bulk. As depicted in Fig. 4.1, an inversion layer confined within a triangular potential exists at the surface of YZ04. A detailed transport characterization and a surface band structure analysis on p-type InAs can help further improve the semiconductor transistor performances.

4.1.2 Two-band Fitting

Comparing R_{xx} and R_{yy} of YZ04 in Fig. 4.2, the p-type InAs also demonstrates an inhomogeneity. Both R_{xx} and R_{yy} are B independent, and R_{xy} shows a linear dependence on B, indicating the presence of one type of majorities. The sign of the Hall slope in Fig. 4.2 (c) is opposite from the ones of the n-type InAs samples, consistent with the holes in the bulk. In contrast, there are still electrons at the surface and the nucleation layer of YZ04 respectively due to E_F pinned above E_C^s and the UID donors. Compared with holes in the bulk, because of either small density (the surface inversion layer) or low mobility (the nucleation layer), their conductivities are at least one order of magnitude smaller. Therefore, YZ04 behaves as a hole-dominant mono-band system.

When the scale of R_d is sufficiently shrunk compared with the n-type InAs, a slight parabolic

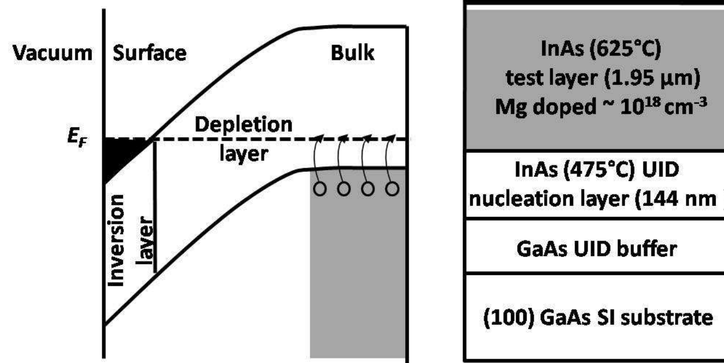

Figure 4.1: Left panel: Schematic band structure at the surface of p-type InAs. E_F is above the surface conduction minimum and close to the bulk valence band maximum. The shaded area is the inversion layer, while the holes stay in the bulk and are separated from the surface electrons by a depletion layer. Right panel: Schematic of the InAs/GaAs heterostructure with surface electron inversion layer (Black) and the bulk hole test layer (shaded).

background can be still observed [Fig. 4.3 (a)] at room temperature. Two conducting layers are thus assumed to exist in YZ04, with one being the surface inversion layer and the other being the bulk layer. And their transport properties are derived from a two-band fitting on R_d and R_{xy},

$$\begin{cases} \mu_s = 700 \text{ cm}^2/\text{Vs} \\ n_s = 3.1 \times 10^{12} \text{ cm}^{-2} \end{cases}, \quad \text{and} \quad \begin{cases} \nu = 310 \text{ cm}^2/\text{Vs} \\ p = 48 \times 10^{12} \text{ cm}^{-2} \end{cases}, \tag{4.1}$$

where ν and p are hole mobility and sheet density. Figure 4.3 manifests a sufficient correspondence between data and the two-band theoretical fit. Obviously, the holes in the bulk are dominant in the conductivity as expected. The relatively low hole mobilities are consistent with previous studies [24].

4.1.3 Surface Band Structure

The 3D hole density in the bulk can be calculated to be $p_{3\text{D}} = 2.7 \times 10^{17}$ cm^{-3}, in a magnificent agreement with Mg doping concentration of 2.78×10^{17} cm^{-3}. For shallow acceptors in InAs, their average ionization energy is ~ 15 meV, thus the thermal energy at room temperature is adequate to ionize all of them. To calculate E_F in a hole system, Equation 3.9 has to be modified as

$$p_{b3\text{D}} = \int_{-\infty}^{E_V^b} \frac{m_h^* \sqrt{2m_h^*(E_V^b - E)}}{\pi^2 \hbar^3} \frac{1}{e^{\frac{E_F - E}{kT}} + 1} \left[1 - \frac{2(E_V^b - E)}{E_g}\right] \sqrt{1 - \frac{E_V^b - E}{E_g}} dE, \tag{4.2}$$

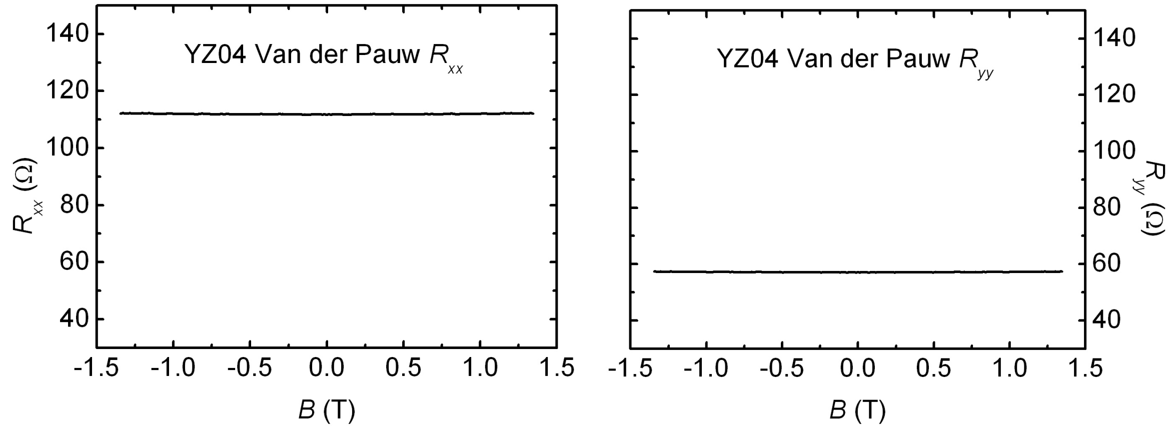

(a) Longitudinal MR of YZ04 Van der Pauw along $\hat{x}$.

(b) Longitudinal MR of YZ04 Van der Pauw along $\hat{y}$.

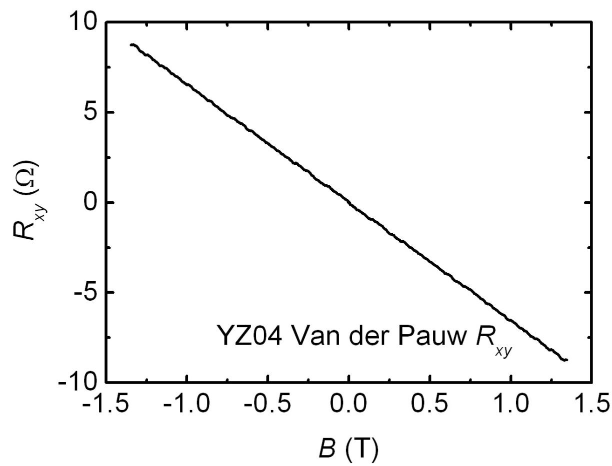

(c) Transverse MR of YZ04 Van der Pauw

Figure 4.2: YZ04 Van der Pauw magneto-transport measurements at T = 300 K

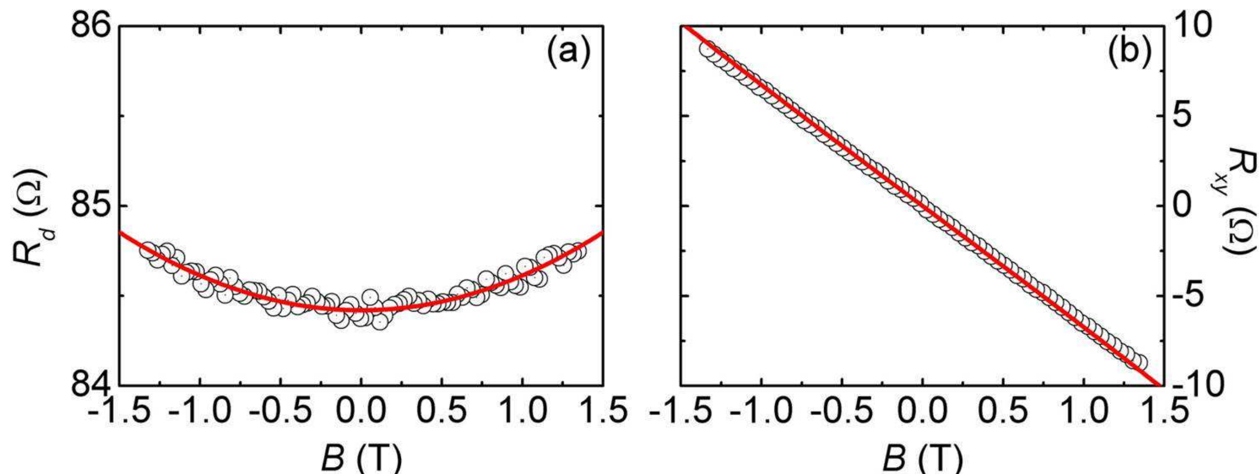

Figure 4.3: (Color online) (a) R_d and (b) R_{xy} data of YZ04 Van der Pauw at T = 300 K. The circles are experimental values (For clarity, 1 out of 16 experimental points only are plotted). Red solid lines are fitted curves from the two-band fitting.

with E_V^b being the valence band maximum. Considering the Γ-point hole effective mass is $m_h^* = 0.40m_e$, E_F is calculated to be 88 meV above E_V^b through Eq. 4.2. The quantization of the inversion layer subbands can be treated the same as the accumulation layer. The first two subbands in the triangular well are occupied with their eigen energies E_1 = 88 meV and E_2 = 155 meV above E_C^s. Each subband has its own electron density $n_{s1} = 2.19 \times 10^{12}$ cm^{-2} and $n_{s2} = 0.91 \times 10^{12}$ cm^{-2}, besides, the approximate width of the triangular well ~ 30 nm, and $F = 5.9 \times 10^4$ V/cm. In our highly mismatched p-type InAs, large neutral clusters of impurities and defects could exist, which distort the current flow lines and reduce the mobility [24]. These T-independent defects scattering plus the phonon scattering together determineμ_s. Figure 4.4 illustrates the band structure of YZ04 and the probability density associated with the surface electron wave functions at room temperature.

4.2 Liquid Helium Temperature Band Structure

4.2.1 T = 8.2 K

Antilocalization

In a disordered metal-like system, except the classical Drude multi-carrier correction to the MR, a quantum correction to the conductivity of the surface 2D electrons $\sigma_2(B)$ can be also observed, which is the antilocalization (AL) signal near zero fields. In a closed transport path scattered by impurities, an electron has a finite probability of returning to the incident point via an identical path in the clockwise and counterclockwise directions, as schematically shown

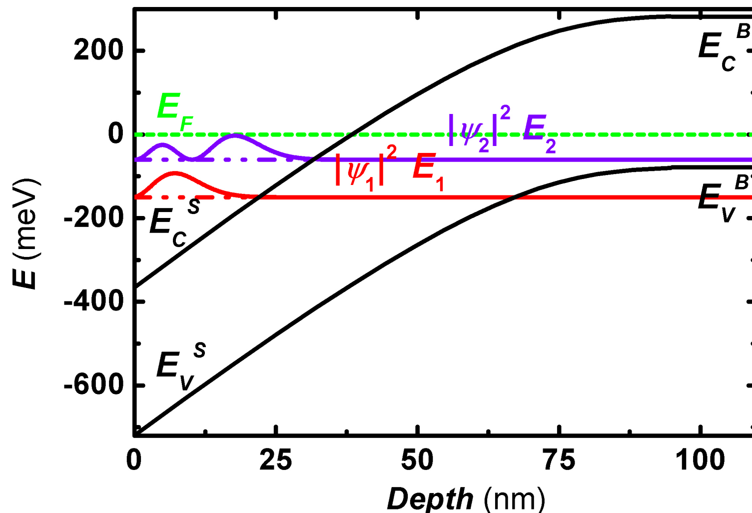

Figure 4.4: (Color online) Room temperature schematic band structure at the surface of sample YZ04, where the 2DES has two occupied subbands [the energy levels are explained in the text, and $|\Psi_i|^2$ ($i = 1, 2$) represents the probability density (in arbitrary units, with $|\Psi_i|^2 = 0$ taken at the E_i line)].

in Fig. 4.5. In weak spin-orbit interaction (SOI) materials, the constructive interference at the incident point contributes to an increase of resistance known as weak localization (WL). In strong SOI materials such as InAs, the destructive interference occurs due to spin rotation over the paths, which contributes an extra phase shift of π. This gives a decrease in resistance, known as AL. With an external magnetic field, the phase coherence will be broken, as a result, negative and positive MR occur in WL and AL respectively. Low temperature AL magneto-transport measurements are sensitive to electron interferences, and thus can be used as a probe of quantum states [25, 26, 27, 28, 29]. The spin-dependent interactions between controllable surface magnetism and itinerant electrons in a non-magnetic host provide insight for spin-based technologies, magnetic data storage and quantum information processing.

The InAs epitaxial layer has prominent Rashba SOI due to structural inversion asymmetry, and hence shows AL, which contains a characteristic MR determined by the elastic relaxation time τ_0 (independently determined by carrier mobility and density), the phase decoherence time τ_ϕ, and the spin-orbit decoherence time τ_{SO}. In confined structures, such as films and wires, WL and AL are more prominent due to larger possibilities of time reversed trajectories. Because WL and AL are interference effects, they have a unique dependence on the external magnetic field. The MR measurement is a useful method to extract the quantitative information of spin and phase scattering of the electrons. Figure 4.6 presents a schematic MR curve showing AL. The separation of the resistance maxima in B is affected by τ_{SO}. As the separation gets wider, τ_{SO} decreases, indicating an increase in SOI. The depth of the resistance minimum depends on the ratio τ_ϕ/τ_{SO}.

The quantum corrections to the two-dimensional conductivity $\sigma_2(B)$ arising from AL are

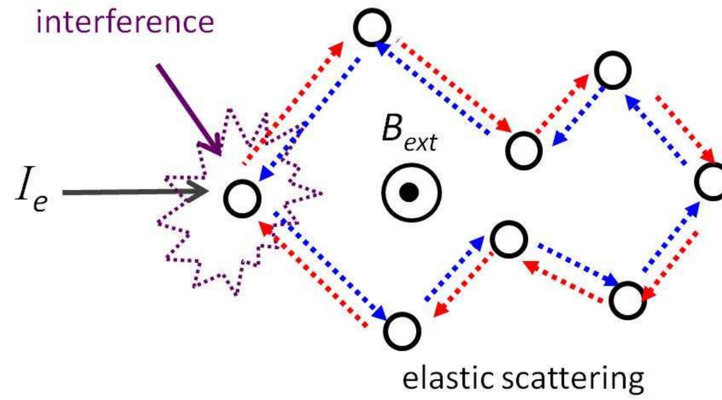

Figure 4.5: Quantum interference of time reversed paths of an electron with a perpendicular B.

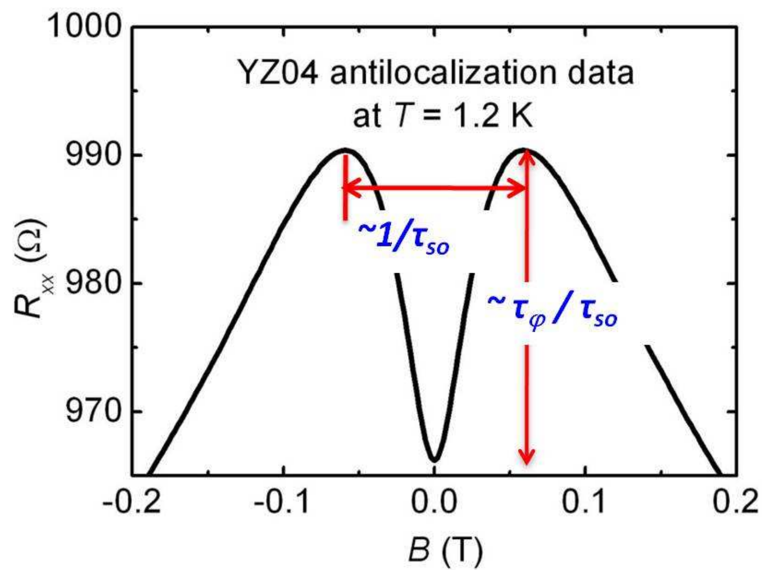

Figure 4.6: Characteristic shape of the AL measurement. Curve shape sensitive to phase coherence time τ_ϕ and spin-orbit scattering time τ_{SO}.

sensitive to τ_i and τ_{SO}. To properly express the interactions in our studies, an expression for $\Delta\sigma_2(B) = \sigma_2(B) - \sigma_2(B = 0)$ was adapted by using the HLN model [30, 31]

$$\Delta\sigma_2(B) = \frac{e^2}{2\pi^2\hbar}\Bigg\{-\Bigg[\psi(\frac{1}{2}+\frac{B_0}{|B|}) - \psi(\frac{1}{2}+\frac{B_\phi + B_{SO}}{|B|}) + \frac{1}{2}\psi(\frac{1}{2}+\frac{B_\phi}{|B|}) - \frac{1}{2}\psi(\frac{1}{2}+\frac{B_\phi + 2B_{SO}}{|B|})\Bigg] + \Bigg[ln(\frac{B_0}{|B|}) - ln(\frac{B_\phi + B_{SO}}{|B|}) + \frac{1}{2}ln(\frac{B_\phi}{|B|}) - \frac{1}{2}ln\left(\frac{B_\phi + 2B_{SO}}{|B|}\right)\Bigg]\Bigg\} \quad (4.3)$$

where $\psi(x)$ is the digamma function and each scattering time τ_α (with $\alpha = 0, \phi, SO$) corresponds to a characteristic magnetic field $B_\alpha = \hbar/(4eD\tau_\alpha)$, with D being the 2D diffusion constant, together with τ_0 can be determined from carrier density and mobility independently.

Three-band Fitting

When the sample is cooled down to $T = 8.2$ K, the shape of MR and the Hall data (Fig. 4.7) varied significantly from room temperature. In Fig. 4.7(a), the abrupt negative MR originates from the WL. Near zero fields, the crossing over to positive MR of the signal indicates the presence of the AL. The Hall slope in Fig. 4.7 (c) possesses a different sign from Fig.4.2 (c), which implies the electrons become the majorities. Most of the holes in the bulk are frozen out in our p-type InAs, and the ionized impurity scatterings are supposed to be reduced dramatically. Due to the reduction of holes, other types of carriers can be detected in the magneto-transport measurements at low temperatures. Both the bulk and the nucleation layers are unintentionally doped with H, C, and O at a level of $\sim 10^{16}$ cm^{-3} during the growth, which could cause a considerable amount of free electrons. Thus the residue holes plus the electrons form the bulk carriers. Including the electrons from the surface and the nucleation layers, this is a three-band system with

$$\begin{cases} \mu_s = 500 \text{ cm}^2/\text{Vs} \\ n_s = 3.1 \times 10^{12} \text{ cm}^{-2} \end{cases}, \quad \begin{cases} \nu = 19000 \text{ cm}^2/\text{Vs} \\ p = 0.0021 \times 10^{12} \text{ cm}^{-2} \end{cases}, \quad \text{and} \quad \begin{cases} \mu_n = 26 \text{ cm}^2/\text{Vs} \\ n_n = 36 \times 10^{12} \text{ cm}^{-2} \end{cases}. \quad (4.4)$$

Figure 4.8(a) has the MR data cut at 1.4 T due to the experiment limits, however, the background plot from the three-band analysis manifests a tendency to merge with the experiment data at larger fields, together with the Hall signal fitting in Fig. 4.8(b) support the three-band fitting. In Eq. 4.4, the bulk carrier is a result of compensation between the UID donor electrons and the residue holes. From the fitting, the transport property of the bulk is more hole-like, and the considerably large mobility is caused by the small carrier density due to compensation. n_s is not changed compared with room temperature. This is expected, because the distance between E_F and E_C^s is approximately T-independent, as well as F.

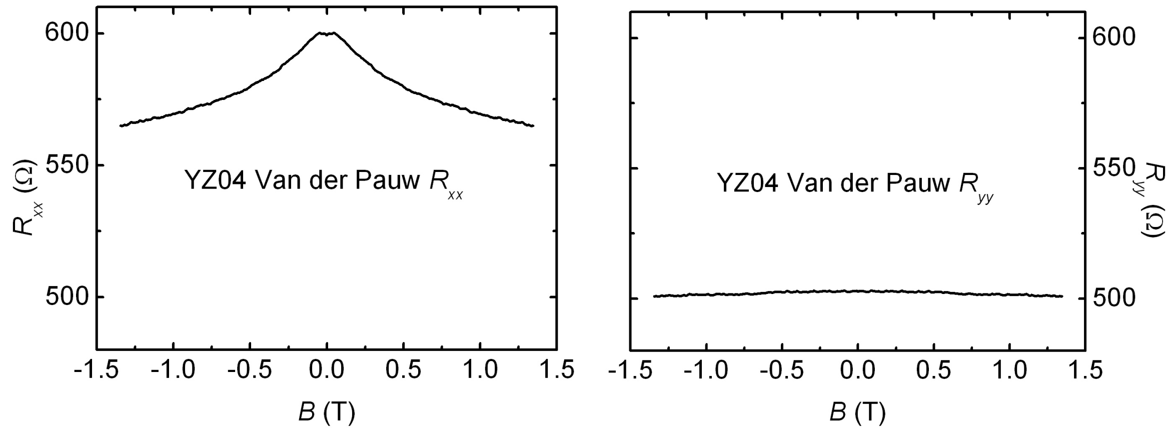

(a) Longitudinal MR of YZ04 Van der Pauw along $\hat{x}$.

(b) Longitudinal MR of YZ04 Van der Pauw along $\hat{y}$.

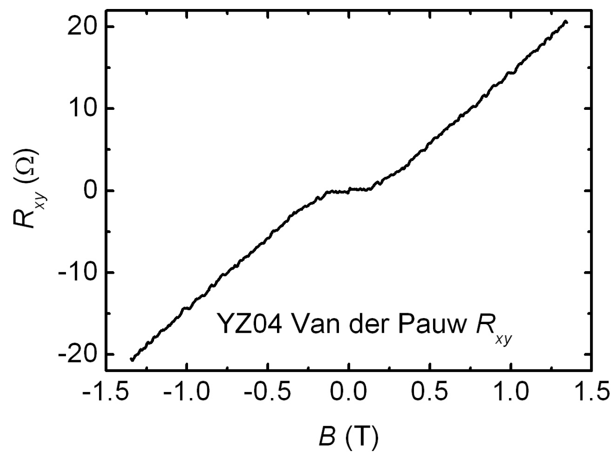

(c) Transverse MR of YZ04 Van der Pauw

Figure 4.7: YZ04 Van der Pauw magneto-transport measurements at $T = 8.2$ K

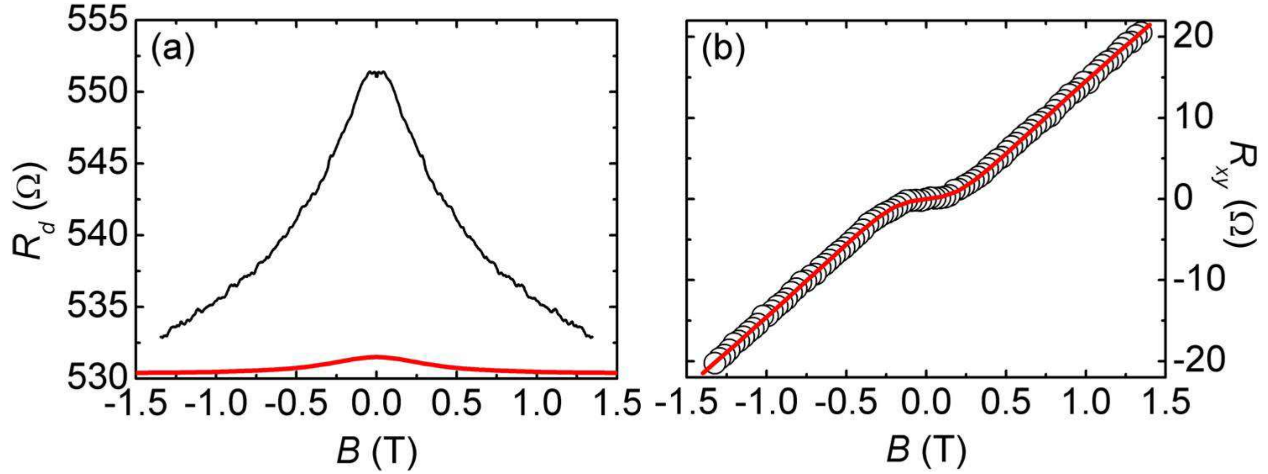

Figure 4.8: (Color online) (a) R_d and (b) R_{xy} data of YZ04 Van der Pauw at T = 8.2 K. The circles are experimental values (For clarity, 1 out of 16 experimental points only are plotted). Red solid lines are fitted curves from the three-band fitting.

Therefore, two surface subbands are presumed to be occupied as well. The improved μ_s is due to the reduction of both Coulomb and phonon scattering. The surface band structure can not be plotted due to the uncertainty of the hole density in the bulk.

The AL signal in Fig. 4.7 is attributed to the surface accumulation layer. In Fig. 4.9(a) MR is presented as $\Delta R_d(B) = R_d(B) - R_d(B = 0)$ normalized to $R_{d0} = R_d(B = 0)$. Since $\Delta R_d(B) \ll R_{d0}$ we linearize to $\Delta\sigma_2(B)/\sigma_2(B = 0) \approx -\Delta R_d(B)/R_{d0}$ which allows direct comparison to experimental $R_d(B)$ values. Experimentally, our data follow Eq. (4.3) to good precision. The AL fitting in Fig. 4.9(a) plus the background in Fig. 4.8(a) provide a reasonable fitting of $R_d(B)$ as illustrated in Fig. 4.9(b).

The determined relaxation times are τ_0 = 0.011 ps, τ_ϕ = 1.8 ps, and τ_{SO} = 1.7 ps. With D = 64 cm^2/Vs, the diffusive coherence lengths are calculated according to $L_\alpha = \sqrt{D\tau_\alpha}$: the ballistic coherence length L_0 = 12 nm, the phase coherence length L_ϕ = 110 nm, and the spin-orbit coherence length L_{SO} = 100 nm.

4.2.2 T = 1.2 K

Three-band Fitting

To further eliminate the contribution to the conductivity from the residue holes and the UID donor electrons, the sample is cooled down to T = 1.2 K in the ^{3}He cryostat system, where large fields can be applied up to B = 10 T. Figure 4.10 shows the MR and Hall measurements of YZ04 at T = 1.2 K, with a significant AL signal observed. Two sets of carrier density and mobility are obtained from the two-band analysis, and we assign them

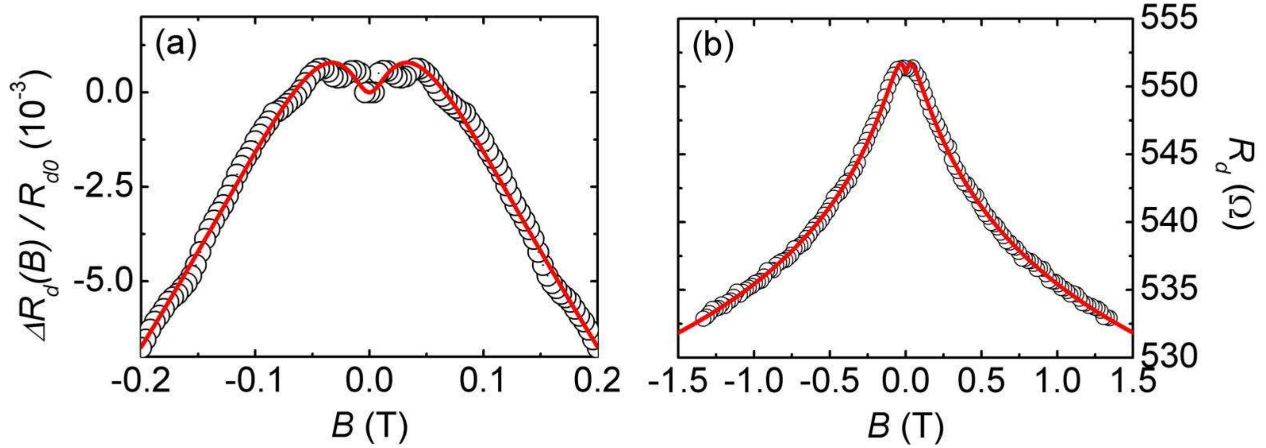

Figure 4.9: (Color online) (a) Magnetoresistance due to AL within a small range of B at 8.2 K. (b) R_d data with AL fitting at 8.2 K. The circles are experimental values (For clarity, 1 out of 2 and 1 out of 20 experimental points only are plotted in (a) and (b) respectively). Red solid lines are fitted curves from Eq. 4.3.

to the two surface subbands electrons: $n_{s1} = 2.2 \times 10^{12}$ cm^{-2} and $\mu_{s1} = 360$ cm^2/Vs; $n_{s2} = 1.0 \times 10^{12}$ cm^{-2} and $\mu_{s2} = 730$ cm^2/Vs. The good correspondence between two-band fitting and the experiment data in Fig. 4.11 assures the validity of the two-band fitting. The sum of the two surface subbands electron densities matches with the previously calculated n_s at higher temperatures. In the triangular well model, with $n_s = 3.2{\times}10^{12}$ cm^{-2}, the first two subbands are populated with electron densities of $n_{s1} = 2.28 \times 10^{12}$ cm^{-2} and $n_{s2} = 0.92 \times 10^{12}$ cm^{-2}, consistent with the two-band fitting. The electron mobilities of the two subbands are rather enhanced, which is still attributed to the reduction of both Coulomb and phonon scattering. When ionized impurity scatterings are predominant, the electron wave functions are sensitive to them, and thus lead to different electron mobilities of the two surface subbands. their The fairly straight Hall signal in Fig. 4.11(b) suggests the freeze-out of the nucleation layer. Nonetheless, there is a slight slope change near zero fields, which denotes a tiny amount of ionized acceptors and UID donors being left in the bulk.

Antilocalization analysis

A more prominent AL signal can be observed at this temperature, as demonstrated in Fig. 4.12. From the total density and the effective mobility of the surface electrons, we derive $\tau_0 = 0.056$ ps and $D = 310$ cm^2/Vs through non-parabolicity calculation. The two surface subbands electrons are treated together to fit the data with Eq. 4.3. The determined relaxation times are $\tau_\phi = 2.6$ ps, and $\tau_{SO} = 0.64$ ps. The spin-orbit decoherence time decreases while the elastic relaxation time increases, implies the system is dominated by the Dyakonov-perel mechanism [32] $< \Delta E_C^2 >= \dfrac{4\hbar^2}{\tau_{SO}\tau_\phi}$, where $< E_C^2 >$ is the Fermi surface

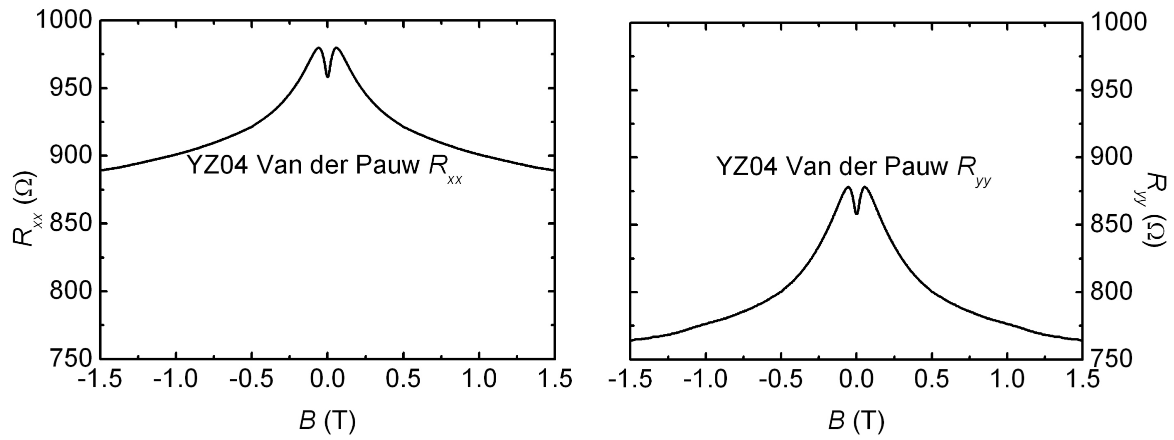

(a) Longitudinal MR of YZ04 Van der Pauw along $\hat{x}$.

(b) Longitudinal MR of YZ04 Van der Pauw along $\hat{y}$.

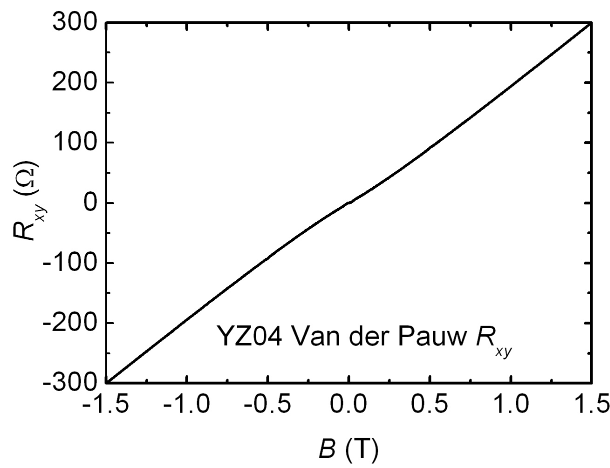

(c) Transverse MR of YZ04 Van der Pauw

Figure 4.10: YZ04 Van der Pauw magneto-transport measurements at $T = 1.2$ K

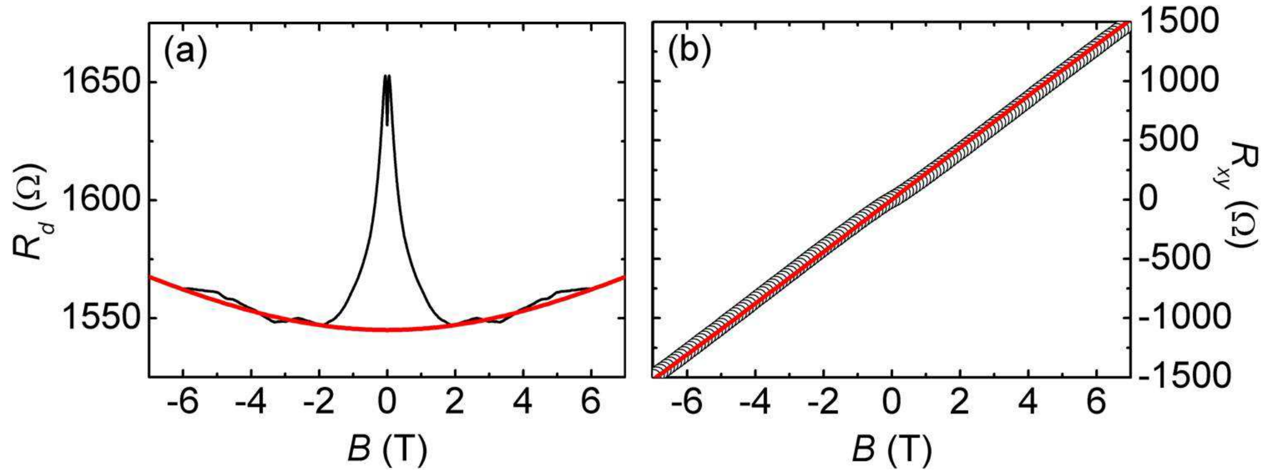

Figure 4.11: (Color online) (a) R_d and (b) R_{xy} data of YZ04 at 1.2 K. The black line and the circles are experimental values [For clarity, in (b) 1 out of 50 experimental points only are plotted]. Red solid lines are fitted curves from the two-band analysis, which in (a) leads to a parabolic background in MR.

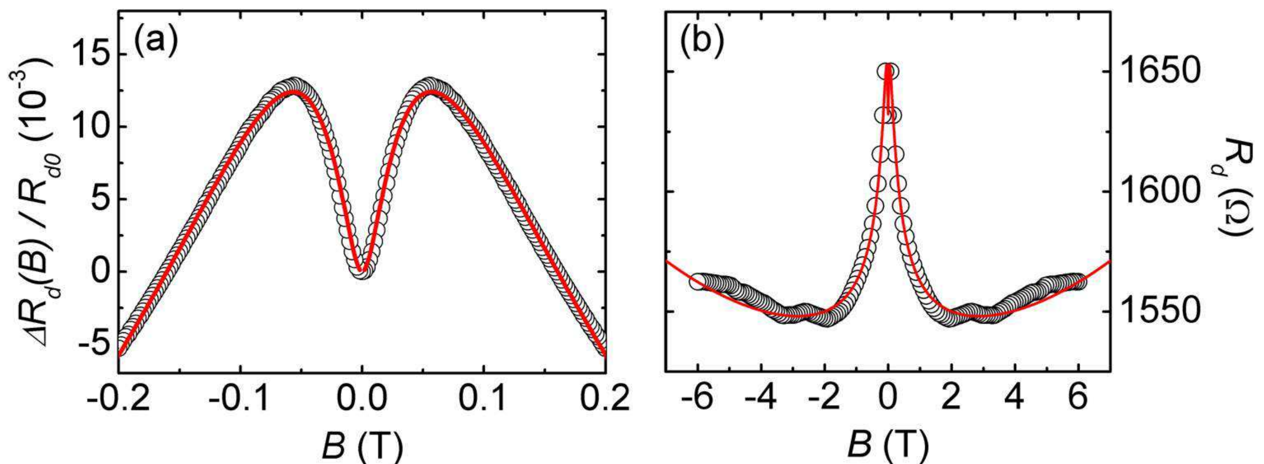

Figure 4.12: (Color online) (a) Magnetoresistance due to AL within a small range of B at 1.2 K. (b) R_d data with AL fitting at 1.2 K. The circles are experimental values (For clarity, 1 out of 2 and 1 out of 40 experimental points only are plotted in (a) and (b) respectively). Red solid lines are fitted curves from Eq. 4.3.

average variance of the spin-split of the conduction band ΔE_C. Using the approximation $\Delta E_C = \sqrt{< \Delta E_C^2 >}$ and the equation $\Delta E_C = 2\alpha k_F$ with α and k_F being Rashba spin-orbit constant and Fermi wave vector respectively, the Rashba parameter can be determined as 1.1×10^{-12} eVm. The inter-band scattering also exists between the two surface subbands. However, how does this scattering mechanism contribute to the phase and spin-orbit decoherence requires further studies. The diffusive coherence lengths are calculated as $L_0 = 42$ nm, $L_\phi = 280$ nm, and $L_{SO} = 140$ nm.

Chapter 5

Discussion

5.1 n-type InAs

The nucleation layer, the bulk layer, and the surface accumulation layer form a three-band structure in our n-type InAs semiconductors. Typically, the parallel conductivity from the surface and the bulk are observed in magneto-transport measurements of n-type InAs. In our experiments, the nucleation layer also contributes to the flim conductivity. Especially for the InAs with lower doping concentration, the conductivity from the nucleation layer can not be eliminated. The nucleation layer is a couple hunderds nm thick InAs layer between the InAs test layer and the GaAs substrate. It is grown at a relatively low temperature and unintentionally doped (UID) with C, H, and O. The growth condition is kept consistent for n-type InAs with any doping levels. The measurements indicate an electron density of $\sim 5 \times 10^{17}$ cm^{-3} and a mobility of $\sim$ 2000 cm^2/Vs for nucleation layers of n-type InAs films with different doping concentrations. The electrons of the nucleation layer may be from the UID donors and the dislocations, and are still active even at 1.2 K. The test layer is doped with Si, which is a shallow donor for InAs. Therefore, all of the donors are ionized and the amount of bulk free electrons matches with the donors. During the cooldown, for any n-type InAs samples, the electron density of each layer is almost unvaried. The resistance first decreases and then increases as the temperature declines, which can be interpreted as the temperature dependence of mobility directly. The mobility improves at the beginning of the cooldown due to less phonon scattering. Once it reaches the maximum, the Coulomb scattering exceeds the phonon scattering, and becomes more robust indirectly due to less screening effect from the slightly dropped electron densities. Thus the mobility starts decreasing, consistent with the resistance cooldown history. Another interesting phenomenon is that the Fermi level rises up in the bulk as the temperature is lowered, whereas only slightly declines at the surface. In the confined potential well at the surface, the first two subbands are populated. The mobilities and the densities of the surface and bulk electrons derived from the three-band fitting are consistent with the ones analyzed through the Shubnikov-de

Haas oscillations at liquid helium temperatures. At the temperatures studied, the surface and the bulk electron mobilities decrease as the doping concentration increases. Yet, the contributions to the conductivity from the surface and the nucleation layers are less weighted in n-type InAs with heavier doping. As a result, heavily doped n-type InAs is less affected by the surface accumulation layer.

5.2 p-type InAs

A multi-band structure also exists in our low mobility p-type InAs samples. At room temperature, surface electrons occupied the first two subbands in an approximate triangular potential well. The surface electrons form an inversion layer separated from the holes in the bulk. The measured Hall effects at low temperatures indicate a freeze of holes in the bulk and a switch between the inversion layer and the accumulation layer on the surface. Weak localization and antilocalization signals within low-field regime were observed, which are attributed to the surface electrons. The surface electron mobility keeps increasing as the temperature decreases, which is due to the reduction of the phonon scatterings and the Coulomb scatterings.

Chapter 6

Summary

We successfully grew n- and p-type InAs films, where a three-band system is observed. The multi-band analysis and the non-parabolicity theory can be applied to the characterization of the transport properties and the surface band structures of the InAs thin films. Among n-type InAs films, the electron densities increase as the doping concentration increases, whereas the mobilities decrease. During the cooldown, minimum resistances, which correspond to maximum mobilities, are observed. And the Fermi level in the bulk increases as the temperature decreases. In the p-type InAs, the surface electron mobility increases as the temperature decreases. At liquid helium temperatures, the holes are mostly frozen out, and weak localization and antilocalization signals from the surface electrons are obtained. From the antilocalization measurements, the relaxation times and the diffusive coherence lengths can be determined, which are crucial for the spin electronic devices.

Bibliography

[1] J. R. Weber, A. Janotti, and C. G. Van de Walle. Intrinsic and extrinsic causes of electron accumulation layers on InAs surfaces. *Appl. Phys. Lett.*, 97:192106, 2010.

[2] L. F. J. Piper, T. D. Veal, M. J. Lowe, and C. F. McConville. Electron depletion at InAs free surfaces: Doping-induced acceptorlike gap states. *Phys. Rev. B*, 73:195321, May 2006.

[3] C. A. Mead and W. G. Spitzer. Fermi level position at semiconductor surfaces. *Phys. Rev. Lett.*, 10:471, Jun 1963.

[4] L. Ö. Olsson, C. B. M. Andersson, M. C. Håkansson, J. Kanski, L. Ilver, and U. O. Karlsson. Charge accumulation at InAs surfaces. *Phys. Rev. Lett.*, 76:3626, May 1996.

[5] M. Noguchi, K. Hirakawa, and T. Ikoma. Intrinsic electron accumulation layers on reconstructed clean InAs(100) surfaces. *Phys. Rev. Lett.*, 66:2243, Apr 1991.

[6] T. D. Veal and C. F. McConville. Profiling of electron accumulation layers in the near-surface region of InAs (110). *Phys. Rev. B*, 64:085311, Aug 2001.

[7] L. J. van der Pauw. A method of measuring the resistivity and Hall coefficient on lamellae of arbitrary shape. *Philips Technical Review*, 20:220, 1958.

[8] H. H. Wieder. Transport coefficients of InAs epilayers. *Appl. Phys. Lett.*, 25:206, 1974.

[9] D. A. Anderson L. L. Taylor M. J. Kane, N. Apsley and T. Kerr. Parallel conduction in GaAs/$Al_xGa_{1-x}As$ modulation doped heterojunctions. *J. Phys. C: Solid State Phys.*, 18:5629, 1985.

[10] H. A. Washburn, J. R. Sites, and H. H. Wieder. Electronic profile of n-InAs on semi-insulating GaAs. *J. Appl. Phys.*, 50:4872, 1979.

[11] P. D. Wang, S. N. Holmes, T. Le, R. A. Stradling, I. T. Ferguson, and A. G. de Oliveira. Electrical and magneto-optical of MBE InAs on GaAs. *Semicond. Sci. Technol.*, 7:767, 1992.

[12] Y. Lin, A. R. Arehart, A. M. Carlin, and S. A. Ringel. Separation of bulk and surface electron transport in metamorphic InAs layers using quantitative mobility spectrum analysis. *Appl. Phys. Lett.*, 93:062109, 2008.

[13] W. Zawadzki and B. Lax. Two-band model for Bloch electrons in crossed electric and magnetic fields. *Phys. Rev. Lett.*, 16:1001, May 1966.

[14] W. Zawadzki, S. Klahn, and U. Merkt. Semirelativistic behavior of electrons in InSb in crossed magnetic and electric fields. *Phys. Rev. Lett.*, 55:983, Aug 1985.

[15] M. I. Guseva, N. V. Zotova, A. V. Koval, and D. N. Nasledov. A study of the behavior of column IV elements in InAs doped by ion implantation. *Sov. Phys. Semicond.*, 8:59, 1974.

[16] K. Wang, Y. Gu, X. Yang, T. Yang, and Z. Wang. Si delta doping inside InAs/GaAs quantum dots with different doping densities. *J. Vac. Sci. Technol. B*, 30:041808, 2012.

[17] J. H. Davies. *The physics of low-dimensional semiconductors: An introduction.* Cambridge University Press, New York, NY, 1997.

[18] A. P. Roth, J. B. Webb, and D. F. Williams. Band-gap narrowing in heavily defect-doped ZnO. *Phys. Rev. B*, 25:7836, Jun 1982.

[19] Z. M. Fang, K. Y. Ma, D. H. Jaw, R. M. Cohen, and G. B. Stringfellow. Photoluminescence of InSb, InAs, and InAsSb grown by organometallic vapor phase epitaxy. *J. Appl. Phys.*, 67:7034, 1990.

[20] Ioffe Physical Technical Institute. Fermi level versus temperature for different concentrations of shallow donors and acceptors. `http://www.ioffe.ru/SVA/NSM/Semicond/InAs/Figs/723.gif`.

[21] C. Kittel. *Introductrion to solid state physics.* Wiley, Danvers, MA, 2004.

[22] M. M. Parish and P. B. Littlewood. Classical magnetotransport of inhomogeneous conductors. *Phys. Rev. B*, 72:094417, Sep 2005.

[23] A. Patanè, W. H. M. Feu, O. Makarovsky, O. Drachenko, L. Eaves, A. Krier, Q. D. Zhuang, M. Helm, M. Goiran, and G. Hill. Effect of low nitrogen concentrations on the electronic properties of $InAs_{1-x}N_x$. *Phys. Rev. B*, 80:115207, Sep 2009.

[24] T. I. Voronina, T. S. Lagunova, S. S. Kizhayev, S. S. Molchanov, B. V. Pushnyi, and Yu. P. Yakovlev. MOCVD growth and Mg-doping of InAs layers. *Semiconductors*, 38:537, 2003.

[25] Yao Zhang, R. L. Kallaher, V. Soghomonian, and J. J. Heremans. Measurement by antilocalization of interactions between InAs surface electrons and magnetic surface species. *Phys. Rev. B*, 87:054430, Feb 2013.

[26] Yao Zhang and J.J. Heremans. Effects of ferromagnetic nanopillars on spin coherence in an InGaAs quantum well. *Solid State Commun.*, 177:36, 2014.

[27] W. Wei and G. Bergmann. CuCo: A new surface Kondo system. *Phys. Rev. B*, 37:5990, Apr 1988.

[28] H. He, G. Wang, T. Zhang, I. Sou, G. K. L Wong, J. Wang, H. Lu, S. Shen, and F. Zhang. Impurity effect on weak antilocalization in the topological insulator bi_2te_3. *Phys. Rev. Lett.*, 106:166805, Apr 2011.

[29] H. Lu, J. Shi, and S. Shen. Competition between weak localization and antilocalization in topological surface states. *Phys. Rev. Lett.*, 107:076801, Aug 2011.

[30] S. Hikami, A. I. Larkin, and Y. Nagaoka. Spin-orbit interaction and magnetoresistance in the two dimensional random system. *Prog. Theor. Phys*, 63:707, 1980.

[31] S. V. Iordanskii, Yu. B. Lyanda-Geller, and G. E. Pikus. Weak localization in quantum wells with spin-orbit interaction. *Pisma Zh. Eksp. Teor. Fiz.*, 60:199, Aug 1994.

[32] Ch. Schierholz, R. Kürsten, G. Meier, T. Matsuyama, and U. Merkt. Weak localization and antilocalization in the two-dimensional electron system on p-type InAs. *Phys. Stat. Sol. (b)*, 233:436, 2002.